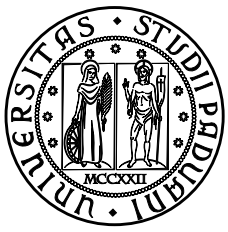

UNIVERSITÁ DEGLI STUDI DI PADOVA

DIPARTIMENTO DI FISICA
"GALILEO GALILEI"

DOTTORATO DI RICERCA IN FISICA
XXII° CICLO

DOPANT AND NON-DOPANT IMPURITIES IN SEMICONDUCTORS: BORON IN GERMANIUM

Direttore della scuola: Ch.mo Prof. Attilio Stella

Supervisore: Ch.ma Prof.ssa Marina Berti

Co-Supervisore: Dott. Gabriele Bisognin

Dottoranda: *Silvia Vangelista*

January 31, 2010

To my family

Sommario

Il germanio negli ultimi anni ha riscontrato un rinnovato interesse, sia nel campo scientifico che tecnologico, in quanto sembra costituire una valida alternativa al silicio come substrato per la realizzazione di dispositivi tecnologici di dimensioni sempre più piccole. Questo interesse ha stimolato nuovi studi riguardanti proprietà fisiche fondamentali di questo materiale, poiché la maggior parte della letteratura a disposizione sul germanio risale agli anni Cinquanta e Sessanta ed è incompleta.

In questa tesi vengono affrontati due aspetti poco indagati del germanio: la presenza e la natura dei difetti formati a seguito di impianti amorfizzanti e sub-amorfizzanti, attraverso lo studio dello strain indotto nel substrato; la variazione del parametro reticolare indotto da atomi di boro posti in siti sostituzionali o in clusters con atomi di germanio interstiziale. Entrambi gli argomenti vengono affrontati utilizzando principalmente la tecnica di diffrazione a raggi x ad alta risoluzione (HRXRD), tecnica che permette di rivelare lo strain dovuto alla presenza di difetti anche molto piccoli o presenti con bassa densità, per questo invisibili con altre tecniche. Lo studio dei difetti da impianto è importante soprattutto a causa delle conseguenze che questi possono avere nell'interazione con i droganti successivamente introdotti nel substrato.

In questa tesi si dimostra che impianti sia amorfizzanti che sub-amorfizzanti danno luogo a difetti di tipo interstiziale; lo studio delle cinetiche di scioglimento ha indicato che in entrambi i casi sono oggetti semplici, come difetti di punto.
In particolare, nei campioni con impianto amorfizzante si formano difetti a fine range di impianto, rivelati tramite HRXRD sia *prima* sia *dopo* la ricrescita epitassiale del film amorfo, i quali si sciolgono dopo annealing a temperature moderate ($< 400\ ^{\circ}$C). Nei campioni impiantati con dosi non-amorfizzanti si formano difetti la cui natura e stabilità dipendono dalla dose di impianto.
In questi campioni non-amorfizzati sono presenti layer sottili di boro, il quale dovrebbe diffondere per la presenza di interstiziali generati dagli impianti e messi in movimento da trattamenti termici (il meccanismo di diffusione del boro in germanio è proprio di tipo interstiziale). L'assenza di diffusione suggerisce la presenza di meccanismi locali di ricombinazione degli

interstiziali con le vacanze, di cui il germanio è ricco a differenza del silicio.

Per quanto riguarda il secondo argomento, l'interesse verso il boro nasce dal fatto che è il drogante di tipo *p* più promettente in germanio, soprattutto per la sua bassa diffusività. Il drogante viene di norma introdotto per impianto ionico nel substrato amorfizzato e non nel cristallo, per evitare che gli atomi di drogante possano penetrare in profondità nel campione per effetto channeling, allargando il profilo di impianto in maniera incontrollata.
In questa tesi si dimostra che anche impiantando in cristallo si possono ottenere ottimi risultati dal punto di vista della sostituzionalità e dell'attivazione elettrica del boro, se durante l'impianto si mantiene il substrato a temperature molto basse (in particolare alla temperatura dell'azoto liquido). Attraverso l'analisi di questi campioni con la tecnica HRXRD è possibile individuare la variazione del parametro reticolare indotto dal boro sostituzionale e quello indotto dal boro associato agli interstiziali, dati ancora mancanti in letteratura.

Questi risultati costituiscono un tassello fondamentale per la corretta interpretazione di fenomeni fisici quali il danno da impianto e la diffusione del drogante, e possono essere utilizzati per costruire modelli teorici sempre più accurati.

Abstract

In recent years germanium found a renewed interest both in the scientific and in the technological field, since it appears an effective alternative to silicon as a substrate for the realization of smaller and smaller technological devices. This interest stimulates new studies about some fundamental physical properties of this material, as most part of the literature at disposal about germanium dates back to the fifties and sixties and it is incomplete.

In this thesis two not-well investigated aspects of germanium are addressed: the presence and the nature of the defects formed following amorphizing and sub-amorphizing implants, through the study of the strain induced in the substrate; the lattice parameter variation induced by boron atoms placed in substitutional sites or in clusters with interstitial Ge atoms. Both the arguments are addressed mainly using the High Resolution X Ray Diffraction (HRXRD) technique, which allows to reveal the strain due to the presence of small defects and present with low density, for these reasons invisible by other techniques. The study of the defects caused by implantation is important especially for the consequences that they can have in the interaction with dopants subsequently introduced in the substrate.

In this thesis it is demonstrated that both amorphizing and sub-amorphizing implants give rise to defects; the study of the dissolution kinetics shows that in both cases they are simple objects, such as point defects.
In particular, in the amorphized samples defects are formed at the end of the implant range, revealed by HRXRD both *before* and *after* the epitaxial regrowth of the amorphous layer, which dissolve after annealing at moderate temperatures ($< 400\ ^{\circ}$C). In the sub-amorphized implants the nature and the stability of the defects formed depend on the implant fluence.
The same samples are grown with thin boron layers, which should diffuse for the presence of interstitials formed by implants and put in motion by the thermal treatments (boron diffusion mechanism in germanium is interstitials mediated). The absence of any diffusion suggests the presence of local mechanisms of recombination between interstitials and vacancies, of which germanium is rich on the contrary of silicon.

About the second topic, the interest on boron is due to the fact that it is the the primary

p-type dopant, especially for its low diffusivity. The dopant is usually introduced by ion implantation in the amorphized substrate, not in the crystalline substrate to avoid that dopant ions can go deep into the sample, broadening the implant profile in a not controlled manner.
In this thesis it is demonstrated that also in crystal implantation very good results about boron substitutionality and the electrical activation can be obtained, if during the implant procedure the substrate is kept at low temperature (in particular, at liquid nitrogen temperature). By the HRXRD analysis of samples it is possible to detect the lattice parameter variations induced by substitutional and clustered boron, still lacking in literature.

These results represent a fundamental step forward in the description of fundamental physical phenomena in germanium, such as implant damage and dopant diffusion, and they can contribute in the formulation of more complete theoretical models for their interpretation.

Contents

List of Figures

List of Tables

Introduction: concepts and objectives

The history of germanium since its discovery in 1886 by Wrinkler has been made of periodic fortune and misfortune. It has been discovered later than silicon, but it has been chosen as the key substrate material in the early days of semiconductor transistor developments. The invention of transistor happened accidentally by Shockley, Bardeen and Brattain (1947), during their studies on the field-effect devices , but already in the late forties germanium has been the first choice for this type of researches and applications thanks to a superior crystalline quality at that time respect to silicon. Moreover, its electron mobility three times higher and its hole mobility four times higher than in Si attracted the attention of physicists working on high frequencies devices.
Till the late fifties - early sixties Ge was the main semiconductor, and lots of efforts have been spent to explore its physical properties. Most of the interesting properties of semiconductors were discovered firstly in germanium: the first evidence of plasticity at high temperature in a covalent cubic face cubic centered (fcc) diamond lattice semiconductor was reported in 1952 on Ge; studies on deformed germanium allowed for a new perspective in the mechanical properties of crystalline materials and the observations about its strain-stress characteristic explained with dislocations dynamics were valuable also for other materials. Moreover, many fundamental studies on point defects and impurities started on germanium, in particular the use of group III (B, Ga and Al) and group V (P, As and Sb) impurities as doping atoms, in order to introduce shallow-levels into the band gap.
If on the one hand bipolar transistor was developed in germanium, on the other hand the progress in field-effect devices was limited by the poor quality of its oxide GeO_2. This shortage, together with the development of planar technology on silicon wafers and the lower price of Si than Ge due to the higher availability of the former (it's the second most abundant element of the Earth's crust), stopped the use of Ge as a microelectronic material.

For the next forty years, silicon knew a continuous expansion in its employment, while germanium became the material used for "niche" markets, like epitaxial substrate for III-V solar cells or high resistivity material for the fabrication of nuclear-radiation detectors. This

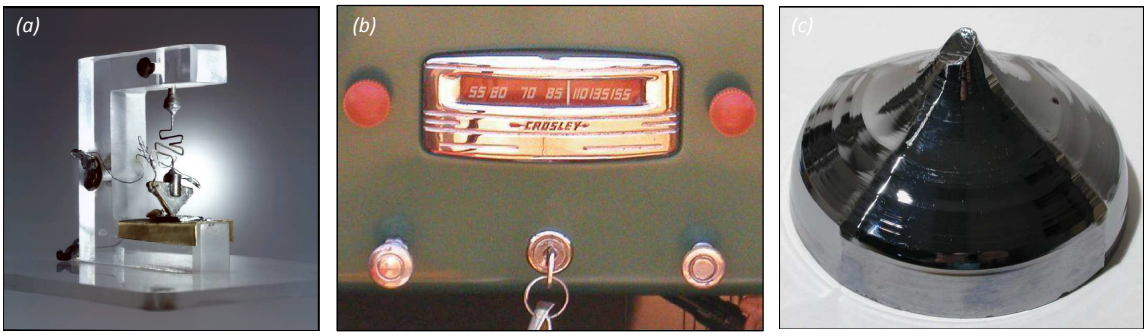

Figure 1: *(a) The first transistor realized in Ge (1948); (b) early "Motorola Chrome Nose" radio Ge based; (c) Ge wafer boule.*

stop in the use of germanium in large consumers devices induced also a stop in the exploration of its basic properties.

Thanks to the opportunities offered by this material, in recent years germanium is considered again as an interesting substrate for micro-electronics applications.
In fact, until the 65 nm CMOS technology node, device scaling down has been achieved by reducing the feature size, maintaining the same materials, i.e. silicon and its oxide. But the physical thickness of the gate oxide became too much small to permit the electron tunneling (~ 3 nm) and the leakage current density became too much high.
This problem can be overcome replacing the classical SiO_2 with high-κ dielectric materials, so that a thicker gate oxide can be implemented. Unfortunately, the employment of these materials has to face some serious problems. First of all, high-dielectric materials can be grown with a poorer quality respect to silicon oxide with the current deposition techniques: this limits the high-field mobility of the transistors and so the advantage of high-κ material use is compensated by a lower drive current. For this and other reasons, scientific community renews its interest for the so-called high-mobility substrates, like III-V compounds, strained silicon, strained SiGe and germanium. The instability of GeO_2 now turns into an advantage: it has been demonstrated that under the same deposition conditions, the interfacial oxide thickness is significantly lower in the case of a Ge substrate than of a Si one. Ge-based p-MOS transistors have been already processed, giving improved performance compared to Si-based counterparts.
Despite these encouraging results, lots of efforts are necessary to overcome the lack of fundamental studies about the properties of germanium, and without this knowledge it will be impossible even to think to a possible switch over to Ge as a material for micro-electronics. Indeed, silicon and germanium are quite similar, but they are not the same semiconductor (table 1): for example they have different melting temperatures that influence the temperature processing, or different dopants behaviour and diffusivity that affect the realization of p- and n-MOS, etc ...

	germanium	**silicon**
Lattice type	Diamond	Diamond
Atomic number	32	14
Lattice parameter $a_0(\AA)$	5.657	5.431
Energy gap (eV) at 300 K	0.67 (Indirect)	1.11 (Indirect)
Dielectric constant ε_r	16.2	11.9
Atomic weight	72.590	28.090
Atomic density (atoms/cm^3)	4.419×10^{22}	4.995×10^{22}
Bulk intrinsic mobility (cm^2/Vs)		
Electrons	3900	1450
Hole	1800	505
Melting point (°C)	938.3	1414

Table 1: *Properties of germanium and silicon at Room Temperature.*

In particular, B seems to have among p-type dopants, the lowest diffusivity in Ge, but also a very low electrical activation under direct ion implantation; other p-type doping elements have been scarcely investigated and the data about solubility and diffusivity have been collected till the sixties, so their precision has to be verified using methods and techniques at our disposal at present. The role of dopants in germanium, how they can be introduced into the substrate (after substrate pre-amorphization or implanting directly in crystal), their diffusivity and the diffusion mechanism are key points to deepen.

Pre-amorphization of the substrate before dopant implantation and subsequent Solid Phase Epitaxial Regrowth is considered the best method in silicon to obtain shallow dopant concentration profiles and almost 100% of dopant electrical activation. It also well known that pre-amorphization creates defects (interstitials) at the End Of the implantation Range, the so-called EOR defects, that during subsequent annealing can dissolve and release an interstitial flux which has detrimental effects on dopants behaviour, giving rise to their clustering or anomalous diffusion (Transient Enhanced Diffusion). In germanium, little is known about the formation or the evolution of these type of defects, and the little available literature is quite controversial.

Direct dopant implantation in the crystalline substrate has been abandoned in Si caused of the channeling phenomena that spread the dopant concentration profile. Moreover implantation at room temperature, without any control of the substrate temperature during the process, can induced in some cases the so-called “dynamic annealing”, i.e. the annihilation induced by the beam itself. The thermal budgets supplied by the beam prevents the complete amorphization, but at the same time it is not sufficient for the annealing out of the defects that can interact with dopant ions.

Lowering the substrate temperature up to Liquid Nitrogen temperature (LNT) dynamic annealing can be avoided. In addition at this temperature boron implantation in germanium, which shows a “milder” structure compared to silicon, induces amorphization and after epitaxial re-

growth excellent results on the dopant electrical activation can be obtained, comparable to those gained with pre-amorphization.

The main technique used in this work, the *High Resolution X-Ray Diffraction* (HRXRD), has been used to analyze a pre-amorphized substrate determining the defects presence through the induced strain, their nature, and their dissolution kinetics. Also Ge substrates implanted with sub-amorphizing fluences has been examined, thus completing the scenario about the defectiveness in germanium after implantation. Moreover, thanks to the presence in these samples of arrays of shallow B-doped layers, it has been possible to detect by SIMS defects interaction with the dopant atoms.
Then samples implanted with different B fluences and keeping the substrates at different temperatures were analyzed by HRXRD. The technique allowed to detect the strain induced by the implanted boron and, using also information coming from NRA-RBS and electrical analysis, it was possible to assign the observed lattice contraction to substitutional boron and the lattice expansion to Boron-Interstitial Ge clusters. Moreover, the determination of the substitutional boron lattice parameter made the HRXRD a powerful technique from which the amount of boron atoms placed in regular lattice sites or off-sites could be deduced quickly and without destroying the sample.

This thesis is developed in four chapters:

- Chapter 1: it contains a review of the data available in literature at present about dopants in germanium (in particular boron): solubility, diffusivity, diffusion mechanisms through point defects;

- Chapter 2: it describes the main experimental tools used both for the realization and the analysis of the samples;

- Chapter 3: it deals with the results obtained in this work, in particular:

  - the EOR defects-induced strain due to Ge self-amorphization, and the kinetics of dissolution;

  - the defects-induced strain after sub-amorphizing implants, the kinetics of their dissolution, and the detection of possible enhancement B diffusion due to interstitials overpopulation;

  - the boron-induced strain after direct implants, keeping the substrates either at Room Temperature or at Liquid Nitrogen Temperature.

- Chapter 4: the results are summarized, giving a hint of possible future works.

Determination of deuterium concentration depth profiles in dilute nitride: fulfilment of previous work

In the first part of my PhD I worked on an argument already faced during my bachelor degree thesis, that is the formation/dissolution mechanism of hydrogen-nitrogen complexes in dilute nitrides, in order to complete some aspects still unexplained.

Hydrogen is a non-dopant impurity in semiconductors but its presence, unwanted or deliberately introduced, can have heavy consequences on the material properties: for example it can interact with native impurities or dopants and neutralize their effects.
In dilute nitrides (obtained from III-V semiconductors by the insertion of nitrogen into the group V sublattice, hydrogen has the effect to passivate nitrogen: indeed it forms complexes with nitrogen which reverse all the effects associated with N. Moreover H effects are fully reversible by thermal annealing of the samples at elevated temperature ($\sim$600 $^{\circ}$C).
These surprising properties attracted the attention of the scientific community, since they provide dilute nitride with additional employment opportunities by tuning the hydrogen amount, but it resulted fundamental to determine the physical mechanism leading to N passivation.
Experimental and theoretical works in literature indicated as responsible for nitrogen passivation the formation of almost two H-N complexes, whom stoichiometries were not clear cause of the difficulties in determining hydrogen location inside the sample (H is the smallest atomic species and it easily diffuses into semiconductors). Substituting hydrogen with deuterium, which is negligibly present in the natural isotopic abundance, but modifies electronic and structural properties of dilute nitrides as hydrogen does, it has been possible to use specific nuclear reactions in order to detect deuterium amount and, above all, to determine its concentration depth profiles in the samples.
At the end of my bachelor degree the stoichiometry of the different complexes formed after full deuteration was determined: only two different N-D complexes are responsible for the hydrogen-related effects observed in the examined samples. However, it was necessary to confirm the complexes stoichiometry independence of the *GaAsN* layer characteristics, like the thickness and the nitrogen concentration, and of deuteration conditions. Moreover, it was fundamental to clarify in which way the D incorporation proceeded into the samples.

In appendix of this thesis the results obtained during the PhD work on this argument are reported, together with a brief overview of the argument in literature and a short description of the results gained with my bachelor degree thesis.

Chapter 1

Germanium: Defects and Dopants

1.1 Diffusion Mechanisms

Diffusion, namely a movement of atoms through a solid, can be approached considering a continuous medium and ignoring the atomistic nature of the diffusion process. This leads to the formulation of Fick's law: the flux or diffusion current **J** of the species considered, defined as the number of respective atoms passing a unit area in a unit time interval, is related to the gradient of their concentration **C**:

$$\overrightarrow{J} = -D \cdot \nabla C \tag{1.1}$$

The negative sign means that the diffusion occurs from the zone of higher concentration to the zone of lower concentration. This law represents the macroscopic definition for the diffusion coefficient D ($cm^2 s^{-1}$).
To calculate the change in the amount of an arbitrary substance in a given volume V, the fluxes via the volume boundary S as well as the generation or loss within the volume have to be taken into consideration. This leads to a general continuity equation that, in absence of external sinks or sources of substances can be express as:

$$\frac{\partial C}{\partial t} = -\nabla \overrightarrow{J} \tag{1.2}$$

Combining this equation with 1.1 we have the so-called Fick's second law of diffusion:

$$\frac{\partial C}{\partial t} = \nabla (D \cdot \nabla C) \tag{1.3}$$

Many diffusion phenomena can be dealt with the phenomenological base of Fick's laws. All that is required, is to know the diffusion coefficient and its dependence on temperature and possibly other variables - it is not necessary to know anything about the atomic mechanisms in-

volving point defects to solve diffusion problems. It turns out, however, that complex diffusion problems - e.g. simultaneous diffusions (B and P in Si), can not be modeled adequately without knowing the atomic mechanisms and their interaction. Atomistic processes are considered within the framework of the random-walk theory.
In solids, above the absolute zero temperature, the atoms are in constant motion around energetically favoured positions. Time-averaged, these oscillations do not lead to a net displacement. In order to have a real displacement, only jumps of atoms between energetically favourable sites are considered. The direction of each of these jumps is independent of those of previous jumps: the atoms perform the so-called "random walk" or "Brownian movement". This is a general relation between the mean square distance covered by the random walking atom (also called diffusion length L) and the number of steps and the square of the distance r_0 covered in one step:

$$\langle r^2 \rangle = L^2 = r_0^2 \cdot 3N. \tag{1.4}$$

The phenomenological description of diffusion (that only works on averages and thus only if many particles are considered) has to be linked with the basic diffusion event, the single jump of a single atom or defect.
The net flux of particles is described as the difference in the number of particle jumps to the left and to the right. With the jump frequency ν eq. 1.1 can be obtained with the following expression for the diffusion coefficient (for cubic crystals):

$$D = g \cdot a^2 \cdot \nu \tag{1.5}$$

with a the lattice constant and g a geometric factor of the lattice type we consider; it takes into account that considering all jumps that are possible in the given lattice, only some have a component in the x-direction.
The jump frequency is given by:

$$\nu = \nu_0 \cdot \exp\left(-\frac{G_m}{k_B T}\right) \tag{1.6}$$

with G_m the free enthalpy for the jump or for the migration of the atom or defect, and ν_0 the frequency of "attempts" to overcome the enthalpy barrier for a jump; it is, of course, the vibration frequency of the lattice atoms (around 10^{13} Hz).
This gives the second important set of parameters describing a property of a dopant, namely its migration energy (also called activation energy) H_m and its entropy S_m:

$$G_m = H_m - T S_m. \tag{1.7}$$

Combining eq. 1.6 with eq.1.7 the diffusion coefficient D can be expressed in terms of the migration energy:

$$D = D_0 \cdot \exp\left(-\frac{H_m}{k_B T}\right) \tag{1.8}$$

where all the constants have been included in D_0.
These formulas relate the atomic properties of defects to the diffusion coefficient from Fick's laws.

1.2 Intrinsic Point Defects

There are several atomic mechanisms that lead to the movement of atoms, which depend on whether the diffusing atom resides in a lattice (substitutional) or interstitial position: a substitutional atom can migrate by exchange with a direct neighbour, while an interstitial can jump from on interstitial site to a nearest neighbour one. However, most diffusion processes are mediated by intrinsic point defects: vacancies (V) and interstitial (I).
Three principal atomic diffusion mechanisms are possible. The first one is the *direct mechanism*, where impurities which have small ionic radii can travel directly from one interstitial site to another one: some metals, for example Cu, Li, Ni, diffuse through direct interstitial mechanism with a low activation energy so that they have very high diffusivities at low T.
In germanium the dominant diffusion mechanism is in general considered the *vacancy mechanism*, where a diffusing atom jumps into a neighbouring vacant lattice site. To avoid oscillations of this exchange procedure, the vacancy must move at least to a third-neighbour site away from the dopant. Thus, the vacancy or another vacancy within the diffusion regime can return on a different path within the germanium's diamond lattice. Then long-range migration of the dopant will take place (figure 1.1).

The counterpart of the vacancy mechanism is the *interstitialcy mechanism* (figure 1.2). Dopant diffusion takes place when a dopant at a substitutional site is approached by a germanium interstitial. The dopant is kicked out by the interstitial to reside at interstitial position, while the original self-interstitial has disappeared by occupying the regular lattice site. Now this interstitial dopant is able to move towards an adjacent lattice site to re-form a germanium interstitial by the same "kick-out" process, like the interstitial dopant itself was generated.
It is common to denote the diffusing species involved by one of the above mechanisms as dopant-defect pairs. In the case of the vacancy mechanism, we label a dopant X which is in the vicinity of a vacancy V as XV-pair. If the dopant resides on a substitutional lattice position, it is referred to as X_s, while when the dopant X is adjacent to an interstitial I, it is written as XI-pair and as X_i when it rests at an interstitial site (e.g. after implantation). The rate equations for the

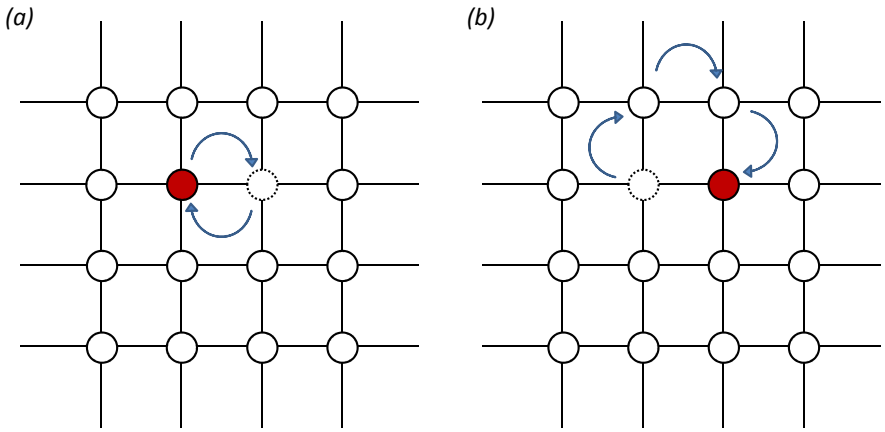

Figure 1.1: *Vacancy mechanism for self-diffusion: (a) the tagged germanium atom (dark colour) moves by jumping into the vacancy to its right; (b) vacancy moves to the third-neighbour within the diamond lattice for persist dopant migration.*

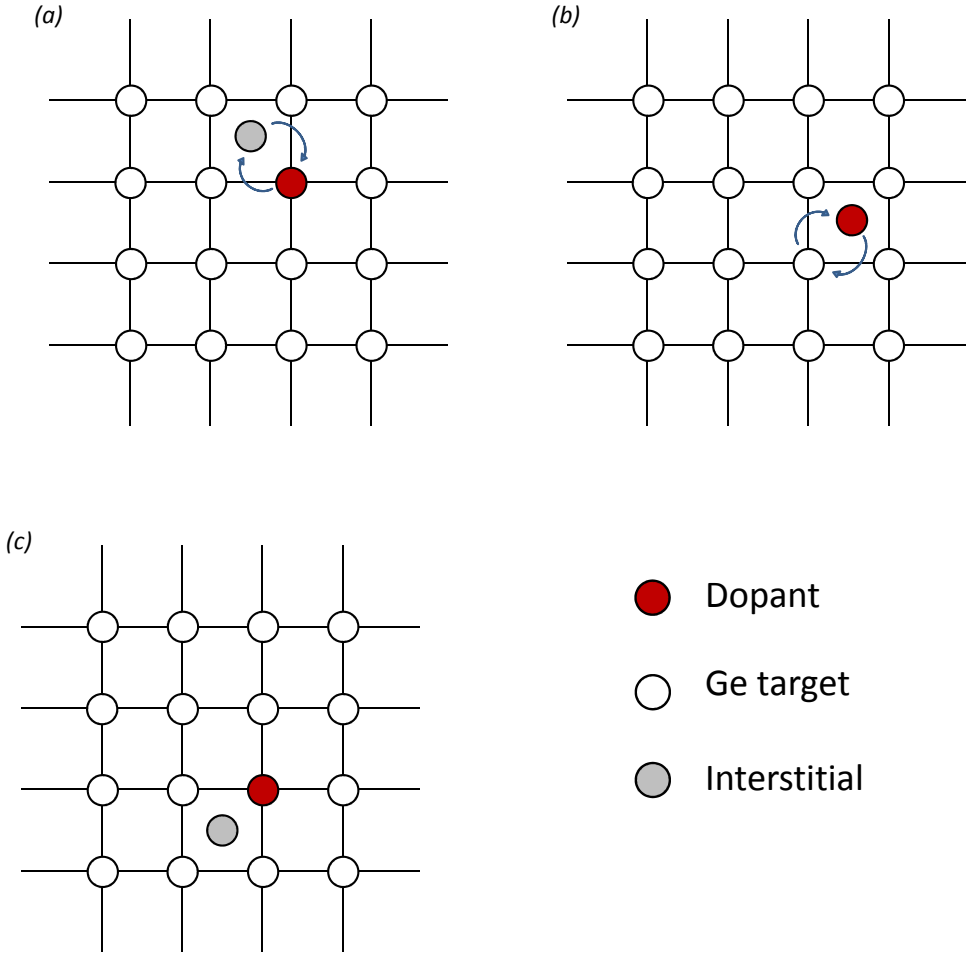

Figure 1.2: *Dopant diffusion via a substitutional-interstitialcy interchange. Dopant at a substitutional site is pushed to an interstitial site by the "kick-out" reaction.*

basic atomistic diffusion mechanisms are:

$$X + V \Leftrightarrow XV, \tag{1.9}$$

$$X + I \Leftrightarrow XI, \tag{1.10}$$

$$X_s \Leftrightarrow X_i + V, \tag{1.11}$$

$$X_s + I \Leftrightarrow X_i. \tag{1.12}$$

If a non-equilibrium density of interstitials is present, e.g. agglomerated at the end-of-range damage region after ion implantation, the mechanism (1.12) can lead a strong enhancement of dopant diffusivity. This is what happens during *Transient Enhanced Diffusion* (TED) of boron in Si. Once the excess interstitials are consumed or have disappeared by surface recombination, the TED stops and normal equilibrium diffusion takes over.
Permanent transport of dopants within the lattice is not only controlled by the diffusion mechanism, there are also recombination processes between dopants and point-defects occur, which can disturb or even prevent dopants from diffusion. These recombinations are always possible when dopant-defect pairs are approaching lattice defects of the opposite type. The basic rate equations for XI and XV pair recombinations are given by:

$$XI + V \Leftrightarrow X_s \tag{1.13}$$

$$XV + I \Leftrightarrow X_s \tag{1.14}$$

The previously defined diffusion current $\mathbf{J}$ can now be expressed with respect to point-defect interactions:

$$\overrightarrow{J} = -D_{XI} \cdot \nabla C_{XI} - D_{XV} \cdot \nabla C_{XV} \tag{1.15}$$

In germanium, where self-diffusion is dominated by mono-vacancy mechanism [1], the diffusion coefficient or diffusivity is given by the product of the diffusion coefficient of the mono-vacancy D_V times its equilibrium concentration relative to the atomic density C_V^{eq}:

$$D_{Ge} = f_V D_V C_V^{eq} \tag{1.16}$$

Where f_V is the correlation factor, equal to for $1/2$ the vacancy mechanism in diamond lattice (Ge).
The mono-vacancy mechanism in Ge can occur in different charge states. Assuming that V could exist in the neutral, singly positive, and singly negative state, the total equilibrium concentration of vacancies becomes function of the Fermi level in the material. The self-diffusion is then not only a function of T, but becomes also dependent on the Fermi level for highly

doped, extrinsic material. Equation (1.16) becomes:

$$D_{Ge} = \frac{1}{2}\left(D_V^0 C_V^{eq0} + D_V^- C_V^{eq-} + D_V^+ C_V^{eq+}\right) \tag{1.17}$$

$$D_{Ge} = D_{Ge}^0 + D_{Ge}^-\left(\frac{n}{n_i}\right) + D_{Ge}^+\left(\frac{n_i}{n}\right) \tag{1.18}$$

With n the free electron concentration and ni the intrinsic carrier concentration.
In the case of multiple positive and negative charge states, formula (1.18) can be generalized to:

$$D_{Ge} = D_{Ge}^0 + \sum_{r=i} D_{Ge}^{r-}\left(\frac{n}{n_i}\right)^r + \sum_{s=i} D_{Ge}^{s+}\left(\frac{n_i}{n}\right)^s \tag{1.19}$$

From this equation one derives that in extrinsic n-type material ($n >> n_i$) self-diffusion of germanium will be enhanced, due to the contribution of negatively charged vacancies. The experimental self-diffusion coefficient can be explained by considering neutral and negative charge states of V only, that is we can neglect the third term in equation (1.19). This means that self-diffusion will be enhanced in heavily n-doped Ge, compared with intrinsic materials, while it is expected to be lowest in heavily p-doped Ge.

The experimental methods to study point defects can be divided in two groups [1], [2]:

- Experiments in which the defects concentration and distributions are essentially those corresponding to thermal equilibrium at the measuring T;
- Experiments in which the point defects are not in thermal equilibrium, i.e., the crystal is supersaturated or under-saturated with point defects.

For the first group, it's important to note that the concentration of point defects in Si and Ge are several orders of magnitude lower that those in metals with comparable melting points. As a consequence, it is not possible to detect directly the presence of point defects in thermal equilibrium at high temperatures. In principle, such investigations would give the free energy of formation of those defects that dominate in thermal equilibrium (e.g. vacancies, di-vacancies, self-interstitials). In absence of direct information, self-diffusion measurements are the most important for the study of point defects with low G_m values in Ge. The standard approach to measure self-diffusion in solids is the use of radioactive tracers: the diffusion coefficient is obtained by comparing the distribution of tracer atoms resulting from a diffusion treatment with a theoretical diffusion profile. The distribution of the tracer atoms can be determined by measuring the radioactivity in successive removed layers. Secondary Ion Mass Spectrometry (SIMS) is utilized to determine the profile of these radio-isotopes.
In Ge, a good number of radioisotopes with sufficiently long half-life are at disposal for these studies. Most often ^{71}Ge is used [3], [4], [5], [6], [7]: it is produced from stable ^{70}Ge by neutron

capture and γ-emission, and it decays by electron capture in stable ^{71}Ga. Another candidate is ^{77}Ge, produced by (n,γ) reaction with ^{76}Ge atom [3], [5], and it decays to ^{77}As by electron emission. Figure 1.3 summarizes the D_{Ge} obtained from radio-active tracer studies [3], [4], [5], [6], [7]; according to this last reference, the Arrhenius law of figure 1.3 can be written as:

$$D_{Ge} = 13.6 \cdot \exp\left(-\frac{3.094eV}{k_B T}\right)(cm^2/s) \tag{1.20}$$

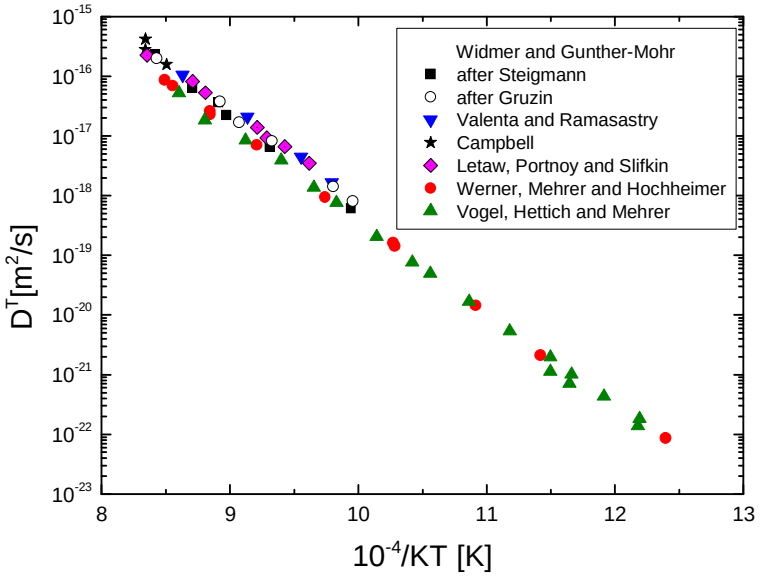

Figure 1.3: *Arrhenius plot of self-diffusion in intrinsic Ge at ambient pressure [7].*

Another method to measure self-diffusion consists in the evaluation of the diffusion of stable isotopes with different mass [8], thanks to the SIMS mass separation capabilities. As shown in figure 1.4, there's a good agreement with previous work. The corresponding fit yields:

$$D_{Ge} = 12 \cdot \exp\left(-\frac{3.05eV}{k_B T}\right)(cm^2/s) \tag{1.21}$$

More recently, Huger et al. [9] investigated single crystalline germanium $^{70}Ge/^{nat}Ge$ isotope multi-layer structure, in order to determine self-diffusion between 429° and 596 °C using neutron reflectometry. The diffusivity obtained is well describe by the Arrhenius equation:

$$D_{Ge} = 23 \cdot \exp\left(-\frac{3.13eV}{k_B T}\right)(cm^2/s) \tag{1.22}$$

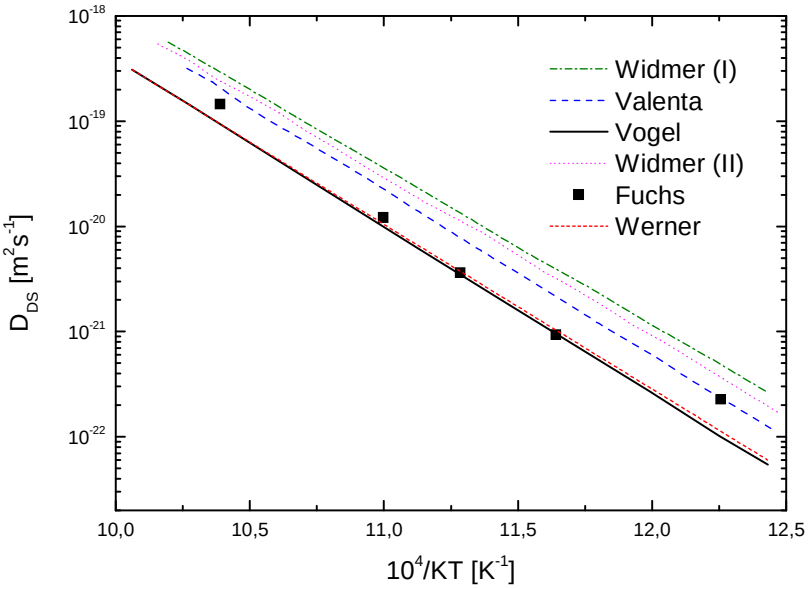

Figure 1.4: *Arrhenius plot of the Ge self-diffusion coefficient as a function of temperature [8].*

The isotope mass effect is rather small, but it is possible to observe the same diffusion behaviour using other Group IV impurities (Si, Sn, in particular) [10], [11], [12], [13]: since these impurities are electrically neutral, the main difference should come from the different elastic interaction due to the atom size. In table 1.1 we can find the same trend both for activation enthalpy ($H_{Si} < H_{Ge} < H_{Sn}$) and the frequency factor ($D_{0Si} < D_{0Ge} < D_{0Sn}$). This means that the higher the atom size, the higher is D.

Element	**H (eV)**	$D_0(cm^2/s)$	**Technique**
Ge	3.09	13.6	Radio tracer [7]
Si	3.32	42	SIMS [13]
Sn	3.26	840	SIMS [11]

Table 1.1: *Values for the activation energy (enthalpy) and pre-factor for Ge self- diffusion, Si diffusion and Sn diffusion in Germanium.*

Turning now to the second group of point defect investigations, there are three classical methods for generating supersaturations of point defects, namely:

- *quenching* from high temperature followed by annealing at low temperature at a rate fast enough to prevent the annealing out of the defects;
- *plastic deformation*;
- *irradiation* at low temperatures, in order to create vacancy-interstitial pairs and simple point defects.

In the quenching technique the rapid cooling down after heating up the material close to the melting point, allows the defects present in thermal equilibrium at high temperature to freeze their concentration, avoiding diffusion and precipitation. In the early work on germanium, an additional complication was its "thermal conversion": n-type Ge crystal may be converted to p-type with a thermal treatment above 800 °C; moreover this conversion can be suppressed if the crystal surface is first etched and cleaned. Detailed investigations showed that the thermal conversion was connected to copper contamination, and it must be concluded that most of the early quenching experiments give no information on intrinsic defects in germanium. However this phenomenon stimulated the study about Cu diffusion in Ge, through the precipitation method. According to ref. [14] and [15], the self-diffusion coefficient obtained with this method is:

$$D_{Ge} = 6.2 \cdot \exp\left(-\frac{2.94eV}{k_B T}\right)(cm^2/s) \tag{1.23}$$

Successively, great efforts to reduce Cu contamination have been performed (see ref. [1] and references therein). The quenched-in defects are detected by their action as acceptors; the number of quenched-in acceptors per unit volume N_A follows approximately the Arrhenius relation:

$$N_A = N_A^0 \cdot \exp\left(-\frac{E_A^F}{k_B T_q}\right) \tag{1.24}$$

Where T_q is the quenching temperature. In terms of the acceptor concentration C_A equation 1.24 can be written as:

$$C_A = C_A^0 \cdot \exp\left(-\frac{E_A^F}{k_B T_q}\right) \tag{1.25}$$

All the works reported in ref. [1] found an effective formation energy $E_A^F \sim 2$ eV: this energy has been generally assumed to be the formation energy of mono-vacancies in Ge.
Hiraki and Suita [16] deduced the following diffusion coefficient of the quenched-in defects:

$$D_{Ge} = 2 \cdot \exp\left(-\frac{1.2eV}{k_B T}\right)(cm^2/s) \tag{1.26}$$

which they assigned to the migration of mono-vacancies.
Subsequently, after evidences of high mono-vacancy mobility, it appeared certain that the quenched-in acceptors were not mono-vacancies. During quenching, mono-vacancies must have reacted either with impurity atoms to form complexes or among themselves to form di-vacancies or larger vacancy clusters. These discrepancies show that quenching process is a complicated phenomenon.

Plastic deformation of Ge introduces, in addition to the array of dislocations, other crystalline defects, like interstitials or vacancies. But, since Ge can be deformed plastically only at temperatures above the two thirds of the melting temperature, single vacancies or interstitials

generated during plastic deformation anneal out instantaneously on account of their low migration energy. However, there are good theoretical reasons to consider the migration energy of di-vacancies higher than that of a single vacancy, so di-vacancies might be retained at the deformation temperature. Thus, the acceptor level 0.1 eV above the valence band, found by ref.[14], firstly attributed to mono-vacancy, might be attributed to the di-vacancies [1].

Partly due to the inherent limitations of the quenching and deformation experiments, *irradiation* studies have become the most widely used tool for the investigation of point defects in semiconductors. The basic idea about irradiation experiment is the following: by the interaction between lattice atoms and energetic particles (ion or photons) the former can be displaced to create a vacancy, while the recoiled atoms come at rest in interstitial positions. The higher the energy transferred from the incident radiation to the Ge atom, the more complex defects are created during irradiation: electron and γ- irradiation can be arranged such as to create rather simple defects.

In contrast to silicon, reliable information on the properties of intrinsic point defects in germanium is rather limited, despite to numerous studies devoted. This is particularly true for mono-vacancy. For a long time it was assumed that the migration energy of a mono-vacancy in Ge was $\sim$ 2 eV, which implied that the mono-vacancy should be an abundant defect at room temperature after electron and γ - irradiation. Serious doubts about the correctness of this interpretation were raised after *Electron Paramagnetic Resonance* (EPR) experiments [17], that established a migration energy for neutral mono-vacancy in silicon equals to $E^F_{V^0} = (0.33 \pm 0.03)$ eV. Since then, evidences have been found from radiation damage experiments about its small migration energy also in germanium. From electron oxygen-rich Ge samples irradiated at low temperature (25 K) and the annealed [18], it has been estimated a migration barrier for the single vacancy of about 0.2 eV. Ershov et al. [19] found values for the migration energies of neutral and singly charged vacancies in Ge of (0.52 ± 0.05) and (0.42 ± 0.04) eV, respectively.

More recently, some works reported theoretical estimations using molecular-dynamics calculations about the migration energy of neutral vacancy: table 1.2 resumes the results obtained. For comparison, also migration energies for interstitials are reported.

$E^M(V^0)$	$E^M(I^0)$	**Calculation**	**Reference**
0.26	0.64	MD with SW Potential	[22]
0.38	0.76	MD with SW Potential	[20]
0.4	0.87	MD with SW Potential	[21]
0.25	–	DFT with LDA approx.	[23]
0.4	–	DFT with LDA approx.	[24]
0.5÷0.7	1.0÷1.4	MD calculations	[25]

Table 1.2: *Calculated migration $E^M(V^0, I^0)$ energies in eV of the uncharged vacancy and interstitial in germanium ($<110>$ dumbbell site) after [25].*

1.3 Diffusion of p-type and n-type dopants

Impurities of the Group III and Group V in Ge behave as acceptors and donors respectively, with a single energy level close to the edges of the energy band. They are therefore easily ionized and their diffusion can be studied conveniently by *p-n junction* method [26]. In this method, the material under study is doped such that the type of the electrical conduction is opposite to that generated when the impurity has diffused in. The diffusion profile is obtained by locating the p-n junction developed after diffusion as a function of diffusion time. To evaluate the diffusion coefficient, further information on the total concentration of diffusing material and the initial concentration of uniformly distributed current carriers in the specimen are required. The p-n method differs from the standard radio tracer technique since it provides information on the diffusion of electrical active impurity atoms in a uniformly doped sample, whereas by means of tracer methods, diffusion in intrinsic material may also be investigated.
With respect to impurities, a distinction is made between slow diffusers, which are up to 100 times faster than self-diffuser, and fast diffusers, which follow generally an interstitial mechanism (Cu, Li, Ni ...). Group III are among the slow diffusers, while Group V dopants are typically 100 times faster, having an activation enthalpy lower than H_{Ge} and a pre-factor lower than D_{0Ge} (table 1.3).
If we look at the table 1.3, reporting the activation enthalpy and pre-factor by different authors for the most important Group III and V dopants, the data may be contradictory. The discrepancies probably arise from the different experimental conditions, then diffusion phenomenon deserves further systematic studies. For comparison on table 1.4 the activation enthalpy and pre-factor for the most important Group III and V dopants in silicon are reported.
The n-type dopants enhanced diffusion are directly associated with the properties of the point defects involved in the diffusion mechanism: in the case of phosphorous, arsenic and antimony the mass transport is mediated by singly negatively charged donor- vacancy pairs [28]. Riihimäki et al. [29] suggest that in the diamond cubic structure a vacancy next to a substitutional impurity after a diffusion jump, has to move at least to a third nearest neighbour from impurity in order to cause another jump. Thus, if the attractive interaction potential between impurity and vacancy is sufficiently strong to extend to a third coordination site, it is possible for the impurity to diffuse as a pair with the vacancy.
Moreover the activation enthalpy for intrinsic condition decreases with increasing size of the n-type dopants indicating an increasing binding energy between dopant and vacancy. This trend is supported by ab initio calculations [30].
According to older studies on the diffusion of acceptor dopants - aluminium, gallium and indium, these elements diffuse several order of magnitude faster than boron. Moreover their diffusion activation enthalpies exceed the activation enthalpy of self-diffusion. Considering

the DFT calculation of Chroneos et al. [30], these results seem in conflict with the picture on vacancy-mediated acceptor diffusion. Kube et al. [31] explain this deviation between the experimental results and the theoretical prediction with an interaction of the dopants with vacancies on the second and third nearest neighbour site that for the three acceptor suggest to be repulsive.

Element	H (eV)	$D_0(cm^2/s)$	Technique	T range(° C)	Year	Reference
P	2.48	2.5	p-n junction	600-900	1954	[26]
	2.10	0.09	SIMS	600-900	1997	[32]
	2.07	0.0438	SRP	600-850	2003	[33]
	2.30	0.0185	SIMS	600-800	2007	[34]
	2.85	9.1	SIMS	650-920	2008	[28]
As	2.50	10	p-n junction	600-900	1954	[26]
	3.32	$1.45\ 10^6$	SRP	600-850	2003	[33]
	2.71	32	SIMS	650-920	2008	[28]
Sb	2.8	507	p-n junction	–	1967	[27]
	2.28	11.89	SRP	600-850	2003	[33]
	2.55	16.7	SIMS	650-920	2008	[28]
Al	3.2	100	p-n junction	750-850	1967	[36]
	3.45	1000	SIMS	554-905	1982	[35]
	2.2	$9.8\ 10^{-4}$	resonance	525-775	1982	[10]
Ga	3.0	10	p-n junction	600-900	1954	[26]
	3.31	140	SIMS	554-916	1986	[32]
	3.21	8	radiotracer	575-910	2007	[29]
In	2.78	10	radiotracer	510-880	1965	[37]
	3.63	$1.8\ 10^4$	SIMS	554-919	1982	[35]
	3.51	5123	SIMS	550-900	2009	[31]
B	4.6	$6\ 10^8$	p-n junction	600-900	1954	[26]
	4.5	$9.5\ 10^6$	sheet resist.	750-900	1967	[36]
	4.65	$1.97\ 10^5$	SIMS	800-900	2004	[49]

Table 1.3: *Activation enthalpy H and pre-exponential factor D_0 for diffusion in germanium.*

Element	H (eV)	$D_0(cm^2/s)$
P	3.66	3.85
As	4.1	22.9
Sb	3.65	0.214
Al	4.1	1.35
B	3.46	0.76
In	4.19	269

Table 1.4: *Activation enthalpy H and pre-exponential factor D_0 for diffusion in silicon for comparison (from R.B. Fair "Concentration Profiles of Diffuse Dopants in silicon").*

Boron deserves a paragraph apart, since it is the object of our study.
According to Uppal et al. [45], B behaves almost diffusionless: the low B diffusion is associated with a diffusion activation enthalpy that exceeds the value of Ge self-diffusion (table 1.1). Recent studies confirm the low diffusivity of boron either after annealing with Rapid Thermal Processing (RTP) and Flash Lamp (FLA) [39], or after Solid Phase Epitaxial Regrowth (SPER) [54]. The experimental works present in literature found an activation enthalpy compatible each other but a rather large variation in pre-factors, and this variation creates a great discrepancy in the diffusion values (figure 1.5). According to Hu's analysis [40] for diffusion via vacancy mechanism, the activation energy for impurity diffusion should be smaller or at most equal to that for self-diffusion. The high activation energy for B diffusion in Ge compared to self-diffusion can be taken as an indication of a different mechanism in respect to that for self-diffusion. Considering the estimated high enthalpy for self-diffusion in Ge via interstitials ($\sim$6.5 eV), an interstitial mechanism for B diffusion may be reasonable. On the other hand, in the case of vacancy mediated mechanism for diffusion, the high activation energy can be explained with a repulsive interaction between B and *V* due to local stress and/or charge states of the point defects involved in the defect reaction [31]. However, theoretical calculations by Delugas et al. [41] estimated the activation energy for B diffusion in Ge in the form of *B-I* (Boron-Interstitial) higher or equal to 4.3 eV, compatible with the experimental value.

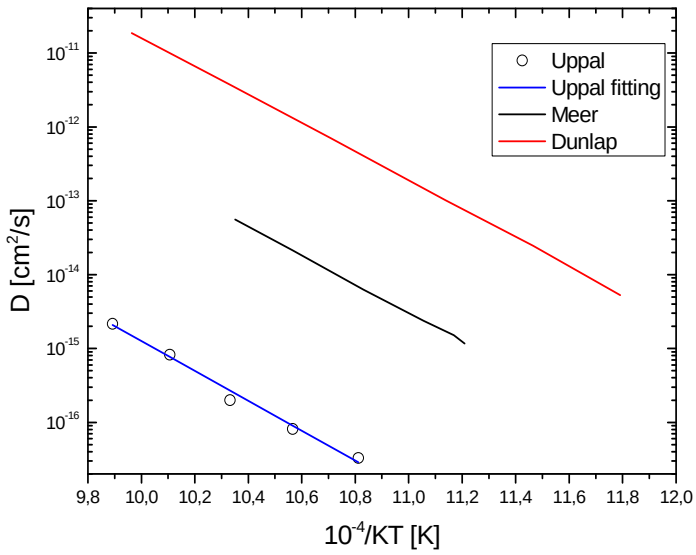

Figure 1.5: *Arrhenius curve for B diffusion in Ge (after [49]).*

1.4 Observations on Transient Enhanced Diffusion of B in germanium

In silicon, it is well known that boron diffuses through interstitials, whose concentration in equilibrium condition is low [42]. But when an excess of interstitials is present, for example after the annealing required for the recovery of the damage caused by ion implantation, boron in the tail of the implanted profile diffuses very fast (100 times faster than the normal thermal diffusion). This fast diffusion is due to Si interstitials, that "kick out" the substitutional boron atoms to interstitial positions where they can diffuse easily; alternatively the interstitials and boron atoms form highly mobile pairs to diffuse. After annealing for a sufficiently long time, the enhanced diffusion saturates: for this reason it is designated as *Transient Enhanced Diffusion* (TED). TED makes difficult to fabricate modern Si based devices because it can limit the fabrication of shallow junctions required for sub-100 nm complementary metal-oxide-semiconductor technology.
Since it has been reported that B diffusion in germanium is interstitial mediated as well [41], [49], it results fundamental for the development of shallow junction in Ge to determine whether TED phenomenon is present in Ge or not.
Some works reported on long tails in B profile implanted in crystalline Ge [44], [45], [54], similar to those seen for B implant in crystalline Si. However these tails are due to channeling effects, since they remain immobile during subsequent rapid annealing in the interval 400-700 $^{\circ}$C [54] (figure 1.6(a)), and for long annealing they show only the equilibrium thermal diffusivity [45], while TED in Si is stimulated by the annealings [46] (figure 1.6(b)). This suggests that B implantation doesn't create the interstitials necessary to sustain TED: indeed at Room Temperature the dopant ion beam itself induces self-annealing of the damage removing most of the implantation-induced defects [47].

Other works recently stated to have found evidences of TED during *rapid thermal annealing* (RTA) of 1 keV B implants performed on pre-amorphized Ge [43], [44] (figure 1.7). Pre-amorphization of the substrate is a methodology introduced firstly on silicon substrate just to avoid channeling effects and to raise the electrical active fraction of the implanted dopants, but it doesn't limit TED because pre-amorphization creates small clusters, at the End Of the implant Range (EOR), that rapidly dissolve for T $\geq$1000 $^{\circ}$C releasing an excess of interstitials. The results found in the work of Simoen et al. [44] are compatible with the picture depicted for silicon, since they observed a B diffusion identified as TED, for boron profiles that result completely contained into the amorphous layer, after annealing at temperature around 400 $^{\circ}$C (at 500 $^{\circ}$C the phenomenon saturates). However it is worth comparing the TED phenomenon in silicon (figure 1.6(b)) and what they observed in germanium (figure 1.8): while in the former the enhanced diffusion leads to an implant depth greater than 100 nm, in Ge the TED observed

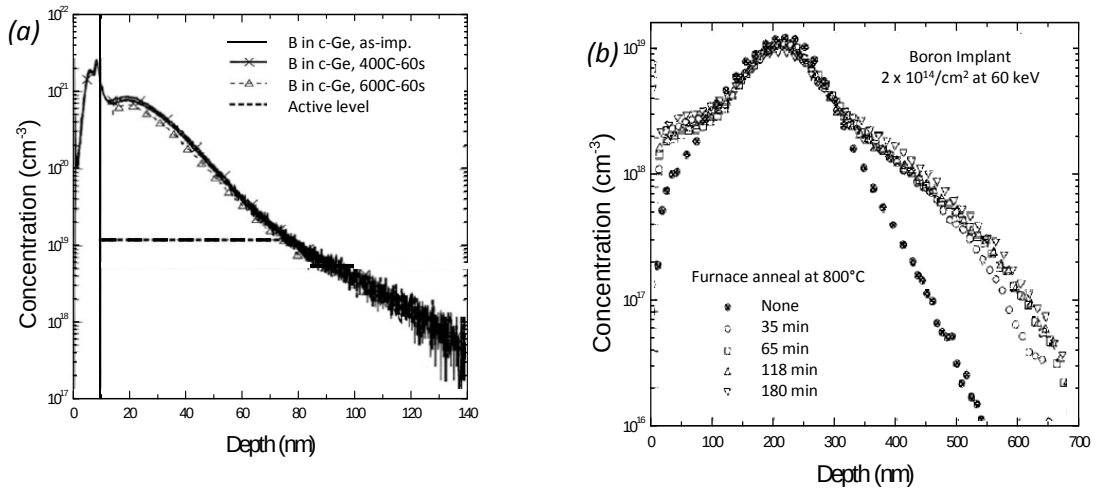

Figure 1.6: *(a) Chemical profiles of 6 keV* 3×10^{15} *atoms/cm*^{2} *boron, as-implanted, and annealed at 400 °C and 600 °C for 60 s, in crystalline Ge; (b) B profile in silicon for several annealing times at 800 °C [46].*

in ref. [44] is only a slight tendency.

However, the results presented in ref. [44] strongly suggest the presence of extended defects beneath the amorphous layer that dissolve around 400 °C, while at higher temperature the interstitial flux run out. The difference in the range of temperature for defects dissolution in Si and in Ge is probably related to the difference of melting temperature of the two substrates, and also to the "milder" structure of Ge compared to that of Si. The authors of ref.[44] investigated by Transmission Electron Microscopy (TEM) the existence of extended defects in pre-amorphized Ge, but they obtained only suggestions of the presence of clusters of point defects.

In any case the results of ref.[44] indicate that further investigations are necessary about the presence and the role of the defects created by ion implantation (both for doping and for amorphization).

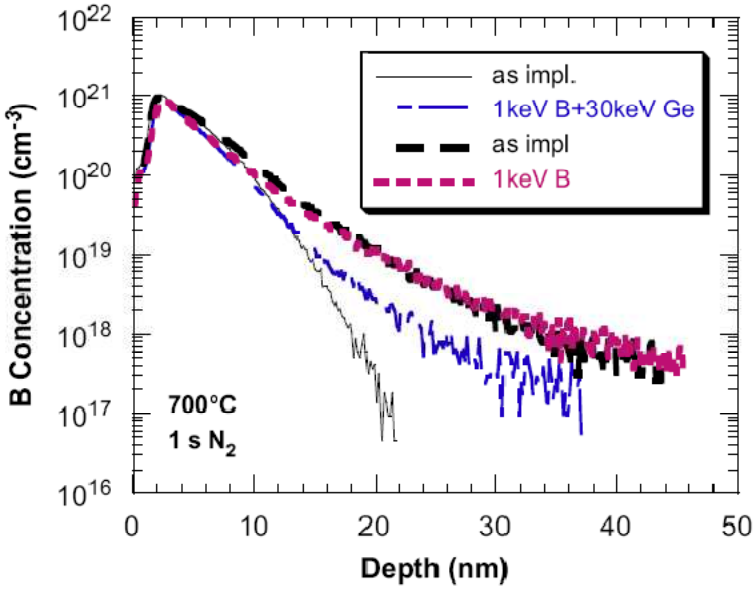

Figure 1.7: *SIMS profiles of B-implanted and pre- amorphized n-type Ge as-implanted (full black line) and after a 700 °C 1 s annealing (blue). This is compared with the corresponding profiles in crystalline Ge: as-implanted (black dashes)and annealed (red line) [44].*

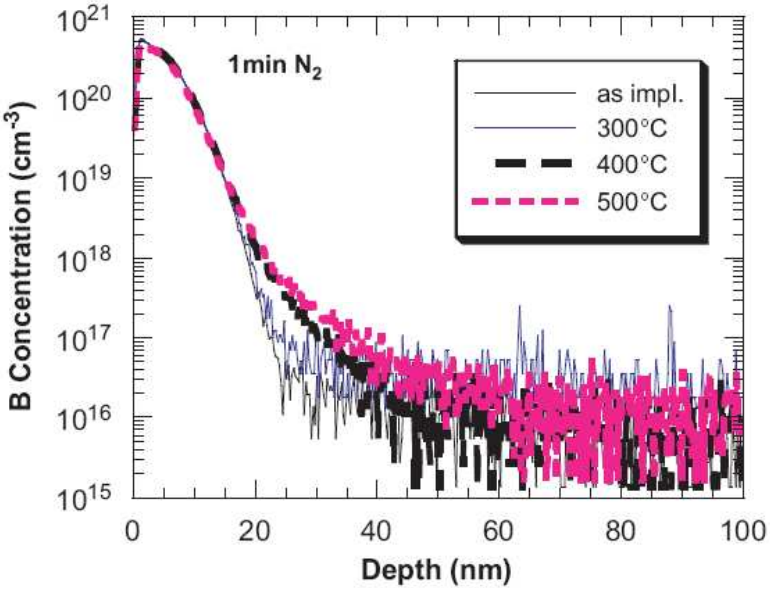

Figure 1.8: *SIMS profiles of 1 keV 5×10^{14} at/cm^2 B-implanted and pre-amorphized n-type Ge (30 keV, 10^{15} at/cm^2). As-implanted profiles are compared with the ones obtained after a 60 s annealing in N_2 at 300 °C (blue line), 400 °C (black dashed line)and 500 °C (red line) [44].*

1.5 Boron electrical activation and clustering

In the past, motivated also by the technological demand MOS device scaling, lots of theoretical and experimental efforts have been spent in order to understand which are the main properties that allows to obtain shallow source and drain junctions in Si. From Si experience, it has been found that the most desirable characteristics are a low dopant diffusivity and a high dopant solid solubility, that is the limit on the concentration of dopants absorbed by the host lattice at a given temperature. The same requirements are searched now for dopants in germanium.
The data available on dopants diffusivity in Ge have been already discussed in the previous section, from which boron appeared a good candidate for $p+$ junction fabrication, while a value for B solubility has not been well assessed.
A systematic investigation on solid solubility of various impurities in germanium as a function of temperature was performed by Trumbore in 1960 [48]; more recently Uppal et al. [45] determined a value for boron solid solubility of 5.5×10^{18} cm^{-3} in single crystal germanium at 850 °C (figure 1.9). This value is below the current technological requirement but it is related to the thermodynamic equilibrium, a condition that is not present when the dopants are introduced into the substrate, for example by ion implantation or diffusion.

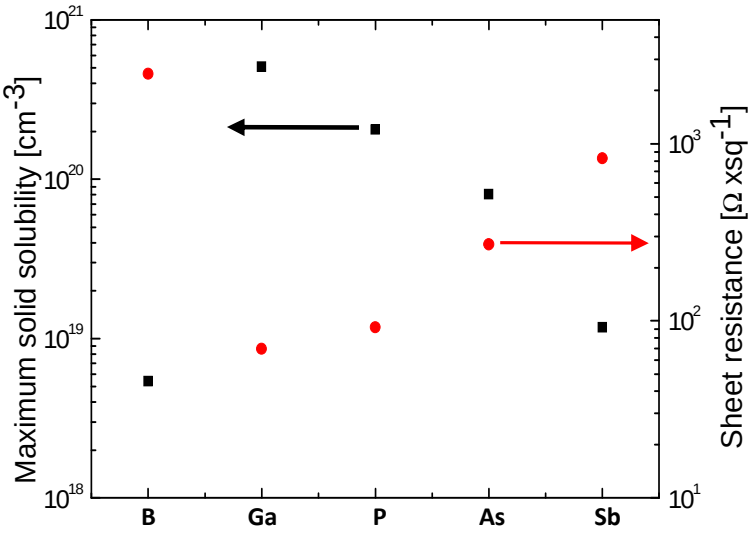

Figure 1.9: *Maximum solid solubility (open circles) and sheet resistance (full circles) corresponding to the junction depth X_j of 100 nm for dopants in germanium and assuming the activation levels given by the maximum solubility for each element [52].*

Indeed, in the case of ion implantation in crystalline Ge at high fluence regime, the concentration of active boron substantially exceeds the maximum solubility: already Gusev et al. [50] in 1974 found a concentration of electrically active boron above the limit of solubility, suggesting that the cause of this enhancement would be the boron implant damage itself. It is

important to remember the heavier damage caused by ion beam in Ge than in Si, also by light ions implantation like boron [67]. The implant damage has to be recovered by subsequent annealing in order to obtain high B substitutionality - that is high electrical activation [54], [50], [55], [45], [60], [59]. Jones and Haller [51] found high carrier concentration, i.e. a p-layer formation, even without annealing, but their results can be explained with p-type defect centers located near boron, rather than with boron itself.

Different methods can be used to anneal the sample and induce electrical activation. Some works reported on furnace anneals for B activation [49],[50], [53], but the samples described show only medium-level electrically activated concentration. Moreover this method uses relatively long thermal cycles, causing dopant diffusion and an implant profile deeper than 100 nm [53] (figure 1.10(a)). The thermal budget required for dopant activation in Ge can be obtained by Rapid Thermal Annealing (RTA) with better results, leading to an activation level in the $10^{19} - 10^{20}\ cm^{-3}$ range [33],[54], [53], [59] (figure 1.10(b)), and a sheet resistance of about 200 $\Omega/\square$, below the theoretical minimum shown in figure 1.9. Sheet resistance measurements, in combination with Hall effect, allow to directly obtain the carrier concentration as well as the mobility, and thus the electrically active doping concentration. In both annealing methods, B profiles show long tails due to channeling effect, in disagreement with the objective of shallow junction.

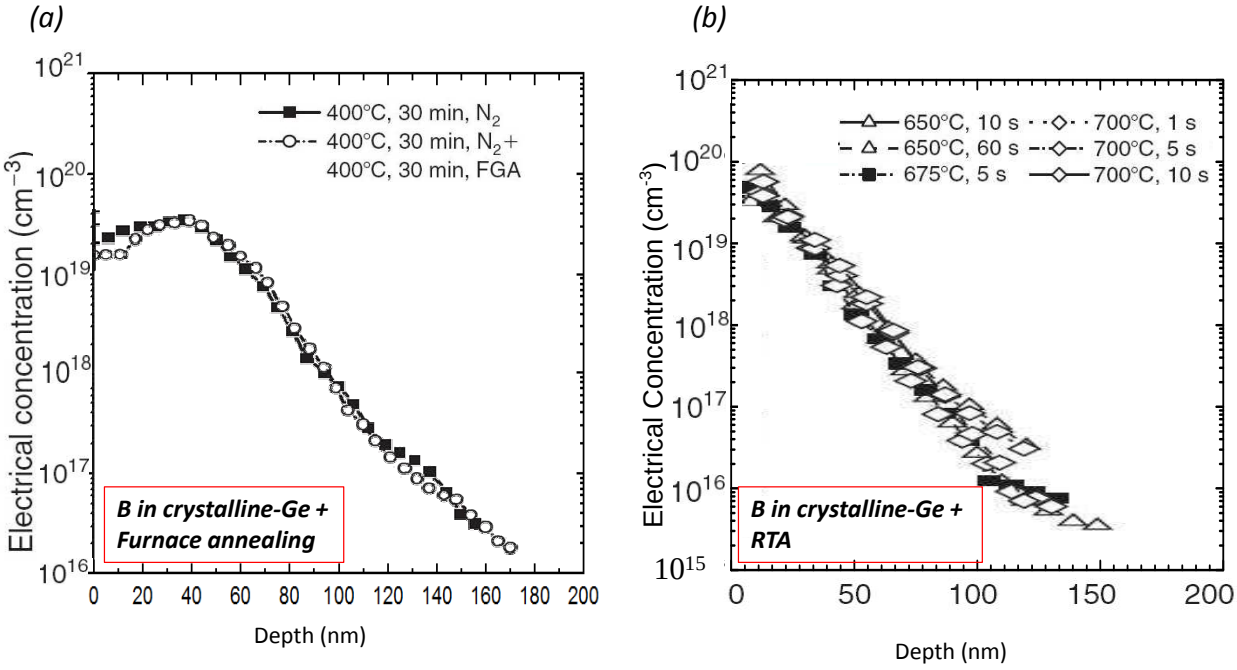

Figure 1.10: *(a) Electrical concentration measured on BF_2 implanted Ge samples and annealed in furnace; (b) electrical concentration measured on BF_2 implanted Ge samples and annealed by RTA processing at various conditions [53].*

Moreover, implantations in crystalline germanium and annealed either in furnace or in RTA, allow to activate only few percents of the implanted boron (figure 1.11(a)): according to Uppal et al. [49], and Satta et al. [54], [57], this can be explained with the formation of boron precipitates or clustering during implantation at the location of the highest boron concentration, that even after annealing at 600 °C remain present in the same position, indicating a higher thermal budget demand for their dissolution [57]. In this latter work these objects are clearly revealed by Cross-sectional Transmission Electron Microscopy as dark contrast regions located in correspondence of boron peak (figure 1.12), but the authors didn't provide details about the composition or the stoichiometry of these clusters [57].

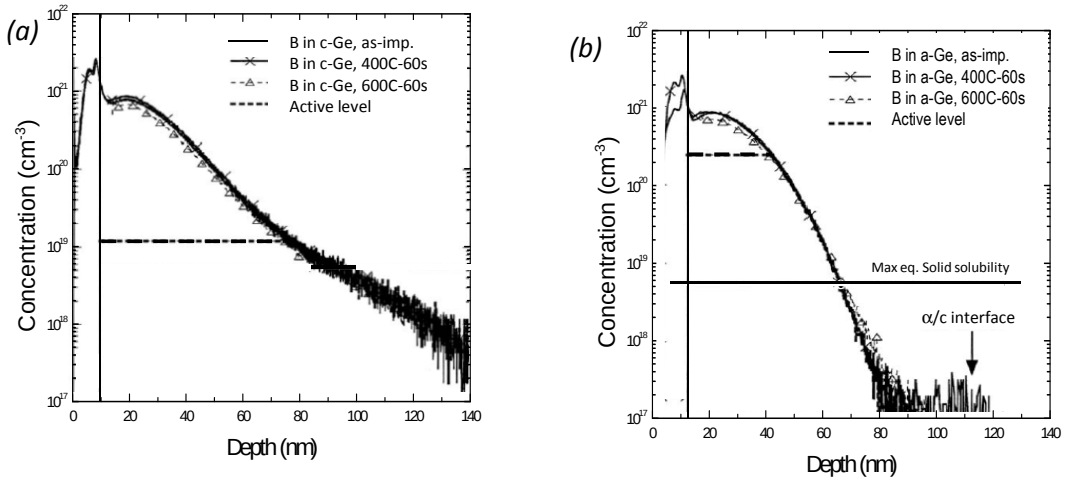

Figure 1.11: *Chemical profiles of as-implanted and annealed at 400° and 600° C for 60 s (a) in crystalline germanium and (b) in Ge pre-amorphized by a Ge implant of 100 keV energy to a dose of 1* $\times 10^1 5$ *atoms/cm*^{2} *[54].*

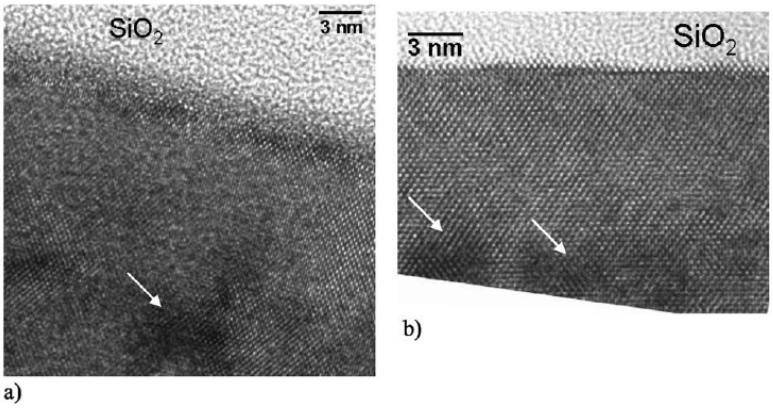

Figure 1.12: *Cross-sectional TEM micrographs of 6 keV* 3×10^{15} *atom/cm*^{2} *boron-implanted crystalline Ge, (a) as-implanted; (b) after annealing at 400 °C for 60 s [57].*

Very good results on B electrical activation have been obtained instead in Ge samples amorphized (*a-Ge*) before B implantation (the *Pre-Amorphized Implant* (PAI) method), and then regrown by Solid Phase Epitaxy - SPE (see next chapter for details of the method). B profiles are shallower than those obtained in crystalline germanium (*c-Ge*): in figure 1.11(a) and (b) a direct comparison of B profiles obtained in c-Ge and a-Ge is reported. Satta et al. [54] found an electrical activation level of 2.4×10^{20} cm^{-3} after a low temperature (400 °C) RTA, corresponding to ∼30% of the implanted B, while Chao et al. [60] obtained an electrically active boron concentration of $4.\times10^{20}$ cm^{-3}, after annealing in similar conditions. However, according to ref. [58], these B_{max} determinations rely on approaches (e.g. spreading resistance profiling or sheet resistance measurements coupled with secondary ion mass spectrometry) that suffer the lack of well-calibrated Ge standards and have to refer to some old concentration-dependent Hall mobility curves dated back to 1962.
Mirabella et al. [58] were able to obtain a higher value, equal to 5.5-5.8 $\times10^{20}$ cm^{-3}, corresponding to almost 100% of the implanted B, thanks to a systematic study on pre-amorphized Ge implanted with B in the high doping regime (10^{19}-10^{21} B/cm^3), and extracting the Hall factor. In addition, an accurate room-temperature concentration-dependent hole mobility curve has been reported.

Pre-amorphization is a well assessed method in Si, but it requires a strict control of a high number of parameters, like the energy, the ion mass, the fluence and the dose rate for the amorphization, and the substrate temperature during amorphization.
In germanium this procedure has to be deepened. For example, according to Mirabella et al. [58], it is possible to increase the active B level with the implant fluence, but only up to a certain value B_{max} determined by the parameters chosen for PAI and SPE. Raising up the implant fluence till overcoming B_{max}, dopant excess forms precipitates.
In the work of Chao et al. [60] it has been found that the electrical activation level depends on the energy of the Ge ion beam employed for the amorphization, i.e. on the amorphization depth. Indeed, if the amorphous layer is too much shallow, the subsequent boron implant can penetrate deeper in the sample, thanks to boron ion light weight, up to the amorphous/crystal interface where Ge atoms are got free (figure 1.13). Moreover boron implant can induce the layer re-crystallization (also called *beam induced epitaxial crystallization*), but the provided thermal budget is insufficient to anneal out defects formed during implantation, and higher temperature compared to that for SPE regrowth are required to dissolve these defects.
On the other hand, when the B profile is completely embedded into the amorphous layer, a low thermal budget is sufficient for the re-crystallization, thanks to an enhanced regrowth rate due to the presence itself of high levels of B doping [56], [57].

Pre-amorphization in silicon has some negative consequences on dopants diffusion, as already explained in paragraph 1.4. Therefore, in order to apply this methodology to Ge sub-

strates, it is necessary to understand if pre-amorphization causes the formation of small clusters, at the *End Of the implant Range* (EOR), and if they could have consequences on dopants. Satta and co-workers [54] analyzed PAI Ge samples both before and after annealing by TEM, revealing only a rough amorphous/crystal interface before crystal regrowth, and neither extended defects nor residual damage after the layer re-crystallization. Not even TEM images reported on ref. [60] revealed defects beyond amorphous/crystal interface (figure 1.13).

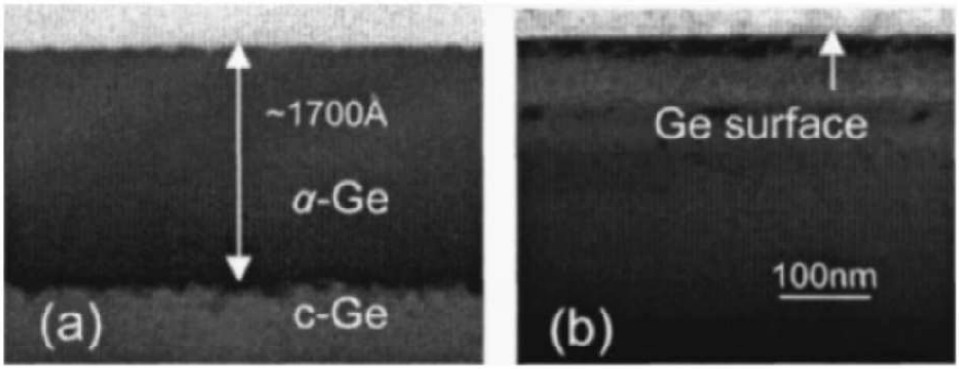

Figure 1.13: *CXTEM pictures of: (a) the sample amorphized with a 45 keV Ge ion beam: a 170 nm thick amorphous layer is visible, but not end of range defects; (b) the same sample subsequently implanted with 20 keV of boron ions: no end of range defects can be observed [60].*

The results in literature delineate a germanium substrate which behaves differently from its relative silicon in many aspects. This means that the absence of TEM observations about EOR defects cannot exclude a priori their existence, but it suggests rather their smaller size compared to the Si EOR defects, and for this reason difficult to observe directly by TEM. The results obtained about EOR defects presence in germanium have been reported on chapter 3.

Chapter 2

Methods

2.1 Solid Phase Epitaxial Regrowth(SPER)

The epitaxial regrowth is a thermally activated process that allows an amorphous layer positioned on a crystalline substrate to acquire the same crystalline structure of the substrate. It is thought to happen in a layer-by-layer fashion, with a motion of the amorphous/crystal interface towards the surface (figure 2.1); in the process the atoms, that in the amorphous layer possess only a short-range order, acquire the long-range order typical of a crystalline structure. The state of conversion is favored by a lowering of the system free energy [61].
SPER of a substrate following pre-amorphization via ion implantation is a procedure of fundamental and technological importance since being reported for the first time, more than 40 years ago [62], [63], [64].

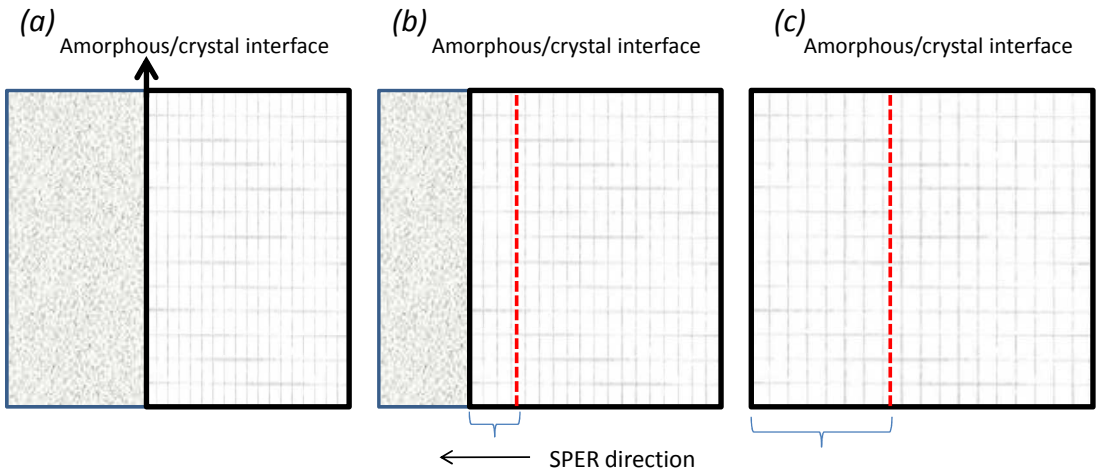

Figure 2.1: *Schematic of the SPER process showing (a) the as-implanted state (b) partial growth on an epitaxial layer, and (c) complete SPER resulting in a single crystal.*

Pre-amorphization before dopant implantation has the aim to avoid channeling phenomena of the implanted atoms that can produce a spread in the dopant concentration profile. Subsequent SPER of the amorphous layer allows dopant to change over to the electrically-active substitutional site during the regrowth process, while dopant diffusion within the lattice is minimized by the low temperature process (in Ge this temperature usually ranges from 300 to 550 °C, as reported in figure 2.2, in Si temperature ranges from 500 to 800 °C).
In Si pre-amorphization leads defects generation beyond the amorphous/crystal interface - the End Of Range defects (EORds). These defects can dissolve during SPER, releasing an interstitial (I) flux towards the surface. As a result of the interaction between the dopants and the Is, a transient and enhanced diffusion (TED) and clustering of dopants are observed. It is important to determine if these processes are present also in Ge: for this reason particular care is devoted to this argument.

SPER is temperature dependent and displays an Arrhenius-type behaviour [61]: in germanium, it is characterized by an activation energy of (2.0÷2.2) eV, in silicon by an activation energy of 2.7 eV.
The regrowth rate results influenced by the substrate orientation and by the presence of impurities: for example B doping enhances SPER rate both in Si and in Ge (in germanium the regrowth rate doubles with implanted B concentration up to 10^{20} cm^{-3} [63], [65], [66]).

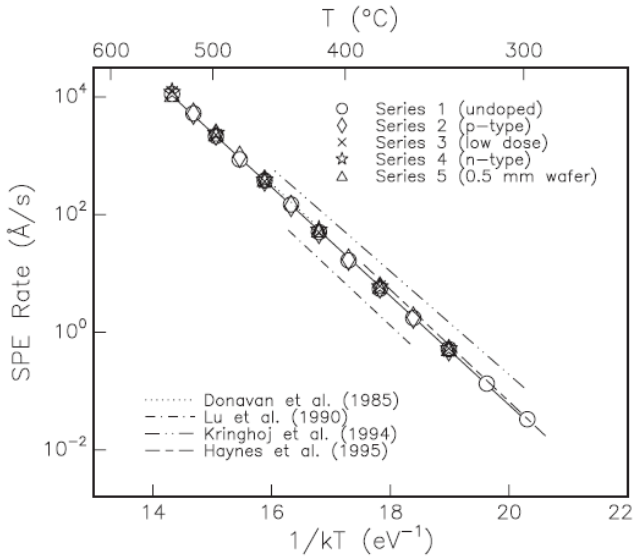

Figure 2.2: *The SPER rates for the various a-Ge layers displayed on an Arrhenius plot. Substrates are: series 1: undoped (∘), series 2: p-type (⋄), series 3: low fluence amorphization (×), series 4: n-type(⋆), and series 5: 0.5 mm thick substrate(△). The SPER rates reported in literature are also shown for comparison. These are plotted over the temperature range in which they were measured (after [66]).*

2.2 Rutherford Backscattering Spectrometry (RBS)

At the basis of the Rutherford Backscattering Spectrometry (RBS) technique there is the elastic collision between a beam of light particles with mass m_1 - usually ^{4}He ions with energies in the 1-2 MeV region - and the target atoms with mass m_2. At these energies the backscattering cross sections $\sigma(E,\theta)$ for the incident ^{4}He ions, on almost all elements more massive than Be, are described by the Rutherford formula:

$$\sigma_R(\theta,E) = \left(\frac{Z_1 Z_2 e^2}{4E}\right)^2 \cdot \frac{4\left[\sqrt{m_1^2 - m_2^2 sin\theta} + m_2 cos\theta\right]^2}{m_2 sin^4\theta\left(\sqrt{m_1^2 - m_2^2 sin\theta}\right)} \tag{2.1}$$

where θ is the scattering angle, Z_1 and Z_2 are the atomic numbers of the incident and target ions, respectively, and E is the incident particle energy. This equation implies that, for a given projectile, heavy atoms are much more efficiently scattered than light atoms. Therefore backscattering spectrometry is much more sensitive to heavy elements than to the light ones.

The energy and momentum conservation principles applied to the two-body collision permit to express the residual energy E_{out} of the projectile after collision as a function of the incident energy E_0 through the kinematic factor K:

$$E_{out} = K \cdot E_0 = \left[\frac{m_1 cos\theta + \sqrt{m_2^2 - m_1^2 sin^2\theta}}{m_1 + m_2}\right]^2 \cdot E_0 \tag{2.2}$$

Since m_1, E_0 and θ are determined by the experimental conditions, m_2 is individuated univocally and the target element at the surface is identified (figure 2.3).

The areal density (Nt), i.e. the number of atoms per unit area, for an element i^{th} in the sample is obtained from the detector solid angle θ, the integrated peak counts A_i, the number of incident ions Q and the cross section $\sigma_i(E,\theta)$, using the formula:

$$(Nt)_i = \frac{A_i cos\theta_i}{Q\Omega\sigma_i(E,\theta)}. \tag{2.3}$$

Many features of a backscattering spectrum are determined by the energy loss of the ingoing and outgoing ion beams crossing the sample. From the knowledge of the stopping power of a material for a particular ion (defined as the energy loss per distance covered into the target, *dE/dx*) it is possible to relate the energy of the scattered particles to the depth in the sample

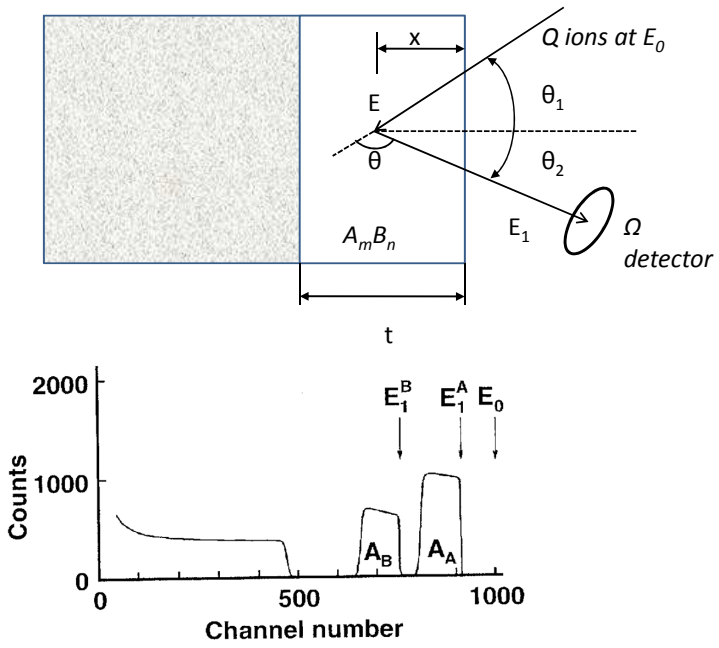

Figure 2.3: *Basic backscattering spectrometry. Experimental geometry (upper figure) and backscattering spectrum (lower figure) for a two element compound film (A_mB_n) of uniform composition on a low-mass substrate.*

where the scattering occurred:

$$\Delta E = \left[K \frac{dE}{dx}|_{in} \frac{1}{cos\theta_1} + \frac{1}{cos\theta_2} \frac{dE}{dx}|_{out} \right] \cdot x \tag{2.4}$$

It is important to underline that in cases of thin targets the stopping power can often be taken as constant, while in the case of thick targets a computer is usually used to calculate by numerical integration the energy of the ions at any depth below the sample surface.

As already explained, RBS suffers for poor sensitivity to detect light elements (i.e. B) in the range of a few atomic percent in heavier matrices like Ge: for example when a layer of a light element is positioned on top of a heavy substrate, then the RBS spectrum of the light element overlaps with the spectrum of the heavy elements, which forms a huge background. It is possible to overcome this difficulty by exploiting resonances of the elastic cross section or *Nuclear Reaction Analyses* (NRA).

In this work RBS has been used in order to investigate the lattice damage in the implanted and annealed samples. With this aim a channelling-RBS measurement along the $< 100 >$ axes has been performed, explained in paragraph 2.4. The dose and the substitutional fraction of B atom in the matrix has been measured by the $^{11}B(p,\alpha)^8Be$ nuclear reaction, described in the next paragraph.

2.3 Nuclear Reaction Analysis (NRA)

In this technique a beam of light particles, as p or α, with an energy in the MeV range is used in order to induce a nuclear reaction with the target atoms. To this aim the incident particles have to overcome the Coulomb barrier, and this is possible at these energies only with light target atoms. For this reason NRA technique is fundamental to detect small amount of impurities with low atomic mass contained in a substrate with higher atomic mass (i.e. B in Si or in Ge). Since in both RBS and NRA analysis usually light particles are revealed, the required equipment is basically the same and often these two measurements are performed at the same time using in a chamber two independent acquisition electronic chains for two solid state detectors connection. Since the reaction products usually have high energy, in order to stop and reveal them detectors with large sensitive depth should be used. Moreover the nuclear reaction cross section is usually much lower than that of RBS: this means that higher current must be used to obtain a good statistics, but this high current could cause pulse pile-up by backscattered particles and thus a high background on the NRA detector. But as the energy of the reaction products is generally higher than that of the backscattered particles, these particles could be eliminated by some filtering technique, for example an absorber foil (mylar).

In order to measure the implanted boron dose in Ge samples, the $^{11}B(p,\alpha)^{8}Be$ has been performed, using a 650 keV proton beam. This reaction has two reaction channels:

$$\begin{aligned} {}^{11}B + p &\rightarrow \alpha_0 + {}^{8}Be + Q(= 8.856 MeV) \\ &\rightarrow \alpha_1 + {}^{8}Be^{*} + Q(= 3.028 MeV) \end{aligned} \tag{2.5}$$

Thanks to its sensitivity this nuclear reaction is considered very attractive for different applications as the estimation of the total B amount and NRA/channeling for lattice location (for example in silicon the reaction revealed B impurity concentration of about 100 part per million atoms [68]). At 650 keV the nuclear reaction has a huge cross section for the α_1 channel (the differential cross section is in the order of 0.1 b/Sr).
Unfortunately, the broad resonance (Γ = 300 keV) and the production of energetic alpha particles of different energies (see figure 2.4) don't allow for depth profiling application with nanometric resolution.

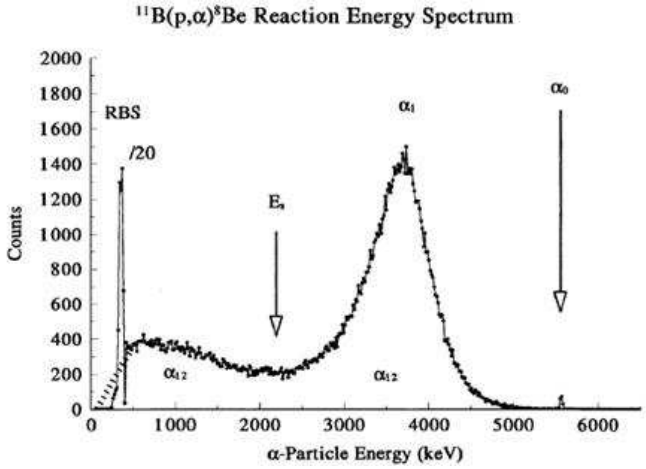

Figure 2.4: *Energy spectrum of* α *particles from* $^{11}B(p,\alpha)^{8}Be$ *reaction at the incident beam energy of 650 keV and detector at 150* $^{\circ}$ *[69].*

2.4 Channeling

Channeling is the steering of a beam of energetic ions into open spaces (channels) between close-packed rows or planes of atoms in a crystal [62].

The channeled ions feel the Coulomb barrier of the atoms bordering the channel, thus they cannot penetrate closer than the screening distance, and the probability of large-angle Rutherford collision or nuclear reaction is greatly reduced compared with the probability of the same interactions in case of non-channeled (random) beam. Consequently, when incident ions strike the crystal at a small angle ψ to a close-packed direction, a yield reduction is observed in the corresponding interaction spectrum (in figure 2.5 a RBS-channeling spectrum is compared with a non-channeled spectrum). Whenever there are atoms displaced from row or plane positions (for example for the presence of point defects or dislocations) channeled ions are gradually deflected out of channel by multiple scattering, then the yield increases.

Usually normalized yield χ is considered: it is the ratio of the yield for ions incident at an angle ψ (with respect to a crystal direction) to the yield for a randomly directed beam. A random spectrum is one for which the ion beam is directed in a random crystallographic direction, which does not exist except for an amorphous material. In order to avoid channeling effects in single crystals the sample can be rotated while random spectra are recorded, in this way the beam describes a cone around a given axial direction and planar channeling effects are averaged. Thus the normalized yield χ can be used to measure the fraction of de-channeled ions: when $\psi = 0$, the channeled fraction of the incident beam is maximum, and thus the yield of close-encounter processes in the corresponding spectrum is at its minimum value χ_{min} (its value typically ranges

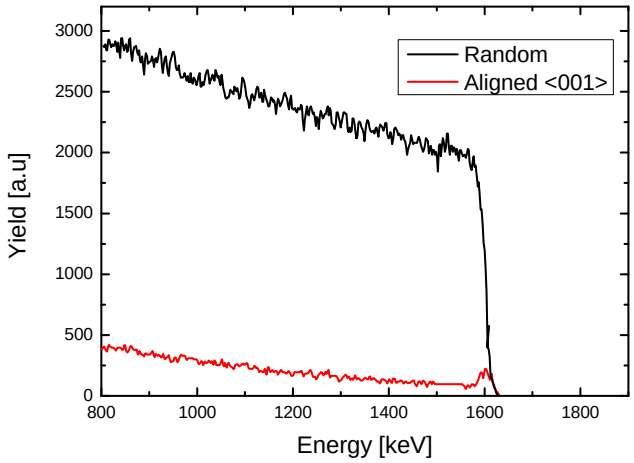

Figure 2.5: *RBS spectrum of a germanium sample collected in random (red line) and in channeling conditions along the* $[001]$ *(black line) with a 650 keV* He^{+} *beam. The scattering angle is* 150°.

between about 0.1 for planar channeling and about 0.01 for axial channeling); at larger angular deviations, the yield approaches the random value and then χ approaches to unity. Also if a near-surface layer of the crystal is completely disordered (i.e. amorphized) χ becomes equal to unity for that layer: measuring the energy increment ΔE over which $\chi = 1$ the thickness of the amorphous layer is determined (figure 2.6).

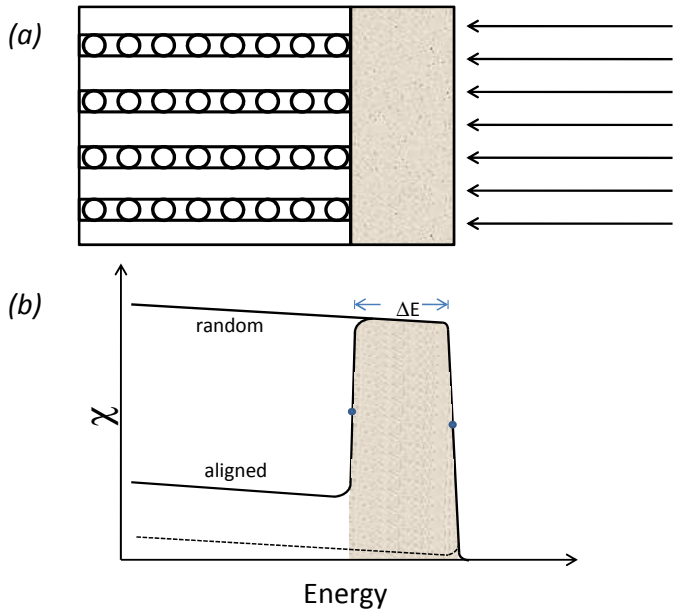

Figure 2.6: *(a) Schematic representation of an ion beam incident on a Ge crystal in which the outer layer has been rendered amorphous by ion implantation; (b) random and aligned spectra for the sample containing an amorphous layer (shaded region); an aligned spectrum for a perfectly crystalline substrate is also reported for comparison (dashed line) [70].*

In channeling measurements useful information can be obtained determining the ψ dependence of the yield χ of closed-encounter processes. In such measurements, the angle ψ is usually varied over a small range centered on the channel direction. This angular scan is called channeling dip (figure 2.7).

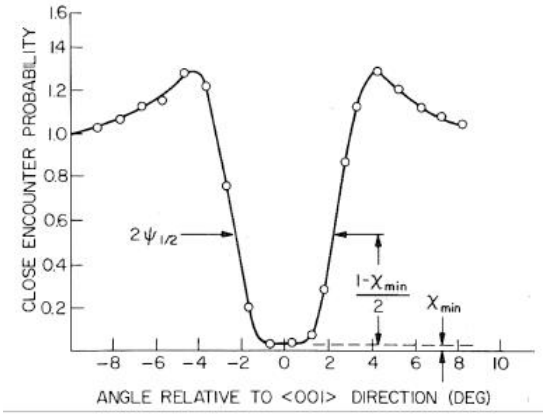

Figure 2.7: *Normalized angular yield profile as a function of the tilt angle(channeling dip).*

It is possible to deduce the position of solute atoms, i.e. impurities, in a crystal lattice by measuring a channeling dip for host atoms and impurity atoms. If the impurities are in the same lattice sites as the host atoms, then normalized yield for the host atoms χ_h is roughly equal to the normalized yield for the impurities χ_i for any ψ (figure 2.8(a)). However if the impurity atoms project into the channel (indicated through generic Miller indices $< uvw >$), the channeled ions interact with them causing an increase in the yield χ_i: for small projections the dip in yield for impurities is narrower than that for host atoms (figure 2.8(b)), while for large projections small double peaks or small central peak may be observed (figure 2.8(c)). When the impurities are positioned at the centre of the channel (i.e. interstitial position) a large peak appears in the yield for impurities dip; for randomly located impurities, a flat profile of χ_i is observed (figure 2.8(e)). By comparing yields from different channels, the position of solute atoms can be determined rather accurately by a triangulation procedure.
A useful quantity that can be calculated from host and impurities minimum yields is the substitutional fraction of the impurity atoms in the host lattice:

$$f = \frac{1-\chi_d^{<uvw>}}{1-\chi_h^{<uvw>}} \tag{2.6}$$

This equation assumes a simple model of channeling, in which the impurities are randomly located into the host lattice, without considering intermediated or mixed situations (as for example figures 2.8(f) and (g)).

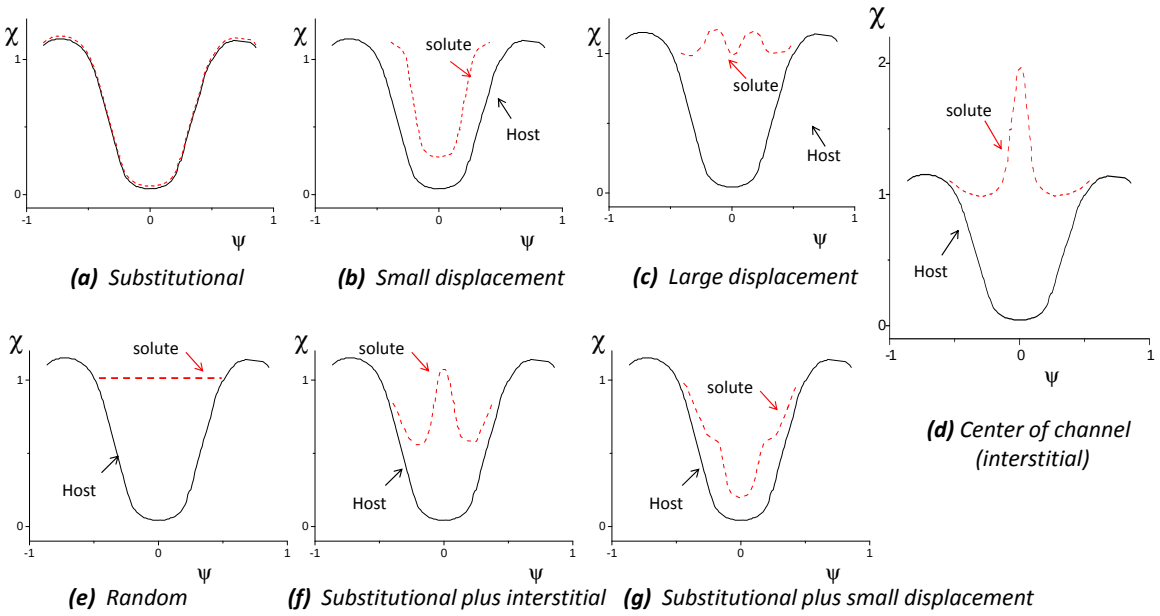

Figure 2.8: *Angular scans for different projections of a solute atom into an axial channel (from [62]).*

2.5 Secondary Ion Mass Spectrometry (SIMS)

It is an analytical technique extremely sensitive to the impurities coming from surface and near surface (up to 30 μm) region of solids with sensitivity limits in the part per billion (ppb) to part per million (ppm) range for almost all the elements. The technique uses a beam of energetic (0.5-20 keV) primary ions (for example O_2^+, O^- or Cs^+) to sputter the sample surface and producing ionized secondary particles (mono-atomic and poly-atomic particles of the sample material and re-sputtered primary ions along with electrons and protons).

This secondary beam passes through an electrostatic analyzer and then through a magnetic mass spectrometer. Varying the magnetic field on the spectrometer it is possible to select different species thus obtaining a mass spectrum.

Depth profiles are obtained bombarding the same point on the sample and monitoring the secondary ion counting rate of the selected element as a function of time. To convert time axis to depth, a profilometer has to be used. Depth resolution is of the order of few nanometers.

Quantitative SIMS analysis requires a standard material from which to measure *Relative Sensitivity Factor* (RSF) value: since the yield depends on the incident element, on the sputtering species and on the sample matrix, separate RSF values must be measured for each element analyzed.

The SIMS measurements shown in this thesis are obtained from a CAMECA IMS-4f spectrometer. In order to detect B, a 3 keV O_2^+ primary beam has been used. For calibration, both germanium and silicon substrates have been measured under the same conditions: these sub-

strates have been implanted at the same time with the same nominal B dose of 4.175×10^{14} B/cm^2 at 68 keV. B dose in silicon was calibrated by comparison with a NIST certified standard (accuracy $\sim$5%).

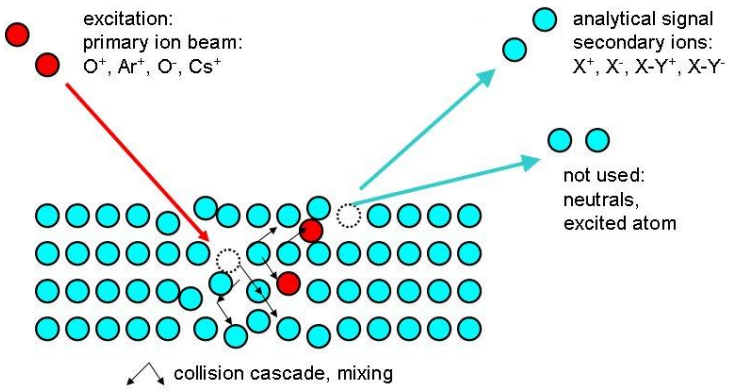

Figure 2.9: *SIMS physical principle.*

2.6 High Resolution X-Ray Diffraction (HRXRD)

High Resolution X- Ray Diffraction (HRXRD) is a non-destructive technique that can be used to determine thickness, lattice parameter, strain, composition and defect presence in crystalline materials.

X-Ray Diffraction technique consists in probing a crystal sample with an X-ray radiation with a wavelength λ close to the lattice spacing, as shown in figure 2.10(a). The X rays are then scattered by the electron cloud surrounding each atom in the crystal.

X-Ray Diffraction can be simply described by the Bragg's law, which affirms that constructive interference occurs between two scattered X rays striking the crystal planes at an angle θ, if the path difference AB is an integer number (n) of wavelengths, i.e. $n\lambda$ (figure 2.10(a)). Then this law relates the spacing between the planes of atoms from which diffraction occurs d, to the angle θ at which the incident beam must strike the planes to give constructive interference:

$$n\lambda = 2dsin\theta \tag{2.7}$$

Each set of crystal planes produces a diffraction spot: the crystal planes are associated with the real space, while the diffraction spots with the reciprocal space, forming a reciprocal lattice. Therefore diffraction can be illustrated also in the context of the reciprocal lattice. If the incident (k_0) and the diffracted (k_h) beam vectors make appropriate angles with respect to the crystal, the scattering vector **S** (equal to k_h-k_0) will end at a reciprocal lattice point (figure 2.10(b)).

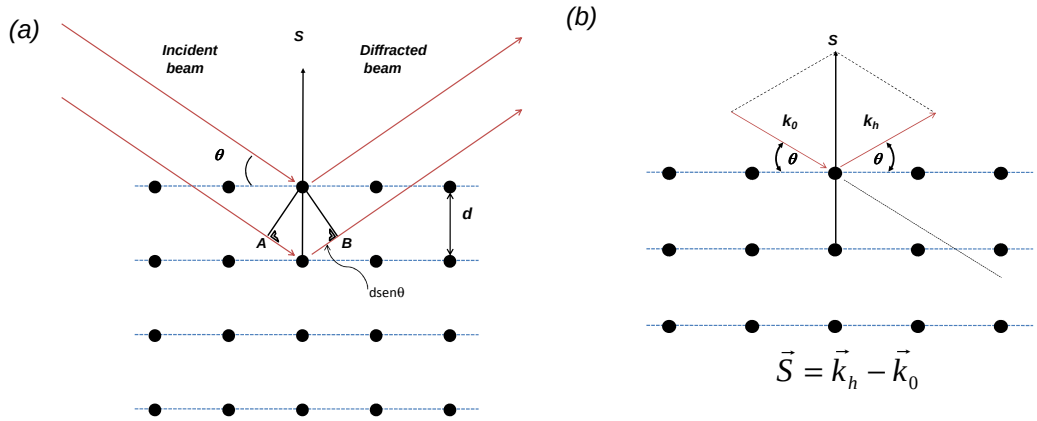

Figure 2.10: *Schematic of x-ray diffraction: (a) illustration of the conditions required for Bragg diffraction to occur and (b) relationship of the incident (k_0), diffracted (k_h) and scattering (**S**) vectors with respect to the crystal. Planes of atoms are indicated by dotted lines: these are not necessarily parallel to the sample surface.*

The diffraction event described in reciprocal space can be illustrated by means of the *Ewald sphere* construction (blue circles in figure 2.11(a)): this is a sphere with radius 1/λ drawn through the origin of the reciprocal lattice, indicated by the starting point of the incident beam vector k_0. The Ewald sphere shows which part of reciprocal space **S** can explore, given a particular wavelength λ and an angle θ. Where the sphere touches a reciprocal lattice spot, diffraction occurs. Not all diffraction spots can be accessed: the larger circle in figures 2.11 shows the outer limit which can be reached with **S** for the given λ and θ. The grey shaded areas show the regions where either the incoming or the outgoing beam is blocked by the sample presence. The length of **S** can be altered changing 2θ, the angle between the incident and diffracted beams. The direction, or orientation, of **S** is scanned by changing ω, the angle at which the incident beam meets the sample surface: the value of ω is different from that of θ - the angle at which the incident beam meets a crystal plane - when the planes are not parallel to the sample surface. In general, if ω is equal to θ, then the reflection is called *symmetrical* (as in figure 2.11(a)), otherwise it is called *asymmetrical reflection* (figure 2.11(b)).

The most precise theory that describes the X ray diffraction phenomenon is the *dynamical theory* of diffraction, which considers the wave field in the periodic potential of the crystal and takes into account all multiple scattering effects [71]. However, a more intuitive description of the X-ray diffraction is provided by the so called kinematic theory, which assumes that no energy is transferred to the diffracted beam: this assumption is adequate for most purposes, but it breaks down at low angles and for highly perfect samples. Hereafter the kinematical approach is adopted in order to describe the main features of a diffraction spectrum, while more precise information are extracted with the help of simulation codes which take into account the dynamical theory of X-ray diffraction.

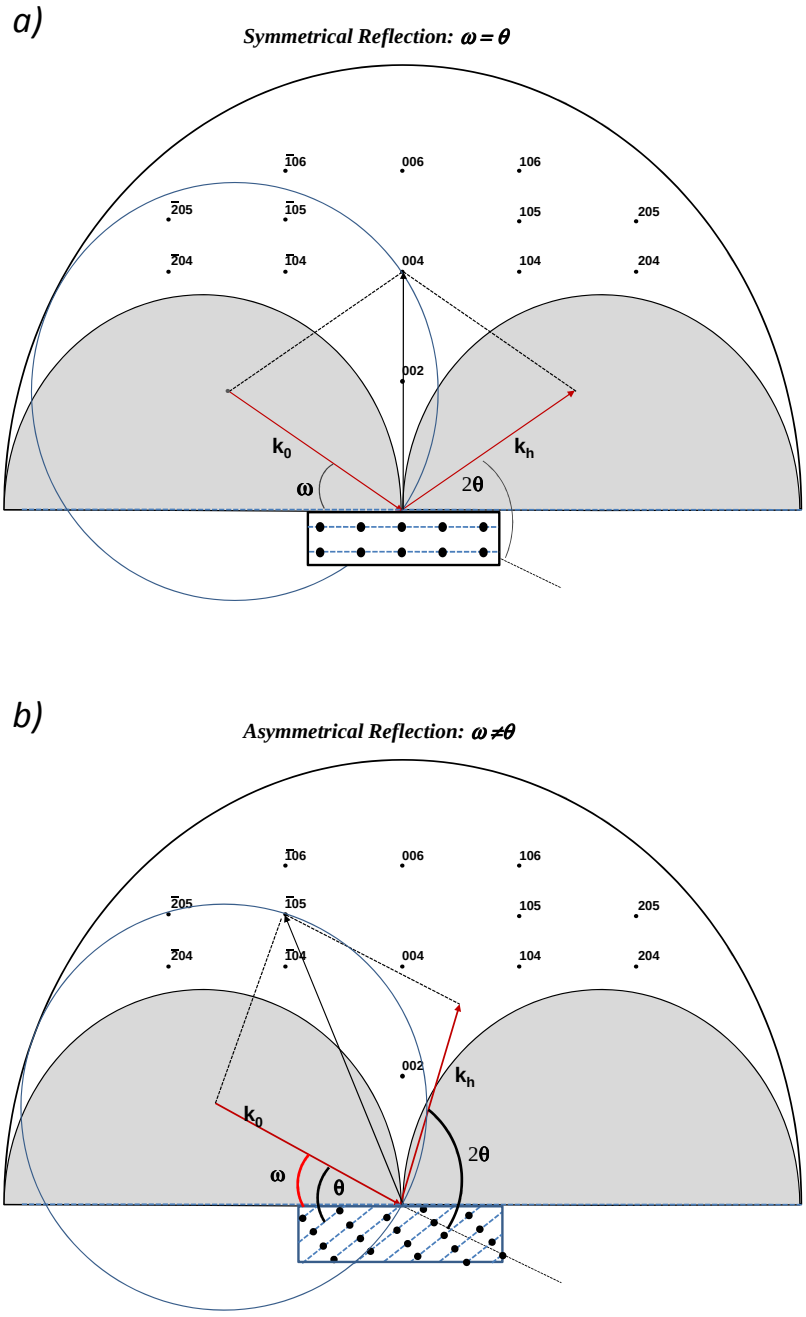

Figure 2.11: *(a) Section through reciprocal space for a* $[001]$*-oriented Ge crystal: the atoms planes are parallel to the surface, in this case* $\omega = \theta$ *and a symmetrical reflection is used. The Ewald sphere is shown here as a blue circle, cutting the 004 reciprocal lattice spot. (b) In order to explore atoms planes not parallel to the surface* ($\omega \neq \theta$) *asymmetrical reflection has to be used.*

2.6.1 High Resolution experimental apparatus and scan types

The lattice parameter measurements performed in this thesis require elevated precision so that to detect a relative lattice variation of the order of $10^{-2} \div 10^{-5}$. This means that the probe must consist of a monochromatic beam with a low divergence δ:

$$\frac{\Delta d}{d} = \frac{\Delta\lambda}{\lambda} + \frac{\delta}{tan\theta} \tag{2.8}$$

where d is the interplanar spacing, $\Delta\lambda$ is the wavelength spread of the radiation, δ is the incident beam divergence and θ is the diffraction angle.
Clearly, a diffractometer capable of providing low δ and $\Delta\lambda$ is required. The X ray source, a Cu anode sealed tube, generates a divergent beam (δ typically $\sim 0.5^\circ$) with a considerable $\Delta\lambda$. To convert the divergent beam to a nearly parallel beam a parabolic bent graded multilayer mirror is used ($\sim 0.3^\circ$), thus reducing the broadening in ω and increasing the intensity (typically by a factor of 10). In order to reduce $\Delta\lambda$ and δ a Bartels monochromator is positioned after the mirror: this element consists in two (220) channel-cut germanium crystals.
If no other element is added to this instrument than a Xe gas proportional counter detector, we have the so-called double axis configuration, with an angular acceptance of 1°. The acceptance can be reduced further by putting slits in front of the detector: the minimum value in the apparatus used in this work is $1/32^\circ$.
Adding an analyzer crystal before the detector to define the direction of 2θ, an instrument with a better 2θ resolution and a better ratio between good signal and noise can be obtained, but on the other hand the analyzer reduces the intensity and makes difficult the alignment. This configuration is called triple axis.
The measurement has to be collected under an adequate thermalization condition: all the apparatus is thus positioned inside a cabinet where the temperature is strictly controlled within $\pm 0.1^\circ$C.
A scheme of the X-ray apparatus used in this work is reported in figure 2.12.

The sample is mounted in a goniometer which allows to perform different scans:

- ω-*scan*: the detector remains stationary and the sample is rotated so as to vary the omega value. The length of **S** stays the same, but its direction changes. It allows to measure the film quality by scanning in the reciprocal space the diffraction spot in an arc, detecting broadening by dislocations and wafer curvature (in figure 2.13 the explored diffraction node, indicated through the Miller indices (hkl), is crossed in the direction indicated by the arrow). The minimum available step for this angle is of 0.0001° = 0.36 arcsec, while the reproducibility was tested to be about 0.0002° and the accuracy of 0.001°;

- 2θ *scan*: the sample remains stationary and the detector is moved. **S** traces an arc along

the circumference of the Ewald sphere (figure 2.13). The angular movement is identical to the previous from a construction point of view, so it has the same specification;

- φ *scan*: rotation of the sample about the φ axis in the plane of the sample, perpendicular to the sample surface;

- Ψ *scan*: similar to φ scans, except that the sample is rotated about the ψ axis, parallel to the sample surface;

- ω-2θ *scan*: the sample is rotated by ω and the detector is rotated by 2θ with an angular ratio of 1:2. The length of **S** changes, but its direction remains the same (figure 2.13).

The ω-2θ scans are called "rocking curves", as involve "rocking" the sample.

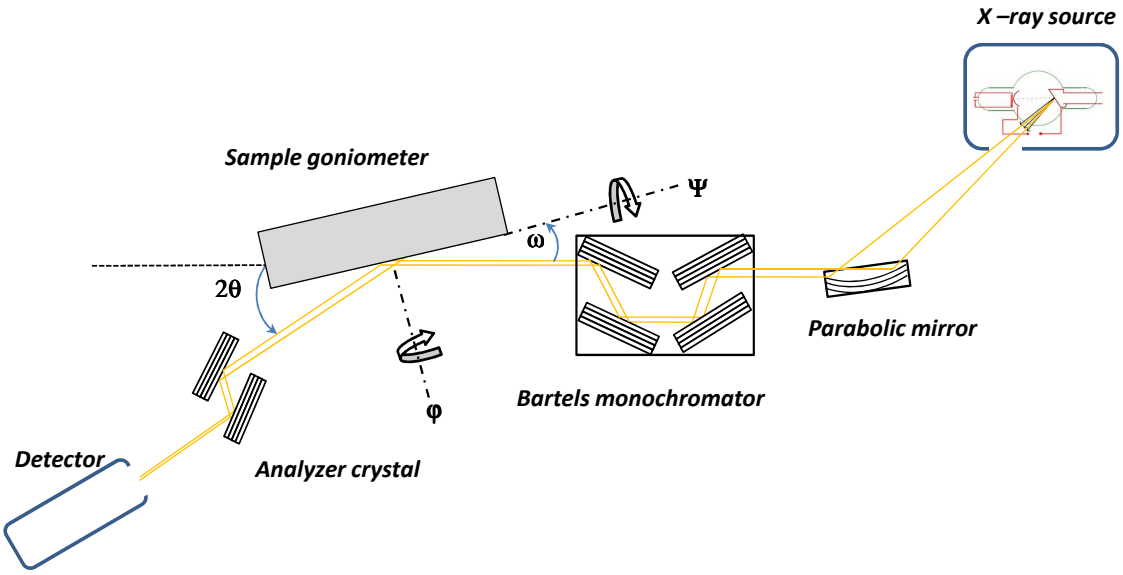

Figure 2.12: *High resolution X-ray diffraction apparatus in our laboratory.*

Much information regarding interplanar spacings and defect-related broadening can be summarized in *Reciprocal Lattice Maps* (RLMs), which show a 2D section through reciprocal space (the intensity shown in RLMs is normally a projection of the 3D intensity of the diffraction spot(s) onto a 2D plane). A reciprocal lattice map can be obtained by taking an ω-2θ scans at different ω values; the results are presented in the form of iso-contours plots.

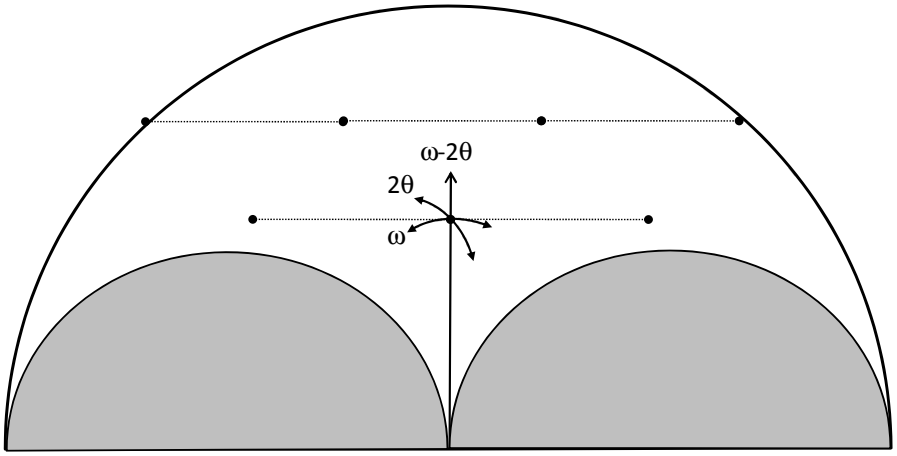

Figure 2.13: *The directions taken by different scan types (ω, 2θ and ω-2θ) in reciprocal space.*

2.6.2 Sample definition and macroscopic deformation: epitaxial structure

When a film is epitaxially grown over a substrate with a different lattice parameter (figure 2.14(a)), the layer atoms tend to adjust themselves in order to reproduce the same crystalline structure of the substrate, undergoing to elastic distortions.
Limiting the description to the tetragonal distortion undergone by cubic film (since Ge belongs to cubic system), the epitaxial layer is pseudomorphically grown if it possesses a lattice parameter in the interface plane ($a_{||}$) equal to that of the substrate (a_s), while the lattice parameter normal to the interface plane ($a_{\perp}$) can distorted, following the Poisson ratio (defined below): when $a_{\perp} < a_{||}$ the layer is affected by compressive strain (shown in figure 2.14(b)); when $a_{\perp} < a_{||}$ the layer is affected by tensile strain.
If the layer overcomes the so called critical thickness (the maximum thickness for which the strain energy is accumulated leading to only elastic deformation), plastic deformation and (misfit) dislocations can be generated and a partial (figure 2.14(c)) or full relaxation (figure 2.14(d)) can be observed.
The relaxation degree of the layer is defined as:

$$R = \frac{a_{\perp} - a_s}{a_{rel} - a_s} \tag{2.9}$$

where a_{rel} is the lattice parameter of the fully relaxed layer.

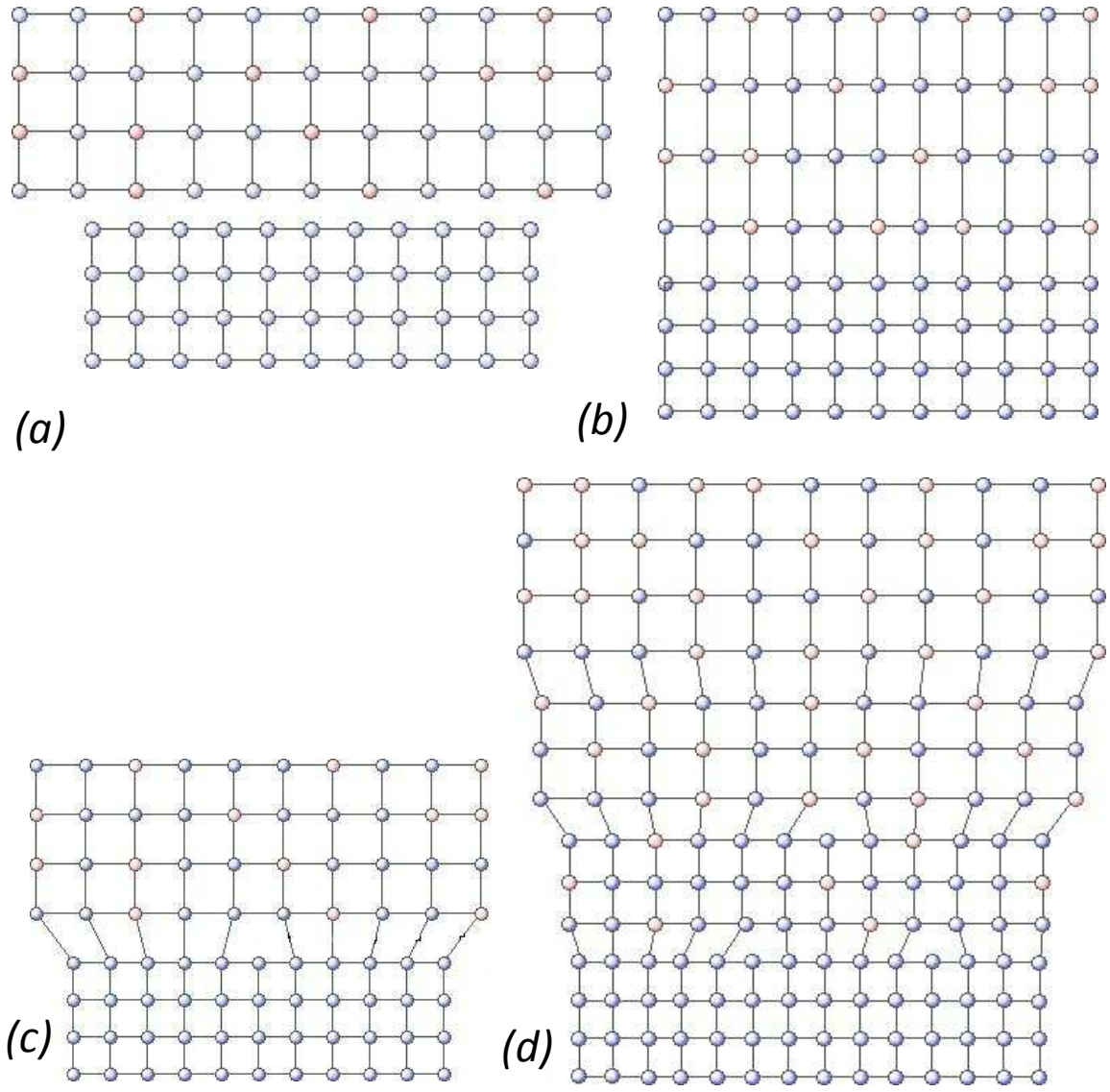

Figure 2.14: *(a) The undistorted (before deposition) and (b) distorted (after deposition) cubic layer on a cubic substrate; when lattice parameters are incapable of accommodating the distortions necessary for perfect epitaxy there could be (c) a partial relaxation and dislocations appear; (d) full relaxation.*

The epitaxial constrains can be described accurately examining the relationship between stress and strain, expressed by Hooke's law. Referring to a cubic system grown along the $< 001 >$ direction, the stress normal to this direction σ_{zz} is zero, therefore:

$$\sigma_{zz} = 0 = c_{12}\varepsilon_{xx} + c_{12}\varepsilon_{yy} + c_{11}\varepsilon_{zz} \tag{2.10}$$

$$\varepsilon_{zz} = -\frac{c_{12}}{c_{11}}(\varepsilon_{xx} + \varepsilon_{yy}) \tag{2.11}$$

where c_{ij} are the stiffness coefficients and ε_{ij} the strain tensor along various directions.
In a cubic system the strain tensor has only two components:

$$\varepsilon_{\parallel} = \varepsilon_{xx} = \varepsilon_{yy} = \frac{a_{\parallel} - a_{rel}}{a_{rel}} \tag{2.12}$$

$$\varepsilon_{\perp} = \varepsilon_{zz} = \frac{a_{\perp} - a_{rel}}{a_{rel}} \tag{2.13}$$

In the case of tetragonal distortion as in figure 2.14(b), the Poisson ratio can be used:

$$\nu = \frac{\varepsilon_{\perp}}{\varepsilon_{\perp} - 2\varepsilon_{\parallel}} = \frac{c_{12}}{c_{11} + c_{12}} \tag{2.14}$$

For most crystals, the ν value is near 1/3 (0.26 for Ge, 0.28 for Si, 0.311 for GaAs).
Then it can be written:

$$\varepsilon_{\perp} = -\frac{2\nu}{1-\nu}\varepsilon_{\parallel} \tag{2.15}$$

In order to understand the direct relation between what it is measured during a diffraction experiment and the strain of the sample, the equation 2.15 is re-written in the following way:

$$\varepsilon_{\parallel} = -\frac{1-\nu}{1+\nu}(\varepsilon_{\perp} - \varepsilon_{\parallel}) \tag{2.16}$$

Multiplying each side by (a_{rel}/a_s), and remembering that for pseudomorphic layers $a_{\parallel} = a_s$ one obtains:

$$\frac{a_s - a_{rel}}{a_s} = -\frac{1-\nu}{1+\nu}(\frac{a_{\perp} - a_s}{a_s}) \tag{2.17}$$

The second term (defined as perpendicular mismatch $m_{\perp}$), can be express as a function of $\Delta\theta$ (the distance between the layer and the substrate Bragg peak) from the differentiation of Bragg equation (eq.2.7):

$$\frac{a_{\perp} - a_s}{a_s} = -\frac{\Delta\theta}{tan\theta_B}. \tag{2.18}$$

From the measurement of $\Delta\theta$ it is possible to obtain the information also about strain and lattice

parameter value of the layer in relaxed condition:

$$a_{rel} = a_s \left(1 - \frac{\Delta\theta}{tan\theta_B} \cdot \frac{1-\nu}{1+\nu}\right) \tag{2.19}$$

In figure 2.15 an example of an experimental diffraction measurement coming from a $Si_{1-x}Ge_x/Si$ sample is reported: in this spectrum two peaks are easily distinguishable, because of the difference between the film and substrate lattice parameters. From the relative positions of the layer and the substrate peaks it is clear that a situation of compressive strain ($a_\perp > a_{||}$) is present. The calculation of the intensity of the two peaks must be performed in the framework of the dynamical scattering theory. Nevertheless a good rule of thumb for the identification of the peaks is that the less intense peak is related to the thin layer while the most intense peak corresponds to the thick substrate. Moreover, the intensity of the thin layer peak is related to the film thickness: the thicker is the film, the more intense is its diffraction peak.

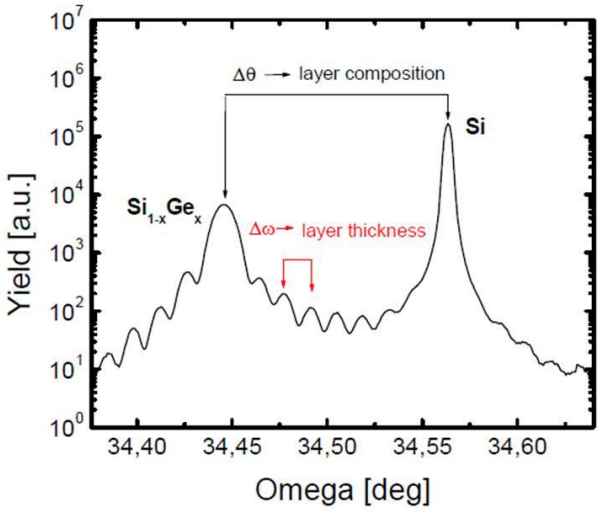

Figure 2.15: *Experimental diffraction spectrum of a $Si_{1-x}Ge_x/Si$ sample. From the knowledge of the distance between the peaks $\Delta\theta$ and the period of the fringes $\Delta\omega$ the composition and the thickness of the layer can be obtained.*

In figure 2.15 also small oscillations around the peaks are visible: these are called *interference fringes*. It is possible to obtain an estimation of the thickness t of the layer measuring $\Delta\omega$, the interference peaks separation:

$$t = \frac{\lambda}{2\Delta\omega cos\theta_B} \tag{2.20}$$

where θ_B is the Bragg angle.

The equation has the advantage not to contain anything about the material or about the diffraction conditions other than the Bragg angle and the geometry: this is because the refractive index for X rays is close to unity. If more than one layer is present, the pattern of the interference

fringes becomes quite complicated for the superimposition and the beat.

For most semiconductor systems the composition follows the Vegard's rule, i.e. the lattice parameter of the alloy $A_{1-x}B_x$ is given by the sum of the lattice parameters of all the components, A and B, each multiplied by their concentrations:

$$a_{A_{1-x}B_x} = a_A + (a_B - a_A) \cdot x = a_A + \Delta a \cdot x \tag{2.21}$$

This application of Vegard's rule requires to know the lattice parameters for both the components of the alloy. In some cases this is not possible, thus it is necessary to define a fictitious cubic lattice parameter.
From a single rocking curve measurement also the alloy composition can be estimated: the link between the lattice deformation Δa due to the epitaxial growth of the alloy layer $A_{1-x}B_x$ and the experimental measurement of the perpendicular strain with a (004) symmetrical reflection is expressed by the following equation:

$$\varepsilon_\perp = \frac{a_\perp - a_{A_{1-x}B_x}}{a_{A_{1-x}B_x}} = \frac{2\nu}{1-\nu} \cdot \frac{x \cdot \Delta a}{\rho_s a_s} \tag{2.22}$$

where ρ_s is the atomic density of the substrate and a_s the lattice parameter of the substrate.
The measurement of peak-to-peak distances and of interference fringes can give all these information in presence of a single layer with a homogeneous composition as a function of depth. But in many cases this this is not true: thus the rocking curves induced by a strain that changes as a function of the depth can be interpreted correctly imaging a superimposition of thinner layers with different lattice parameters and thicknesses. This is the approach implemented in the dynamical simulation software BEDE-RADS MERCURY [72], used in this thesis: the free parameters, i.e. the lattice parameter and thickness of each inserted layer are adapted during a "trial and error" procedure until the residuals, i.e. the difference between the experimental and the simulated data, are minimized.

2.6.3 Experimental diffraction measurement: thin layer between two thick layers

When a very thin layer interposed between two thick layers of another material as in figure 2.16 (for simplicity B_1 and B_2 have the same composition), the sandwiched layer A is too thin to give an independent Bragg peak like that showed in the previous paragraph. It is only able to act as a dephaser for the waves scattered from the substrate B_2 and the waves scattered from the thick cap layer B_1.

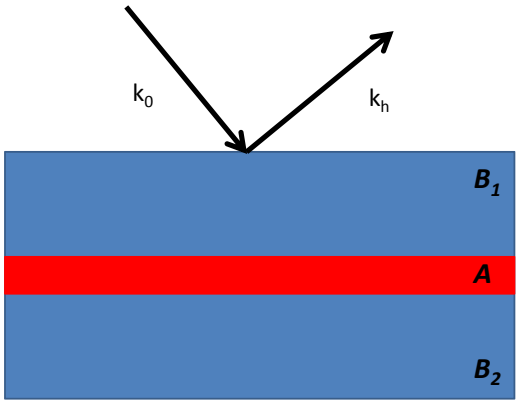

Figure 2.16: *Schematic representation of a thin buried layer A sandwiched between two thick layers B.*

This situation can be described easily by kinematical theory: an exhaustive discussion of the phenomenon can be found in reference [73], here only the final results are reported. The most important is that the difference in the reflectivity ΔR caused by the sandwiched layer A is given by the reflectivity of the cladding layers $B_1 = B_2 = \mathrm{C}$.
ΔR is modulated by two sinusoidal functions that describe the phase shift of the wave fields between the layers B_1 and B_2 separated by the thin layer A:

$$\Delta R \approx 4\Phi_C^2 \left[sin(A_A Y_A + A_C Y_C) + sin(A_A Y_A) \right] \tag{2.23}$$

where Φ_C is the scattering power of the cladding layers, $A_i Y_i$ terms are the phase shifts due to either the thin layer A or the cladding layers C.
The first sinusoidal term depends on the total thickness T_C of the heterostructure, while the second term is a function only of the thin sandwiched layer parameters, which are the perpendicular strain $\varepsilon_\perp$ and its thickness t.
The phase shift between the wave fields is related to a quantity called I_{strain}, defined in this case as the product of the perpendicular strain $\varepsilon_\perp$ of the sandwiched layer and its thickness t. Then

the modulation of the reflectivity increases increasing the layer thickness and/or increasing the strain. As a result of this treatment, a link between the fringe pattern and the strain integral, I_{strain}, has been found: while the period of the oscillations is related to the thickness of the layer B_1, the amplitude of the fringes is related to I_{strain} and thus to the layer thickness t.
This statement can be understood easily examining the example in figure 2.17(a) and (b), where the cap layer (a) and the sandwiched layer (b) thicknesses have been varied.

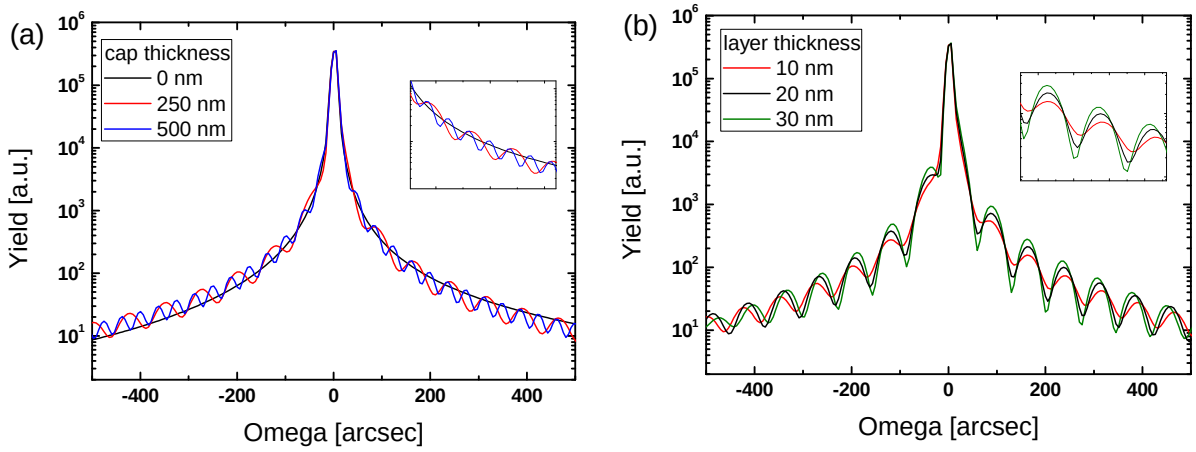

Figure 2.17: *Simulated x-ray diffraction patterns around the (004) Ge reflection for a $Ge_{0.999}B_{0.001}/Ge$ layer sandwiched between two thick Ge layers. (a) Influence of the uppermost layer thickness on the diffraction pattern; (b) influence of the thin buried layer thickness with 250 nm thick uppermost layer.*

2.6.4 Hot stage apparatus and experimental strategy

The HRXRD spectra are usually collected at room temperature. But by heating the sample and then performing rocking curve measurements as a function of the annealing temperature, it is possible to get access at other useful information.
Thanks to the presence in our diffractometer of an hot stage apparatus (figure 2.18) it has been possible to perform a temperature dependent X-ray study during the annealing itself. The rapidity in the acquisition of each rocking curve is fundamental, but the presence in our apparatus of a parabolic mirror ensures a high intensity, then a fast measurement collection. The annealing apparatus is made of a heating plate, which is mounted in place of the normal sample holder plate, where the sample is fixed by clips. Then the sample is covered by a plastic dome, with the peculiarity to be almost transparent to X-ray (the beam intensity is reduced by a factor $\sim 30\%$). Thanks to the presence of the dome it is possible to anneal the sample in N_2 inert gas. During the annealing up to 900 °C the dome is cooled by compressed air.
The temperature is controlled by a NiCr-Ni thermocouple, but additionally it has been checked by comparing the substrate lattice parameter dilatation with literature values, founding a very

good agreement between the nominal and the experimental hot stage temperature ($\pm 3 \div 4\,^{\circ}$C).

Figure 2.18: *Hot Stage.*

The experimental strategy consists in the rocking curve collection during annealing in two different ways:

1. *during isochronal annealing*, i.e. the temperature is raised at regular time interval step; the time interval is that necessary for the sample thermalization, the Bragg alignment and then the $(\omega - 2\theta)$ scan;

2. *during isothermal annealing*, i.e. maintaining the sample at constant temperature a rocking curve is collected at regular time interval step.

From the isochronal annealings we are able to follow the trend of the perpendicular lattice parameter as a function of the annealing temperature (in figure 2.19 the result of the application of the procedure to a deuterated GaAs/$GaAs_{0.986}N_{0.014}$/GaAs sample is reported). In this type of plot it can be individuated changes in the slope during the annealings: every change in the variation rate corresponds to the activation of a process, as it can be the dissolution of different types of defects/clusters of defects, or defects complexes reorganization (e.g. Ostwald ripening). Indeed defects complexes formation/dissolution can take place only after overcoming an energy barrier, energy supplied by the annealing.

These results are more evident in a plot of the derivative of $a_{\perp}$(T) with respect to temperature. In this sort of "strain evolution speed" plot, the de-convolution of the best fit curve allows to find out the temperature at which a particular process evolves at its maximum speed. In figure 2.20 an example of the "strain evolution speed" plot is drawn for the deuterated $GaAs/GaAs_{0.986}N_{0.014}/GaAs$ layer.

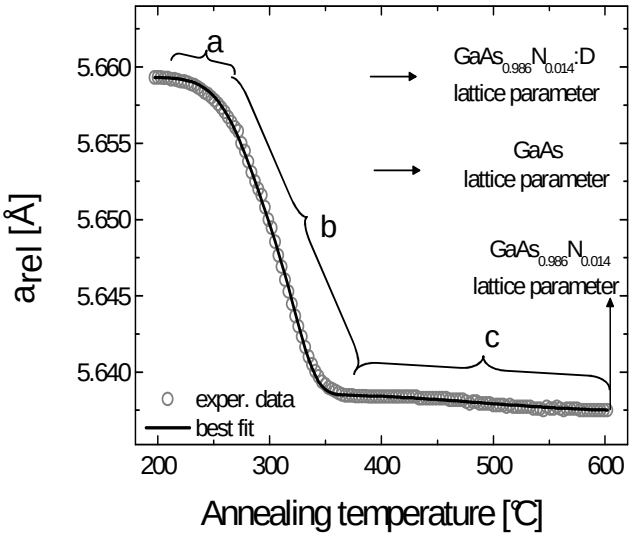

Figure 2.19: *An example of evolution of the perpendicular lattice parameter $a_\perp$ for a $GaAs_{0.986}N_{0.014}$/GaAs deuterated layer as a function of the annealing temperature (open circles), with the best-fit of the data shown as a black line. Three regimes (a, b, c) are clearly evident [76].*

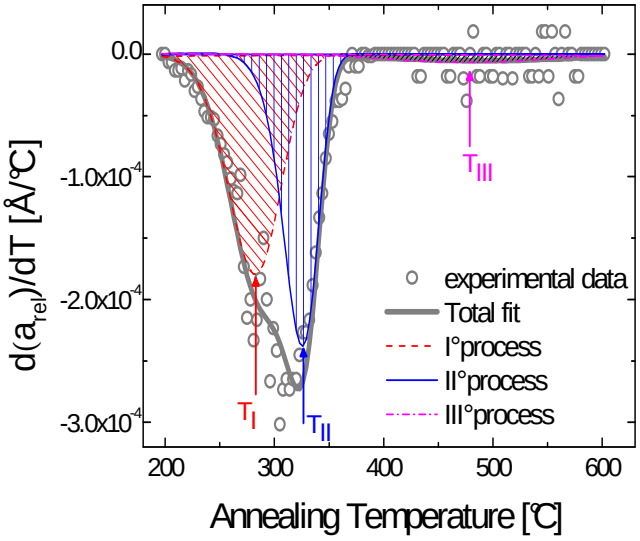

Figure 2.20: *Derivative of the perpendicular lattice parameter $a_\perp$ of the $GaAs_{0.986}N_{0.014}$/GaAs deuterated layer with respect to T. The whole-data best fit (grey continuous line) and the single contribution of each process are also displayed. Arrows mark the $(T_{peak})_i$ values at which each process gains its maximum rate [76].*

In order to characterize in detail the processes involved in the defects complexes formation/dissolution, isothermal annealings are performed, choosing temperature values for the annealings that belong to the intervals individuated by the isochronal annealings.

From these isothermal RCs the evolution of the perpendicular lattice parameter as a function of time can be found. These data can be fitted by an exponential decay curve, from which the decay rate for each dissolution step can be individuated:

$$a_{\perp}(t) = a_{\perp}(0) \cdot exp\left(-\frac{t}{\tau}\right). \tag{2.24}$$

The decay rate is related to the activation/dissolution energy by the following law:

$$\tau = \frac{1}{\nu_0} \cdot exp\left(-\frac{E_a}{k_B T}\right). \tag{2.25}$$

Drawing the logarithm of the decay time τ for each isothermal annealing against the inverse temperature, an Arrhenius plot can be built.

The experimental strategy described has to be adapted to the different sample characteristics under study: for example, a not uniform distribution of defects inside the sample could not allow to determine a unique value of the perpendicular lattice parameter for the entire strained layer. In this case it is preferable to consider the strain integral, defined as the area under the strain profile:

$$I_{strain} = \int_{t_1}^{t_2} \varepsilon_{\perp} dt \tag{2.26}$$

where t_1 and t_2 represent the double ends position of the strained region.

The strain integral can be used instead of the perpendicular lattice parameter: if the perpendicular strain profile changes its shape during the annealing, its integral undergoes to a general variation, with a rate that depends on the dissolution of different complexes.

Chapter 3

Results and Discussion

3.1 End-Of-Range defects in self-amorphized germanium: formation and evolution

As already stated in chapter 1, pre-amorphization of the substrate is an effective protocol in silicon to achieve high dopant electrical activation, and recently it has been demonstrated its effectiveness also in germanium [54], [58].
Due to the heavy consequences in the anomalous B diffusivity that this procedure demonstrated in silicon, some groups investigated on the End Of Range defects (EORds) existence in pre-amorphized germanium, using Transmission Electron Microscopy (TEM) [54], [60], [74], [75]. This technique has the undeniable advantage to give a direct image of defects inside a sample, but it could turn out to be unable to supply a definitive answer in case of small or low density defects.
For this reason High Resolution X-Ray Diffraction (HRXRD) technique has been used, since it allowed to have more sensitivity to small point defects [76], [77], and to avoid sample preparation which can induce artifacts [78].
Firstly, amorphized Ge sample has been measured, with the aim to determine whether EORds are formed immediately after amorphization or not (paragraph 3.1.1). Then the defects evolution during annealing has been studied: using the procedure described in paragraph 2.6.4 it has been possible to determine the number of step required for defects dissolution, and the activation energy for each stage. After the last annealing stage the complete epitaxial regrowth of the layer is obtained: the observation of the survival of a small fraction of EORds after complete regrowth of the crystalline structure gave the possibility to compare directly the results presented in this thesis with those obtained in reference [75] (paragraph 3.1.2).

The sample used for this study (hereafter referred to as *LNT*) is an undoped (001) Czochralski high purity Ge wafer, amorphized in a 400 kV HVEE ion implanter with 2×10^{15} Ge/cm^2 at

the energy of 300 keV, keeping the substrate at the Liquid Nitrogen Temperature. This allowed to split the damage generation from any possible damage annihilation effects due to the beam itself, while the chosen dose ensures homogenous amorphization avoiding "cellular" structure [47].

The presence in the examined sample of an amorphous layer (275 $\pm$ 15) nm thick was revealed by Rutherford Backscattering Spectrometry in channeling configuration (see section 2.4) and not by X-Ray Diffraction technique because it is blind to surface amorphous layer: the absence of an ordered structure leads only to destructive interference. This means that there are no differences in the rocking curves features coming from a bare germanium, and a Ge crystal capped with a continuous amorphous layer: the technique is sensitive only to possibly structures inducing strain in the portion of the Ge crystal.

3.1.1 Room Temperature Characterization

Firstly, a HRXRD rocking curve (RC) (an $(\omega - 2\theta)$ scan) has been collected around the (004) reciprocal lattice point of a Ge crystal and of the as-implanted sample (thereafter labeled *AI* sample). The RCs obtained are shown in figure 3.1(a)-(b).

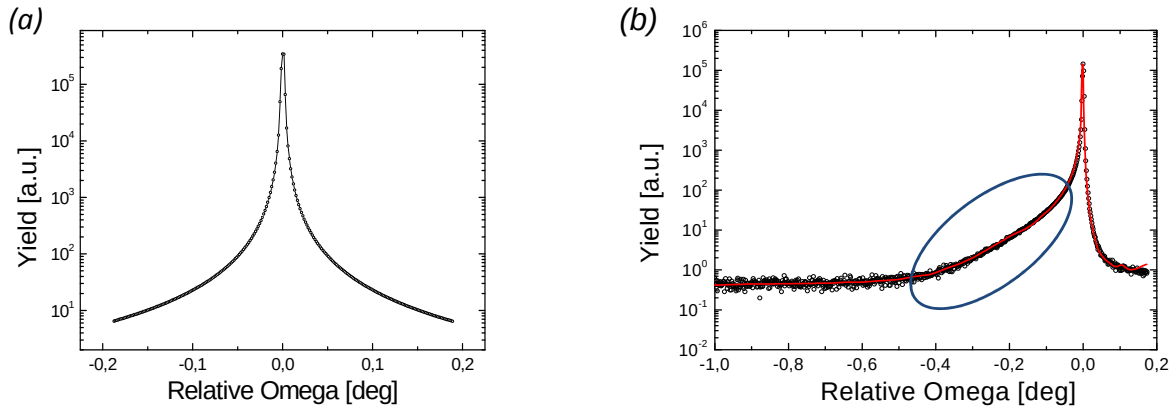

Figure 3.1: *Experimental Rocking Curve of Ge (a) before amorphization (b) after amorphization (as-implanted) with the corresponding best simulation (red line). The blue circle highlights the shoulder appearance.*

The *AI* spectrum, unlike the virgin Ge one of figure 3.1(a), is asymmetric with a shoulder visible at negative angles (the blue circle of figure 3.1(b)), which suggests the presence of positive perpendicular strain in the crystalline remaining part of the sample. Moreover any interference fringes are absent, meaning that no residual crystalline layer is left at the surface of the sample [79].

In order to clarify these indications, the spectrum has been simulated by means of RADS MERCURY code [72]: the best result obtained is drawn as a red line in figure 3.1(b).

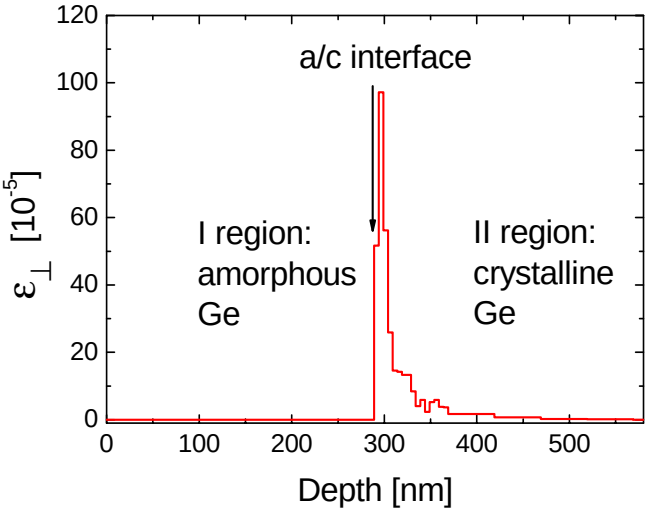

Figure 3.2: *Perpendicular strain profile of the As-Implanted sample.*

The corresponding perpendicular strain profile, drawn in figure 3.2, highlights the presence of a positive strained shallow region immediately below the amorphous/crystal interface. From the experience accumulated with silicon substrates [81] [83] [84], the position and the positive sign of the strain indicate the presence in the sample of interstitial defects, known as End of Range defects (EORds). This is the first time EORds have been revealed in self-amorphized germanium.

As already stated in paragraph 1.4, End of Range defects have a fundamental role in enhancing B diffusion (TED) in silicon substrates. TED phenomenon in Ge is only a slight tendency, and the amount of the positive strain due to EOR defects in Si is normally higher compared to that revealed in Ge. Nevertheless it is very important to understand the formation and the evolution of these defects, with the aim to discover their possible interaction with dopants, crucial information for the realization of Ge-based USJ.

The observation in Ge of a low strain amount due to EORds could justify the lack of TEM images about EORds in as-amorphized samples [54] [60] [75]: indeed, this low strain amount can be induced by small defects or a low defects density, resulting in both cases invisible by TEM (figure 3.3). Another possible reason of the lack of TEM observations could be the thickness of the amorphous regions in the samples of references [54] [60] [75]: they were shallower compared to that of the sample used in this thesis, so the surface could act as a sink for the defects even during implantation.

Only one work in literature reported on EORds observation before SPER, using TEM technique [74]. The authors revealed dot-like defects of 12 nm diameter, but in that case a high energy (1

MeV) silicon beam has been used to amorphize the Ge substrate, and it is probably due to the different conditions created by this high energy implant that some EORds were revealed.

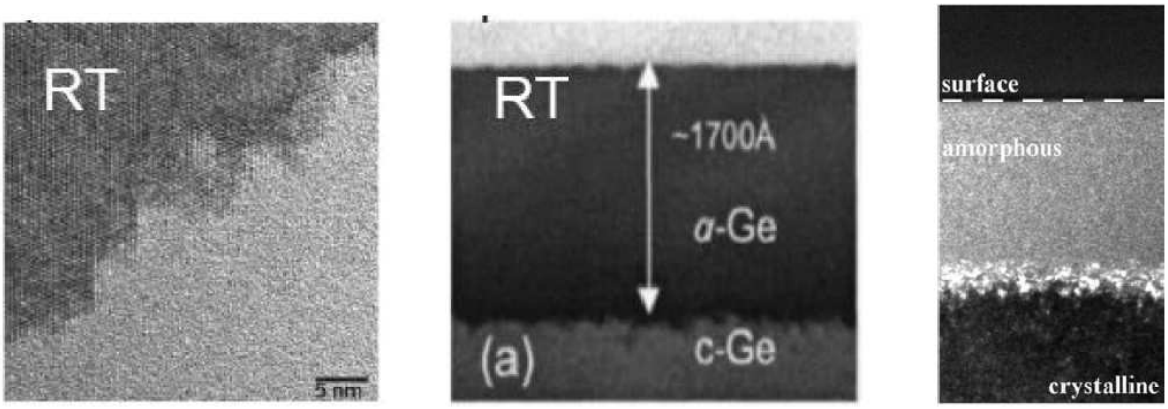

Figure 3.3: *TEM images of germanium amorphized with (a) 100 keV energy Ge ions to a dose of* 1×10^{15} *ions/cm*^{2} *at room temperature [54]; (b) 45 keV energy Ge to a dose of 1* $\times10^{15}$ *ions/cm*^{2} *at room temperature [60]; (c) 150 keV energy Ge ions at a dose of 5* $\times10^{14}$ *ions/cm*^{2} *at a temperature of 270 K [75].*

In summary, for the first time the presence of EORds in self-amorphized germanium has been revealed just before implantation with a beam energy lower than 1 MeV, identifying their interstitial nature and their strain profile.
At this point it was noteworthy to elucidate what happened to EORds during thermal annealing, and to determine whether the thermal budget needed for the complete SPE regrowth of the amorphous layer was enough also to completely dissolve these defects.

3.1.2 High Temperature Characterization

Following the procedure described in paragraph 2.6.4, a first set of isochronal annealings have been performed, each lasting 8 minutes and, after each measurement, rising the temperature of 3 °C. The temperature range spans from 25 ° to 340 °C. For every temperature step, before collecting a new RC, the alignment of the sample was checked, to make sure that Bragg diffraction conditions were preserved.
Unfortunately, this procedure allowed to acquire rocking curves quickly, but with low statistics. Moreover the low intensity of the main feature observed in the RCs - the shoulder at negative angles - and the statistical noise didn't allow for a very accurate strain determination.
But in the rocking curves of figure 3.4(a) is clearly visible that the annealing at increasing temperatures gave rise to a reduction of the shoulder connected to the EOR defects presence. Thus it was possible to individuate a quantity Q proportional to the area under the RC shoulder, and thus to the EORds strain (the dashed region in figure 3.4(a)), and to plot Q as a function of the

annealing temperature (figure 3.4(b)). From this plot information about EORds dissolution can be derived.

Figure 3.4(b) shows that the RCs shoulder, and the related strain, started to change at T $\sim$ 75 $^{\circ}$C, and after that temperature five thermal regions were singled out, indicate in figure with roman numbers. In particular, a considerable changing of Q took place only in the regions labeled as II and IV, while in the other regions Q seemed quite stable.

This important observation allowed to limit the temperature range of the EORds evolution.

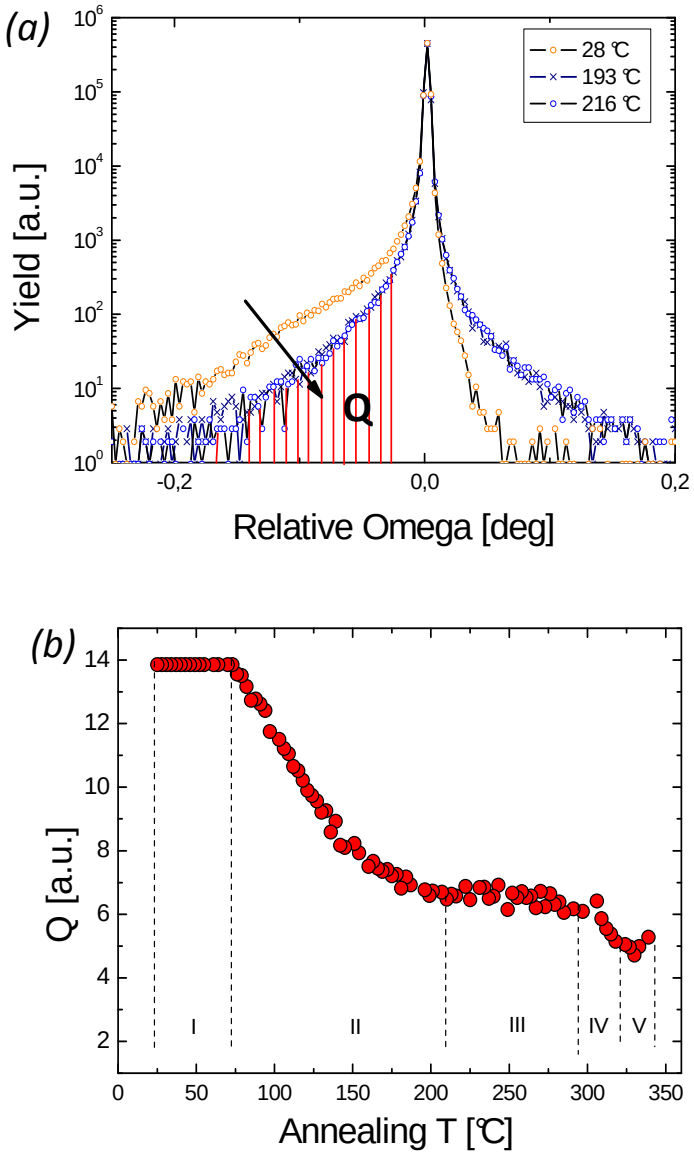

Figure 3.4: *(a) Some rocking curves collected at different annealing temperatures, where the area Q is dashed: Q lowers its value arising T, as indicated by the arrow; (b) Q as a function of the annealing temperature and the five thermal regions singled out.*

A this point series of isothermal annealings have been performed, choosing some temperatures into the thermal intervals II and IV (T equals to 90 °C, 150 °C and 180 °C for the region II and T equals to 320°C for the region IV). During the isothermal processes it was possible to collect rocking curves with high statistics, allowing to determine the strain profile and the integral strain I_{strain} (equation 2.26). Thus the I_{strain} evolution as a function of the annealing time was derived.

In figure 3.5(a) the RC from the *AI* sample before annealing (black line) is compared with the RC acquired after 5.49 h (red line), 17.44 h (green line), 45.11 h (magenta line) and 92.83 h (grey line) annealing at T= 90 °C. After ∼93 hours the spectrum did not change any more, meaning that this defects dissolution stage was saturated.

The corresponding I_{strain} values for each annealing time interval, normalized to the *AI* sample value, are plotted in figure 3.5(b).

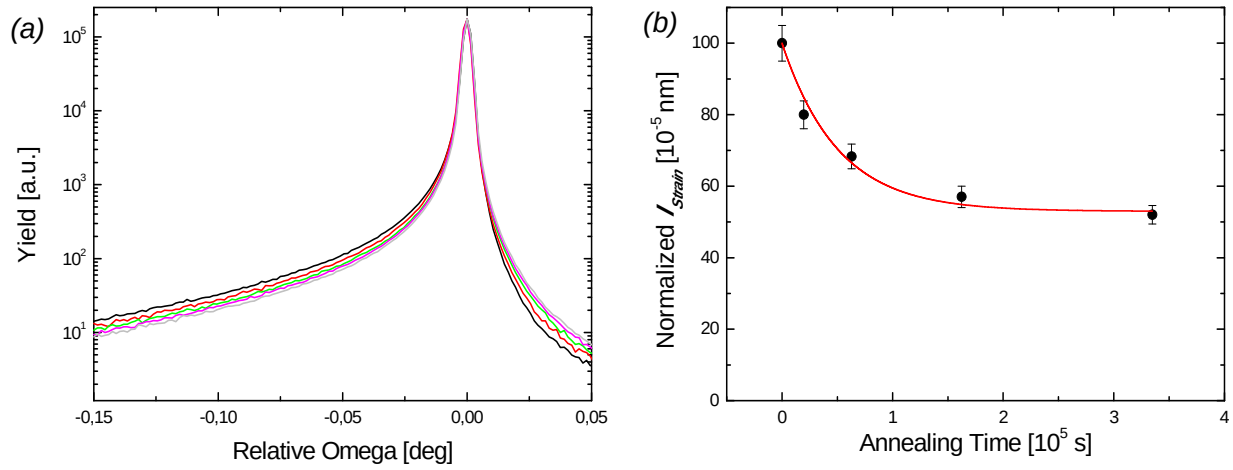

Figure 3.5: *(a) RCs collected before annealing (black line), and after isothermal annealings at T = 90 °C (after 5.49 h (red line), 17.44 h (green line), 45.11 h (magenta line), 92.83 h (grey line)); (b) I_{strain} normalized to the AI sample I_{strain} value as a function of the annealing time for T = 90 °C. The continuous line is the best fit expressed by the function 3.1.*

These values have been fitted by the following exponential decay curve:

$$I_{strain} = c \cdot exp(\frac{-t}{\tau}) + I_0 \tag{3.1}$$

where t is the annealing time, τ_1 the constant decay rate, I_0 the saturation value and c the amount of the strain lowering during the annealing. After annealing at T = 90 °C the original I_{strain} saturates about to a half of its starting value.

The other three isothermal annealings determined other three single exponential processes that

lower I_{strain} to 30% (at T = 150 °C), to 13% (at T = 180 °C) and at 2% (at T = 320 °C) of the starting value (figure 3.6).

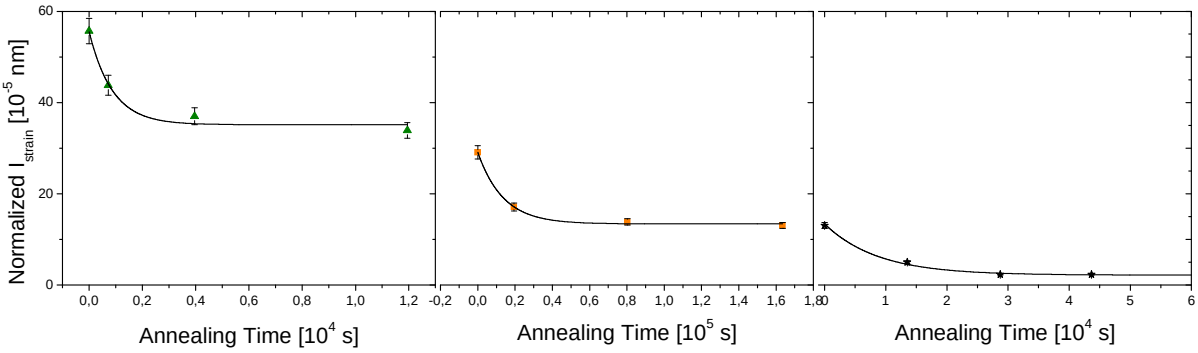

Figure 3.6: *I_{strain} normalized to the AI sample value, as a function of the annealing time for three isothermal processes: 150 °C, 180 °C and 320 °C (triangles, squares and diamonds, respectively). The continuous lines are the data best fits.*

The observation that in every isothermal process I_{strain} saturated to a well determine value implied that three different dissolution steps in the thermal region II and one in the region IV have been distinguished. Moreover the good agreement between the I_{strain} saturation value and the starting one for two consecutive steps indicated the absence of further steps in between.
In order to extract the activation energies E_a and the pre-factors ν for every dissolution step, it was necessary to perform other isothermal annealings for each step. In figure 3.7 the I_{strain} values obtained for these further isothermal processes are plotted in a semi-logarithmic way cause of the different time span in each process. Each set of data corresponding to a certain annealing temperature has been fitted by the single exponential equation 3.1, except for the data at T =120 °C and T =135 °C for which a double exponential decay curve was necessary:

$$I_{strain} = c \cdot exp(\frac{-t}{\tau_1}) + d \cdot exp(\frac{-t}{\tau_2}) + I_0 \tag{3.2}$$

where t is the annealing time, τ_1 and τ_2 the decay rates for two single exponential laws, I_0 the saturation value and c and d the amount of the strain lowering during the annealing.
This double exponential decay curve means that the temperature T= 120 °C was enough to turn on two defects dissolution steps: the first process run out in a range of few tens of degrees, then immediately after it the second process, observed also at T= 150 °C, was switched on. The same explanation holds also for the T= 135 °C isothermal process. This is a further verification that no other steps were present in between the individuated dissolution stages.

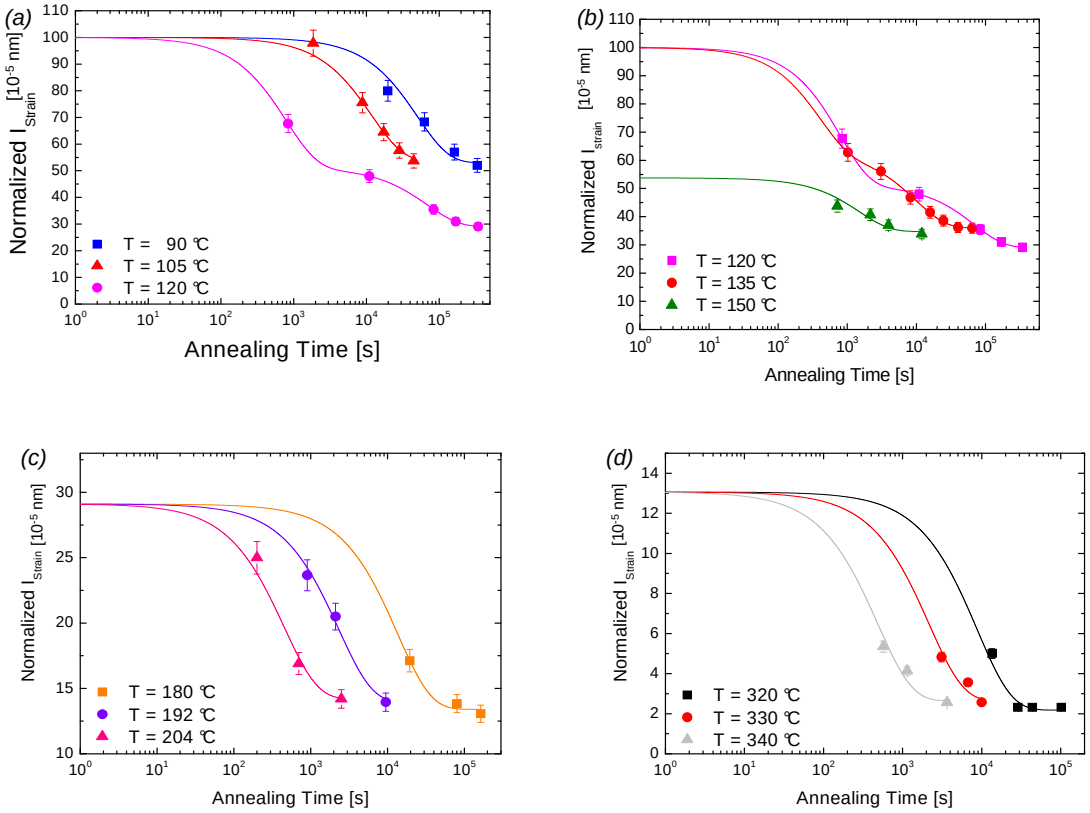

Figure 3.7: *I_{strain} normalized to the AI sample value as a function of the annealing time.The continuous lines are the data best fits. Note the logarithmic scale on the x-axis.*

At this point the decay time τ gained by each isothermal annealing set of data could be plotted in an Arrhenius way, i.e. as a function of the reciprocal of k_BT (figure 3.8):

$$\frac{1}{\tau} = \nu \cdot exp(\frac{-E_a}{k_BT}) \tag{3.3}$$

where k_B is the Boltzmann constant and T the annealing temperature (in Kelvin).
By fitting each data set, the activation energies E_a and the pre-factors ν is got for all the EORds dissolution steps. The values obtained, reported on table 3.1, support the existence of four types of EORds, well characterized by an activation energy and a pre-factor.

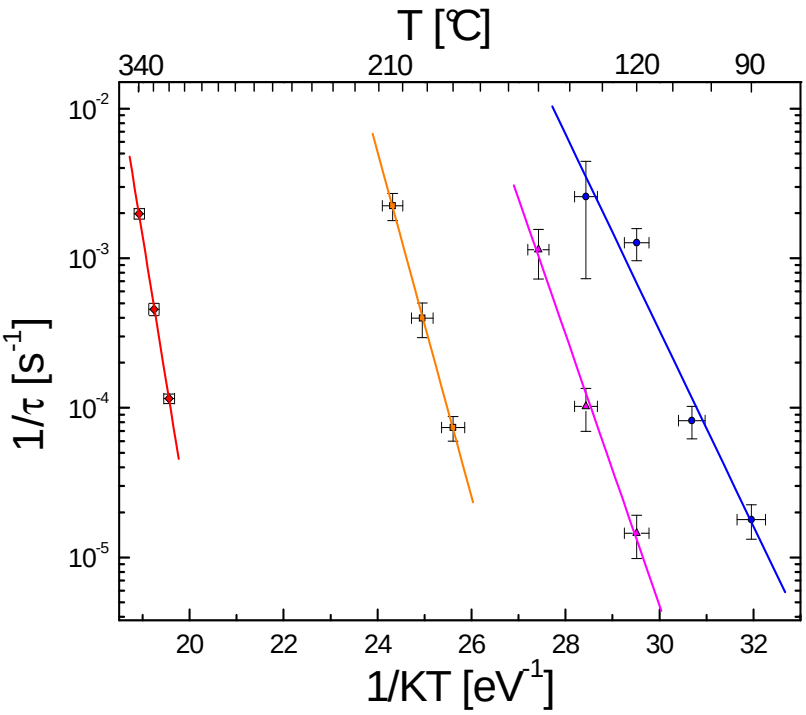

Figure 3.8: *Arrhenius plots of the four EORds dissolution steps. The continuous line are the best fits obtained from equation 3.3.*

Process	**Temperature (°C)**	E_a **(eV)**	ν **(Hz)**	I_0 **(%)**
1	90 105 120* 135*	1.51 ± 0.21	$10^{16\pm3}$	53.0 ± 2.4
2	120* 135* 150	2.08 ± 0.17	$10^{22\pm2}$	35.2 ± 1.3
3	180 192 204	2.65 ± 0.06	$10^{25\pm1}$	13.4 ± 1.5
4	320 330 340	4.46 ± 0.13	$10^{34\pm1}$	2.2 ± 0.1

Table 3.1: *Dissolution steps, with the temperatures at which they have been studied (the temperature marked with an asterisk run out two consecutive steps) and the activation energies E_a and pre-factors* ν *obtained by fitting with equation 3.3; in the last column the strain integral saturation value I_0 for each process is reported.*

An attempt to identify the objects, i.e. the defects types, involved in these dissolution steps is possible comparing the activation energy data with the ones present in literature.
Theoretical calculations about the migration energies for vacancies and interstitials are reported on table 1.2 of the first chapter. From those values it results that the activation energy for first process ((1.51 $\pm$ 0.21) eV) is more compatible with the migration energy for interstitials than that for vacancies. This suggests that the first and larger strain dissolution ($\sim$50%) could be due to the migration of interstitial defects created by the amorphization process. The hypothesis is corroborated by a pre-factor value compatible, within the error bar, with the Ge phonon frequencies, meaning that no other species are involved in the process.
Moreover, calculations of reference [25] found a formation energy for vacancies in the range (1.98 $\div$ 2.35) eV, interval that matches quite well with the activation energies of the other three steps. However, the same reference estimated that the equilibrium concentration for vacancies at temperatures corresponding to those of the isothermal annealings is very low: even for the highest annealing temperature used in this thesis the vacancies concentration does not exceed $\sim 10^7/cm^3$. The value is clearly too low to suggest an important role for these objects in the strain dissolution process. In the same way, it can be excluded a role in the dissolution also for the interstitials formation, due to the high energy required ((3.25 $\pm$ 0.25) eV).
About the activation energies and the pre-factors found for the steps II, III and IV, the values found suggest the involvement of more complex defects than simple interstitials or vacancies, and for this reason they require higher thermal budgets to dissolve, analogous to what happens in silicon.

Coming back to the isothermal processes, it's worth noting that after $\sim$4h annealing at 320 $^\circ$C the corresponding RC (figure 3.9(a)) exhibits weak symmetric interference fringes, unlike the RC acquired during annealing at lower temperatures (figure 3.5(a) for example). These fringes arose from the presence of a strained layer sandwiched between two crystalline structures so thin that acts only as a de-phaser between the bulk germanium and the re-crystallized film. This means that after this annealing the SPE of the amorphous layer has been obtained and the thin strained layer probably came from the survival of a small amount of EORds below the original amorphous/crystal interface. This was the first time that EORds were revealed in PAI germanium sample after SPE regrowth.
As explained in paragraph 2.6.2, the fringes period allowed to calculate accurately the thickness of the regrown amorphous layer, that is (289 $\pm$ 8) nm in agreement within the error bar, with the initial amorphous layer thickness determined by RBS.
It has been performed a simulation of this RC (drawn over the experimental data in figure 3.9(a)): the corresponding perpendicular strain profile is reported in figure 3.9(b). The comparison between this profile with that obtained from the *AI* sample spectrum (figure 3.1(b)) showed that $\sim$98% of the strain (i.e. EOR defects) dissolved during SPER, but a detectable

part was still present. These data mean that the energy supplied to the system to regrow the amorphous layer was not enough for a complete EOR defects annealing.

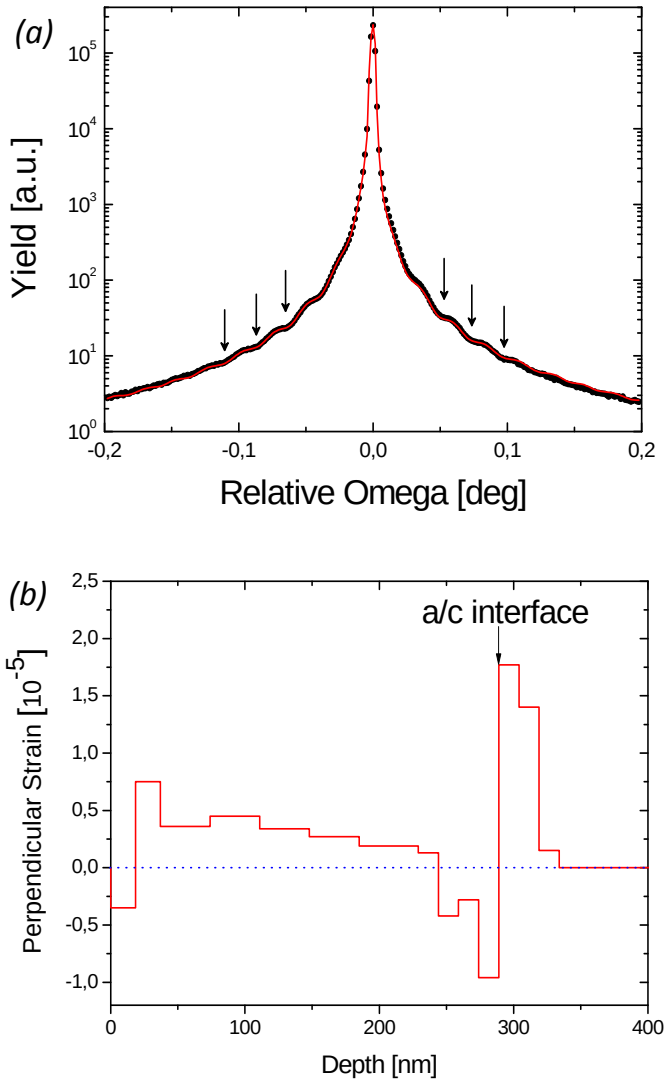

Figure 3.9: *(a) Rocking Curve collected from self-amorphized sample and regrown at 320 °C: the continuous red line over the data is the best fit; (b) corresponding perpendicular strain profile.*

In order to induce the complete dissolution of the residual defects, higher temperature annealings have been performed. The temperature has been linearly raised, as previously described, until the complete disappearance of the fringes pattern.
The fringes at T= 395 °C (open circles of figure 3.10(a)) became weaker, but it was necessary to wait 4.5h at T= 405 °C for the fringes disappearing, as it can be noticed in the corresponding RC (stars of figure 3.10(a)). In figure 3.10(b), the strain profiles related to the best fits of the RCs of figure 3.10(a) showed different features in comparison with the ones obtained before SPER. Associated to the EORds disappearance, a negatively strained layer appeared at

the sample surface. This feature resembled what observed in silicon: indeed, Montecarlo simulations [82] and HRXRD studies [83], demonstrated that Si regrowth leaves a surface layer rich of vacancy clusters which cause negative strain, i.e. lattice contraction. But it is worth noting that the extent of the tensile strain measured after SPER in silicon has almost the same order of magnitude as the compressive strain measured after amorphization. Instead in germanium, the modulus of the negative strain is two order of magnitude lower than the positive strain due to EORds after amorphization. This last observation falls with a more general picture where the germanium behavior only resembles that of silicon, and the thermal budget necessary for SPER and, most importantly, for the strain dissolution is lower in germanium than in silicon.

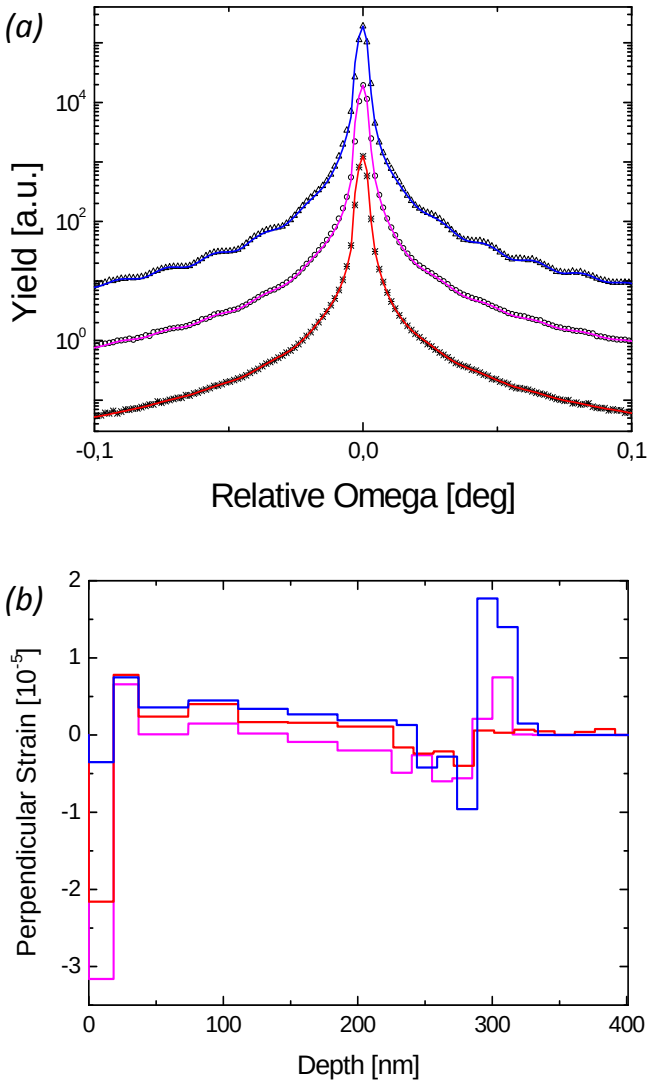

Figure 3.10: *(a) Rocking Curves collected at T = 320 °, 395 ° and 405 °C (triangles, circles and stars, respectively). The continuous lines are the best simulations. The Rocking Curves were offset for clarity; (b) perpendicular strain profiles related to the diffraction spectra of panel (a): blue line T = 320 °C, magenta line T = 395 °C, red line T = 405 °C.*

Now the results can be compared with those described in literature for the EORds existence after SPER. References [54] and [60] didn't report any evidences of EORds existence after SPER using TEM. These results are in good agreement with our results: indeed both groups performed the amorphous layer regrowth at T $\geq$ 400 °C, almost the same temperature at which it has been found the complete dissolution of the strain induced by the defects.
Only recently, Koffel and co-workers [75] have been able to reveal the presence of EORds using a sample amorphized at medium energy (150 keV) and performing a SPE regrowth at a lower temperature (T = 330 °C). However, as already stated, they didn't observe EORds immediately after implantation: probably it was essential to perform the sample annealing in order to promote defects growth in size and thus being able to reveal the defects by TEM. This confirms our hypothesis of dot-like defects formation by implantation, too much small to be revealed by TEM technique.

Performing annealings at T = 550 °C for progressively longer time intervals (Δt equal to 10 s, 30 s and 60 s), Koffel and co-workers showed defects increasing in size from 1-2 nm to 4-5 nm while decreasing in density, in a sort of Ostwald ripening growth mechanism, similar to what is observed in Si.
However in ref. [75] these last results have been observed in samples amorphized with P^+-implantation at the energy of 15 keV, instead of Ge-implantation at 150 keV, because the defects were formed much closer to the surface and this favored their observation under WBDF-TEM conditions. The use of dopants instead of Ge ions in the amorphization procedure could have given rise to a sort of stabilization of the EOR defects and then a higher difficulty to dissolve them, explaining thus the EORds survival at temperature higher than those reported in this thesis.

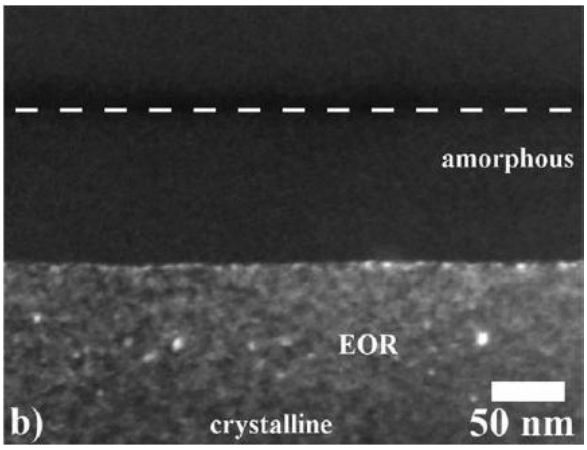

Figure 3.11: *WBDF-XTEM images of a 150 keV Ge^+ 5 $\times$ 10^{14} ions/cm^2 implanted Ge layer after subsequent annealing at 330 °C for 1325 s. The broken line follows the surface of the wafer [75].*

In summary, thanks to HRXRD technique the existence of EORds in self-amorphized Ge has been revealed even after annealing necessary for the SPE regrowth. Moreover, exploiting the Anton Paar apparatus, it has been determined in detail the dissolution kinetics of these defects, discovering the existence of four different types: the first one involving self-interstitials migration, the other three consisting in more complex defects than simple interstitials or vacancies, in agreement with data present in literature and TEM images.

The study performed on the damage recovering after amorphizing implants, highlights the deep differences between Si and Ge: the strain amount due to EORds is lower in germanium than in silicon, and probably this is explainable with the formation of defects with lower size and/or lower density; while germanium required a temperature of about 400 °C for the complete damage recovery, damage disappearance in silicon requires higher temperatures, close to (800-1000) °C [86]; after complete dissolution of the residual defects, at the surface of both the materials a negative strain region is formed, but also in this case the strain amount is higher in silicon than in germanium. The picture drawn is that of a germanium substrate easier to damage with ion implantation, but also easier to recover completely in the cristalline structure, without heavy consequences at the surface.

In order to complete the comparison between silicon and germanium about the defects formation after implantation, it has been studied defects and damage recovering mechanisms in germanium after sub-amorphizing implants. The results are described in the next paragraph.

3.2 HRXRD study of defects in Ge sub-amorphizing implants

The mechanism of defects formation and evolution after non-amorphizing implantations have been studied both at room temperature and after annealing. Annealing induces defects dissolution, and the released interstitial flux can interact with B dopant which, as already explained in chapter 1, diffuses through interstitials. Thus growing samples with B spikes, it was possible also to monitor the presence and the behaviour of the interstitial flux and its interaction with boron.

Using the Molecular Beam Epitaxy (MBE) technique, it has been grown samples containing five B delta layers placed at 100, 300, 500, 700 and 1000 nm under the surface, with a concentration of $4 \times 10^{18} B/cm^3$ and implanted at room temperature with 840 keV energy Ge beam at three different fluences: 2×10^{11}, 1.5×10^{12} and 1×10^{13} Ge/cm^2. The energy chosen for the implant ensured that the projected range R_p of Ge ions was located between the second and the third delta: in this way the surface was sufficiently far not to act as a sink for the interstitials during the defects dissolution process, moreover it allowed the possibility to check the intestitials movement inside the sample towards the deeper delta layers. To make easier the identification of the samples, they have been labeled with the abbreviations *LD*, *MD*, *HD* respectively. The structure of the samples is drawn in figure 3.12.

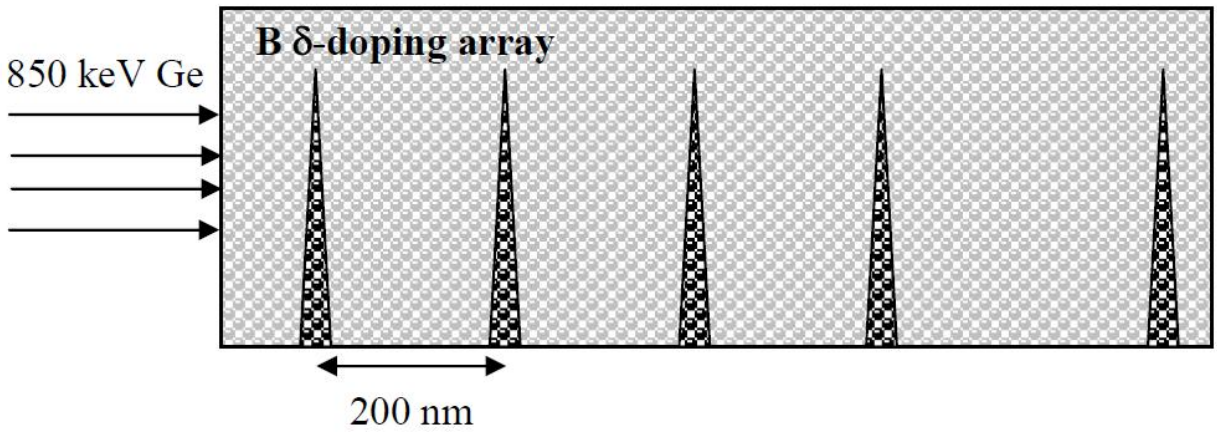

Figure 3.12: *Scheme of the sub-amorphized samples structure.*

3.2.1 Room Temperature Characterization

Performing an $(\omega - 2\theta)$ scan around the (004) reciprocal lattice point in each samples, it appeared immediately that the sample implanted with the lowest fluence (the open squares in figure 3.13(a)) did not show measurable strain. Instead, the *MD* sample RC showed a pronounced shoulder - at negative angles - on the left of the Bragg peak, and in the *HD* sample RC

a series of non-periodic fringes appeared. In figure 3.13(a) the continuous lines over the data are the best fits obtained by simulation.

The corresponding $\varepsilon_{\perp}$ profiles, reported in figure 3.13(b), displayed positive strains meaning that the implants positioned Ge ions in interstitial sites (similarly to what happened in silicon [83]), but the two implant fluences caused different damage amounts (note the different scale for the two profiles).

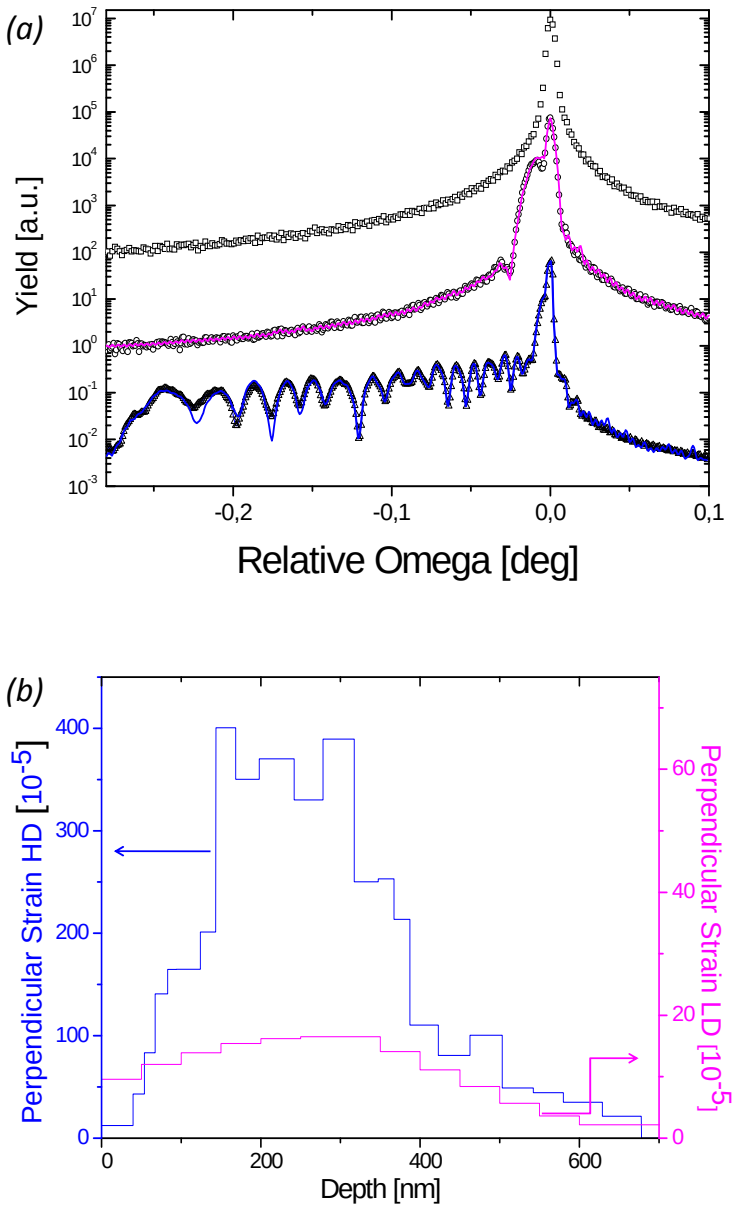

Figure 3.13: *(a) Rocking curves for corresponding to the three different implant fluences:* 2×10^{11} *Ge/cm*^{2} *(open squares),* 1.5×10^{12} *Ge/cm*^{2} *(open circles) and* 1×10^{13} *Ge/cm*^{2} *(crosses symbols); the continuous lines represent the best simulations. (b) Perpendicular strain profiles of the MD sample and HD sample.*

The data confirmed and extended the results reported in reference [47]: after an implant dose of 1×10^{13} Ge/cm^2 the authors detected a distortion respect to the Ge matrix, visible in the WBDF image collected by X-TEM as isolated white spots distributed from the surface to the corresponding projected range.

In order to check the defects stability, the *MD* and *HD* samples were measured again after five months and after twelve months. During these time intervals the samples have been kept at room temperature.

Figure 3.14(a)-(b) showed the As-Implanted RCs of figure 3.13(a) compared with those collected after five months: while in the *HD* sample profiles the same diffraction pattern appeared, in the *MD* sample profiles the compressive peak appeared reduced. This means that part of the strain, i.e. of the defects due to the implantation damage, annihilated via the so-called *ageing phenomenon*, that can be thought as an isothermal annealing at room temperature. This phenomenon clearly indicated the metastable nature of part of the defects created by the self-implantation with medium fluences (1.5×10^{12} Ge/cm^2). The lack of ageing observation in the *HD* sample means that the type and the stability of the defects formed after sub-amorphizing implantation strongly depend on the implantation fluence.

Figure 3.14(c) reported the strain profiles corresponding to the RCs of as-implanted (blue line) and after five months (magenta line) *MD* samples: the strain shape remained the same, but the strain amount lowered. The calculation of the strain integral I_{strain} associated to each profile allowed to be quantitative in the value of the strain amount lowering. The I_{strain} after five months was about 40% of its starting value and, since the HRXRD measurements were made on the same small slice of the *AI* sample, the result was not affected by a possible non homogeneity of the irradiation fluence.

This is the first experimental observation of the lattice strain ageing phenomenon in self-implanted germanium. A similar phenomenon was detected in *P*-implanted silicon [85], but not in self-implanted silicon. This observation suggested one more time that these two semiconductors are different.

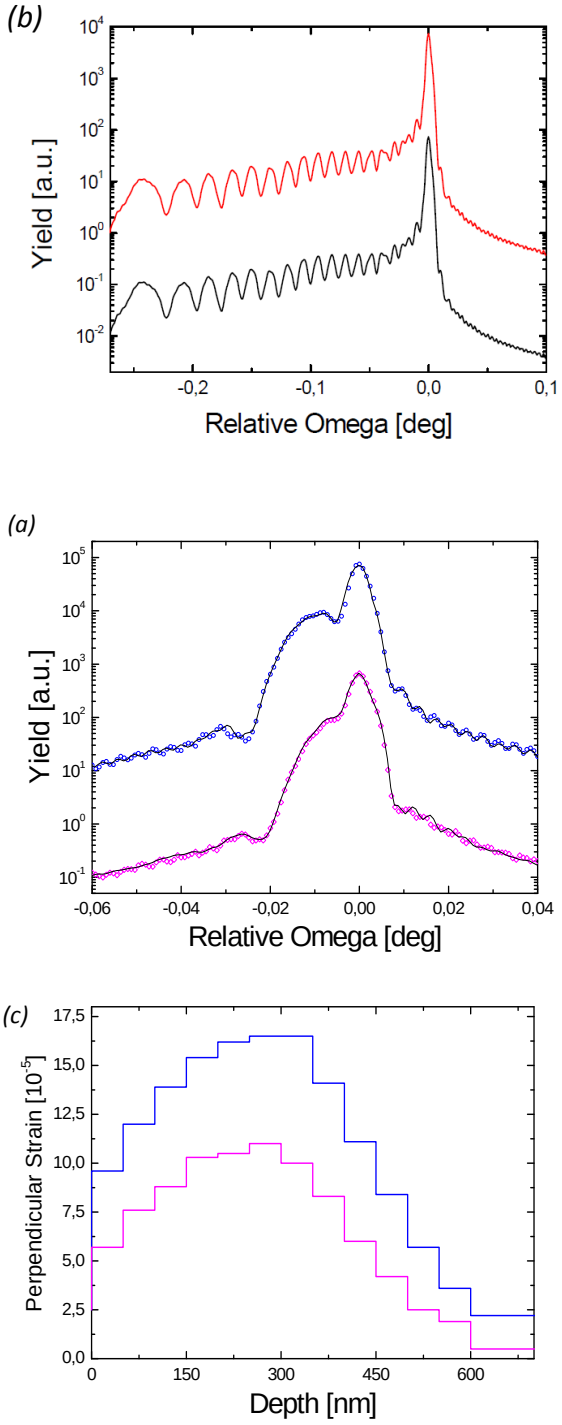

Figure 3.14: *Rocking Curves of: (a) the HD sample as-implanted (red line) and after (black line) five months; (b) the MD sample as-implanted (blue open circle) and after (magenta rhombus) five months. For the MD RC, the best simulations are drawn over the experimental data (black lines). (c) Perpendicular strain profiles of the MD sample as-implanted (blue line), and after five months (magenta line).*

The nature of the defects related to the strain ageing could be clarified putting forward some hypothesis:

- the strain ageing was caused by the dissolution of a particular type of defects created during the implantation;
- the strain integral could be considered proportional to the amount of this type of defect;
- the dissolution followed an exponential decay rate law expressed by the equation:

$$\tau = \frac{1}{\nu_0} e^{\frac{E}{k_B T}} \tag{3.4}$$

  where τ is a constant decay time, ν_0 is the attempt frequency of the process, T is the temperature, k_B is the Boltzmann constant and E the activation energy of the process.

This last hypothesis was plausible since, as reported in section 3.1.2, each step of EOR defects dissolution followed the same law. Moreover, the strain ageing could be supposed as a process not mediated by other defects species, but just activated by the energy at disposal of the system, i.e. the thermal energy: in this case, the Ge phonon frequency ($\sim$ 10 THz) could be used as attempt frequency. Replacing it in the equation 3.4 the activation energy found was about 1.2 eV, in agreement with the theoretical calculations for the migration energy of interstitial defects ($(1.0 \div 1.4)$ eV) [25]. The ageing phenomenon is thus a process where single interstitials formed during implantation dissolve.
Repeating the RCs collection after twelve months no differences have been revealed in the samples: the strain ageing, present only in the *MD* sample, was a phenomenon that run out in five months.

3.2.2 High Temperature Characterization

With the aim to determine the dissolution kinetics for both samples, during thermal annealing isochronal rocking curves were collected (figure 3.15(a)-(b)). Even if the statistics was poor, these RCs showed features that allowed for the strain profiles and the corresponding I_{strain} determination. In figure 3.16(a)-(b) I_{strain} was plotted as a function of the annealing temperature: the star in figure 3.16(a) represented the I_{strain} starting value before the ageing process, while the arrow indicated the lowering due to this phenomenon.

For both the samples I_{strain} was not a monotonic function of the temperature.
The strain dissolution took place at different temperature intervals: $(74 \div 173)$ °C for the *MD* sample, and $(75 \div 318)$ °C for the *HD* sample. This confirmed that the two fluences gave rise to different defects.

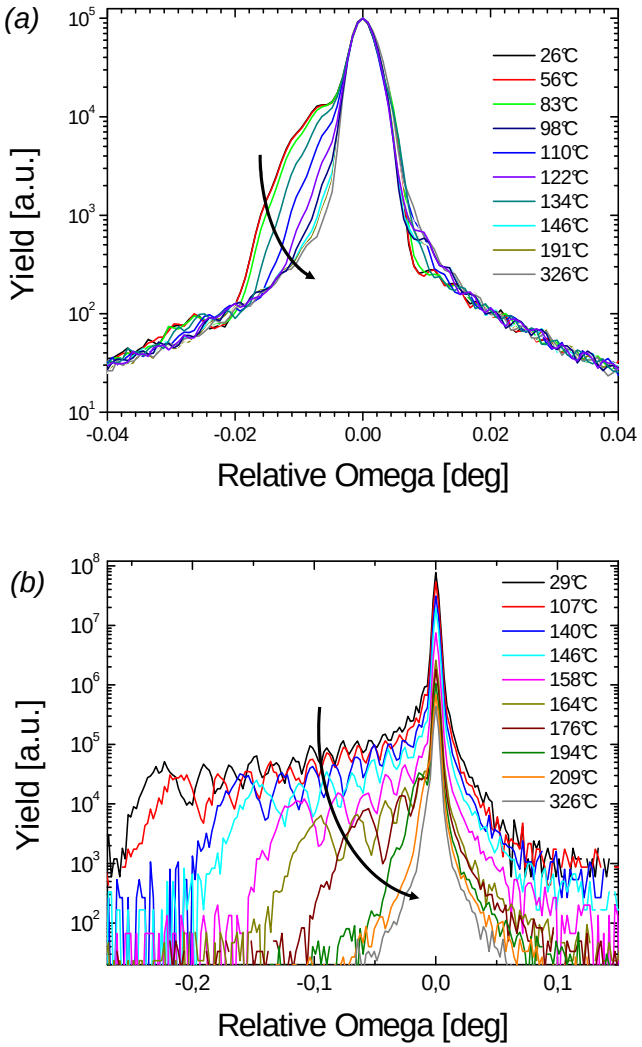

Figure 3.15: *Some Rocking Curves demonstrating the lowering of the shoulder connected with EOR defects dissolution as a function of the temperature for the (a) MD sample (b) HD sample.*

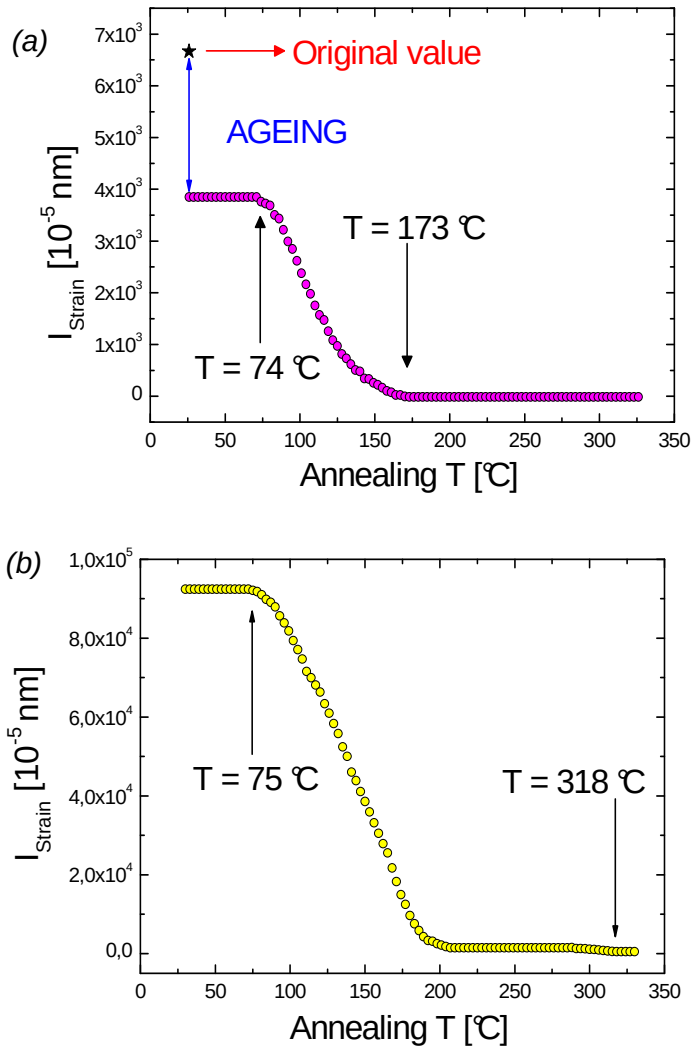

Figure 3.16: *Strain integral as a function of the annealing temperature (a) for the MD sample: the star represents the I_{strain} immediately after implantation; (b) for the HD sample.*

As in the self-amorphized sample, the defects dissolution could happen in many steps each characterized by an activation energy and a pre-factor. The effective number of steps necessary for strain dissolution could be calculated through the derivative of the I_{strain} with respect to T (figures 3.17, where a smoothing procedure of the rough data was applied). The I_{strain} derivative was then fitted (red line drawn over the data) and the fitting curve was de-convolved in order to distinguish the contribution of each process.

The plot corresponding to the *MD* sample (figure 3.17(a)) showed three maximum at T_2 = 93 °C, T_3 = 118 °C and T_4 = 157 °C. The first ageing process was also indicated with a dashed square, and took place at room temperature finishing at T < 74 °C. Also the *HD* sample plot (figure 3.17(b)) showed four maxima, but at different temperatures: T_1 = 106 °C, T_2 = 136 °C, T_3 = 169 °C and T_4 = 304 °C.

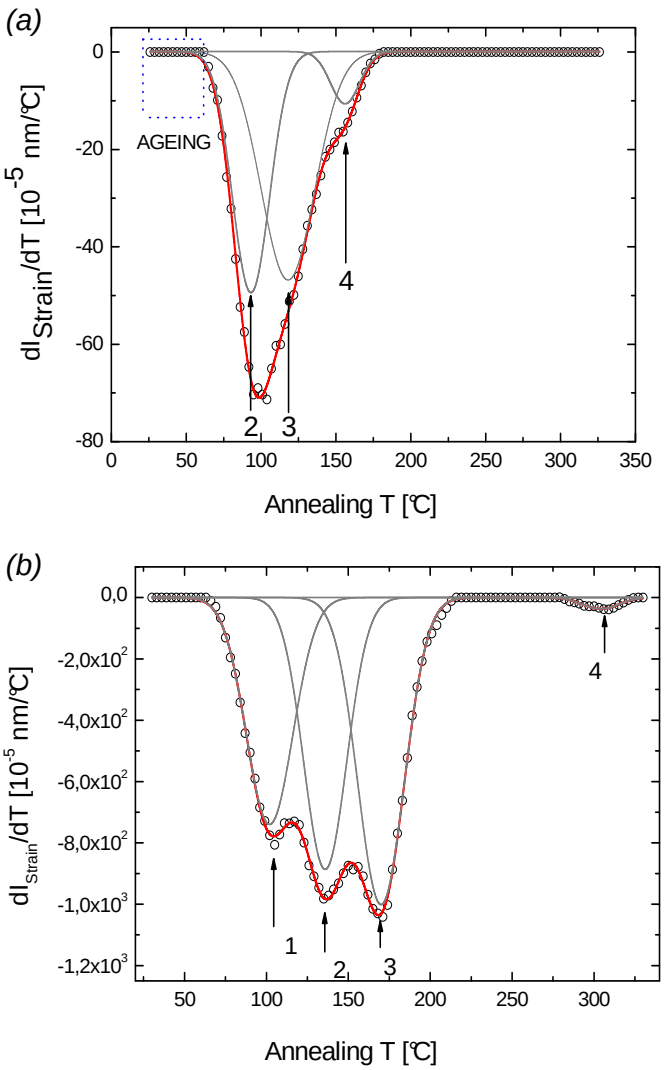

Figure 3.17: *Derivative of the strain integral with respect to the annealing temperature (open circles) for (a) MD sample and (b) HD sample. The gray lines individuate each single strain-recovery step, while the red line represents the whole data fit. The dashed square in panel (a) indicates the ageing temperature interval, while the arrows correspond to the temperature values at which the other strain-recovery steps reach their maximum speed.*

In literature some results were present for sub-amorphizing implants in germanium [80] and in silicon [85].

Hickey and co-workers [80] performed TEM analysis on bulk Ge sub-amorphized with 1 MeV Si at a dose of $1 \times 10^{14} cm^{-2}$. The authors found some defects survival after annealing up to 850 °C, during which these defects decreased in density but not in size ($\sim$12 nm). The corresponding activation energy was in the interval ($(0.1 \div 0.2)$) eV. A possible explanation for the discrepancy between the results obtained in this work of thesis and those in reference [80] can be found in the different implantation parameters: a higher implantation energy could give rise to small clusters of defects which needed a higher thermal budget to dissolve.

In silicon [85], after a sub-amorphizing implantation of $1 \times 10^{14} cm^{-2}$ Si ions at the energy of 100 keV, the recovery of the lattice damage by annealing occurred in a simpler way compared with Ge. Indeed, the strain dissolution involved only two steps: the first started at 50 °C and ended at 200 °C, corresponding to an activation energy of (1.1 ± 0.1) eV, while the second started at 500 °C exhausting at 800 °C, with an activation energy of (3.7 ± 0.1) eV.
The presence of the strain ageing (for the *MD* sample) and a damage-recovery that in both *MD* and *HD* samples took place at lower temperatures than in silicon, indicate a less stable nature of Ge defects formed after sub-amorphizing implants, compared with those formed in Si.

As already discussed in paragraph 1.3, it has been reported in literature that boron diffuses through interstitals. Since the sub-amorphizing implants and and the subsequent annealings could give rise to an interstitial flux, this could interact with boron atoms contained in the thin layers, and induce boron diffusion. These phenomena could be observed by performing SIMS measurements on the *MD* and *HD* samples containing boron delta layers.
Figures 3.18(a) and (b) concern the *MD* sample, while figures 3.18(c) and (d) concern the *HD* sample.
In figures 3.18(a) and (c) boron profiles were collected from the samples as-grown (black lines) and after Ge ions implantation plus annealing at 330 °C (red symbols). Surprisingly, both plots showed identical profiles, without B diffusion. Diffusion was expected after implantation and annealing at least in the first and the second boron deltas, since the maximum of the implant damage and then of interstitials amount was located between them. This lack could be explained by supposing a very low thermal budget or a very local nature of the implantation damage recombination, so that the interaction with B was suppressed. The absence of interstials saturation was confirmed also by SIMS measurements performed after further annealing at 840 °C for 135 minutes of the *MD* sample (figure 3.18(b)) and of the *HD* sample (figure 3.18(d)), both as-grown (blue lines) and sub-amorphized and annealed at 330 °C (magenta symbols). These plots showed only the equilibrium boron thermal diffusion, equal to that reported in literature (paragraph 1.3).

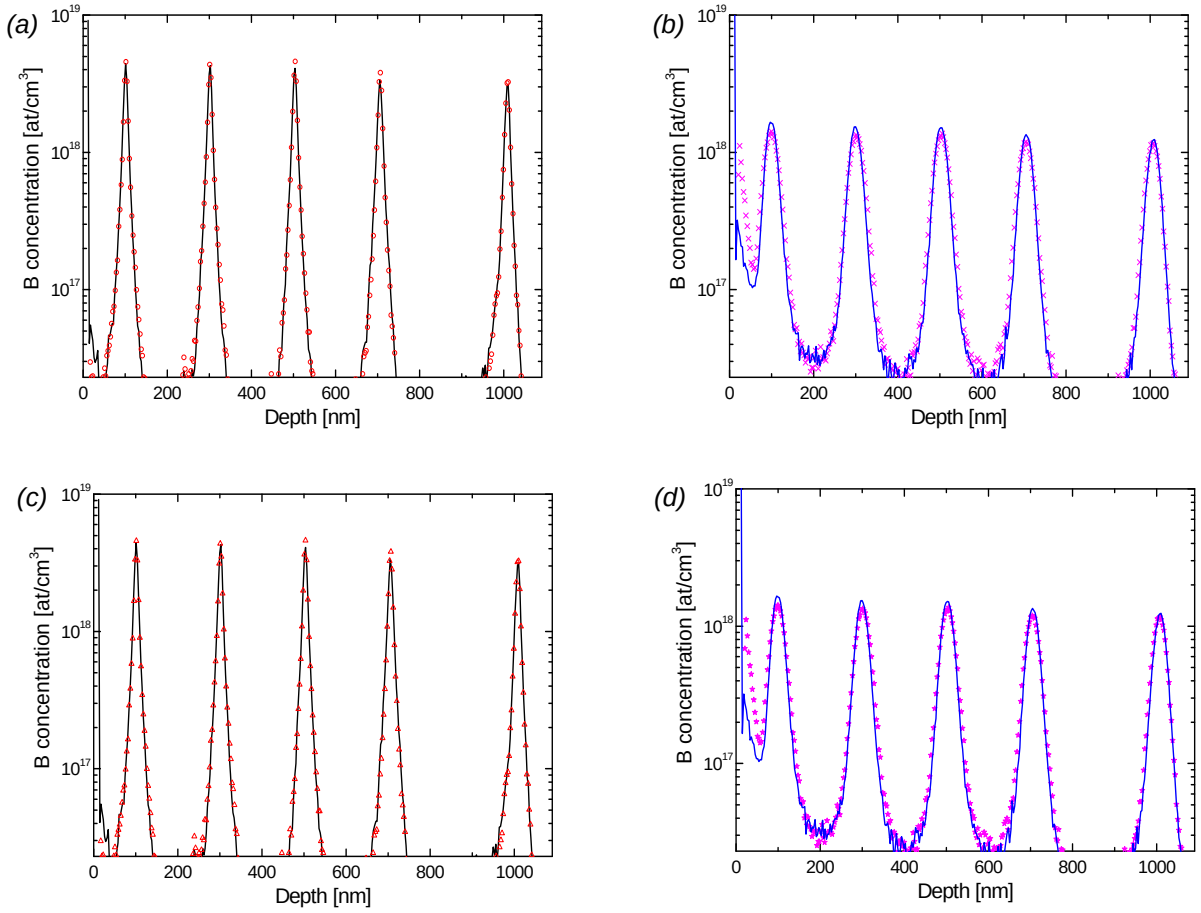

Figure 3.18: *SIMS profiles of the B delta array: (a) for the sample as-grown (black line) and after Ge implantation at Medium Dose plus annealing at 330 °C (red circles); (b) after the 840 °C thermal annealing of the sample as-grown (blue line) and after implantation plus annealing (magenta crosses); (c) for the sample as-grown (black line) and after Ge implantation at High Dose plus annealing at 330 °C (red triangles); (d) after the 840 °C thermal annealing of the sample as-grown (blue line) and after implantation plus annealing (magenta stars).*

In summary, from the study of the defects formed in germanium after amorphizing and sub-amorphizing implantations it appears clear that germanium and silicon are two different materials for many physical properties, and these must be considered when germanium is integrated in silicon technologies.

First of all germanium has a lower melting point compare to silicon (938 °C the former, 1414 °C the latter): this characteristic for itself might justify the observation that defects induced by implantations, both at amorphizing and sub-amorphizing fluences, require lower thermal budgets to anneal out in germanium with respect to silicon. Nonetheless, this issue is not sufficient. This is clear examining figure 3.19 in which the temperatures of the maximum dissolution speed for the different complexes have been plotted both for germanium and silicon -both for amorphizing and sub-amorphizing fluence regimes. Although the temperatures have been normalized to the corresponding melting temperatures of germanium and of silicon, the ranges in which the defects dissolve in germanium and in silicon are different, thus suggesting that other properties influence the defects formation/dissolution process.

For example, it is important to remember that germanium is a vacancy-rich material, and self-diffusion is dominated by mono-vacancy mechanism [1]. This means that the interstitial defects formed by implantation probably diffuse in the substrate and annihilate with the vacancies instead of aggregating, thus requiring a lower thermal budget. In silicon, where self-diffusion is interstitialcy mechanism dominated, the thermal budgets supplied by annealing allow the defects to evolve and grow in dimensions diminishing in density, following the so-called Ostwald ripening [86]: the stability of these objects is such that higher temperatures are required to dissolve.

These observations are confirmed by the HRXRD measurements, in which a lower strain amount due to the defects has been found in germanium compared with that in silicon, and explain the lack of TEM images of EOR defects in germanium self-amorphized at medium energy (lower than 1 MeV). Another support is supplied by the observation that, after the annealing which completely dissolves the positive strain due to the EORds, the amount of negative strain at the surface of the sample due to the presence of vacancies is lower in germanium than in silicon.

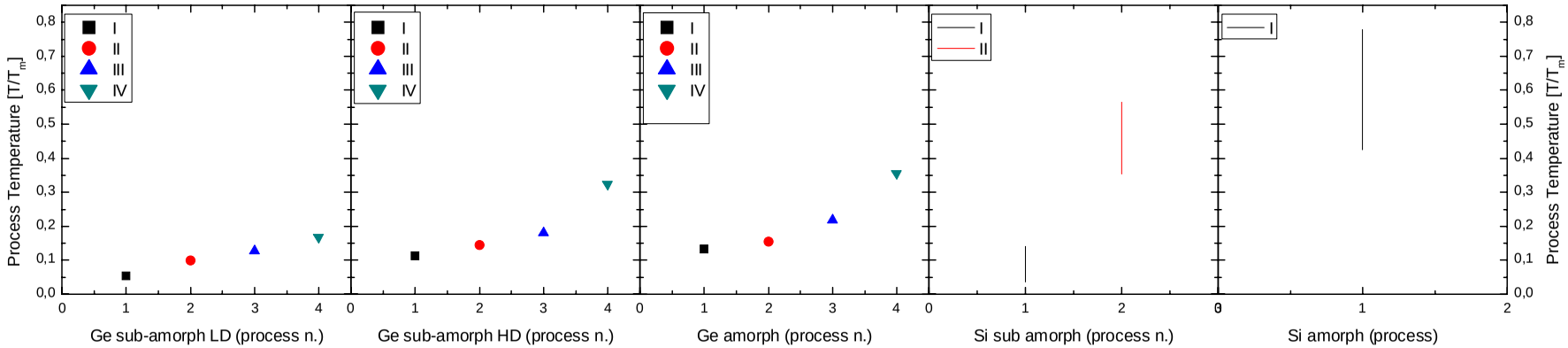

Figure 3.19: *Plot of the defect dissolution processes as a function of maximum speed temperature, normalized to Ge melting point, for germanium sub-amorphized (first and second panel), germanium amorphized (third panel). Direct comparison is made with silicon sub-amorphized [85] (fourth panel) and amorphized [86] (fifth panel) dissolution processes as a function of defect dissolution temperature range, normalized to Si melting point.*

3.3 Strain induced by boron implanted into germanium

Boron, after being the primary p-type dopant in silicon, seems a very interesting p-dopant also in germanium, especially due to its low diffusivity (see table 1.3).
In these last years it has been studied especially from an electrical point of view: the electrical B activation strongly depends on sample preparation, then lots of efforts have been spent in order to determine the best combination between ion implantation conditions and damage annealing. As in silicon, excellent results on B electrical activation have been obtained previously amorphizing Ge samples and, after dopant implantation, regrowing the amorphous layer by SPER. This method avoids dopants channeling effects and Transient Enhanced Diffusion in germanium is only a slight tendency, unlike to what happens in silicon. In the most recent study Mirabella and co-workers [58], using Ge amorphized and then implanted with 35 keV of B ions, found a maximum concentration of active B in the range $5.5 \div 5.8 \times 10^{20}$ at/cm^3 in Ge, which is 2-3 times higher than in Si.
Boron direct implantation into a crystalline Ge substrate induces the so-called "dynamic annealing", i.e. the annihilation induced by the beam itself during implantation at room temperature, a phenomenon observed also in silicon [87]. The thermal budgets supplied by the beam prevents amorphization, but at the same time it is not sufficient for the annealing out of the defects that can interact with dopant ions.
Dynamic annealing can be avoided lowering the substrate temperature up to Liquid Nitrogen temperature (LNT) during boron implantation [88]: in this way the damage is frozen and it can pile up, up to the amorphization.
Despite it could be considered a valid alternative to pre-amorphization, B implantation at LN Temperature is still lacking in a complete structural and electrical characterization. In particular, the determination of the B-induced lattice variation is completely absent, both from the experimental and theoretical point of view, even if this information can be very important.
In this work of thesis the lattice contraction due to substitutional boron was determined using High Resolution X-ray Diffraction. From this datum it is possible to deduce the amount of boron atoms placed in lattice sites and to perform a profile of boron concentration, without destroying the samples.
In this paragraph I reported the complete characterization of the samples implanted keeping the subtstrate at Liquid Nitrogen temperature, obtained using HRXRD together with Ion Beam Analyses and electrical measurements. The results were compared with those obtained from identical samples implanted at room temperature.

The samples analyzed have been obtained from Czochralski (100) crystals (Sb doped, resistivity higher than 40 Ωcm), implanted with B^+ at 35 keV at two different fluences: 2.8×10^{15} and 7.6×10^{15} B/cm^2 (corresponding maximum concentration of 2.5×10^{20} and 5.7×10^{20} B/cm^3).

The used energy led to a B projected range (R_p) of $\sim$100 nm [90].
During implantation, a specimen for each fluence was held either at Room Temperature (RT) or at Liquid Nitrogen Temperature (LNT). To make easier the identification of the samples, they were labeled with abbreviations, reported on table 3.2. Samples annealing after implantation was performed at 360 °C for 1 h in N_2 atmosphere with a proximity cap of Si to avoid Ge surface degradation.

Fluence / Substrate temperature	2.8×10^{15} B/cm^2 (low dose)	7.6×10^{15} B/cm^2 (high dose)
Room temperature ($\sim$300°C)	**RT-LD**	**RT-HD**
Liquid Nitrogen Temp. (77°C)	**LNT-LD**	**LNT-HD**

Table 3.2: *Resume of the samples in analysis, and the corresponding code.*

3.3.1 Ion Beam Analyses and electrical characterization

Firstly, the damage created on the samples by the boron implantation have been investigated by RBS in channeling configuration. Figure 3.20(a) shows the RBS spectra along the $< 100 >$ direction for the *LNT-LD* and the *RT-HD* samples after implantation, normalized to the random yield. Also virgin germanium substrate spectrum was showed for comparison.
The damage level appeared completely different between the RT implanted samples and the LNT implanted ones. In the latter samples dynamic annealing didn't occur, then an homogeneous amorphous layer was formed, with a thickness increasing with fluence: for the *LNT-LD* sample the amorphous layer extended from the surface up to depth of $\sim$185 nm, for the *LNT-HD* one it extended up to $\sim$205 nm. Also in the RT implanted samples the damage increased with B fluence, and amorphous layers were formed at the surface, but even for the *RT-HD* sample the layer thickness didn't go over the B projected range R_p (showed in figure 3.20(a) by an arrow), due to the presence of B atoms that enhanced the recombination velocity and thus the damage annealing. In other samples implanted at higher B fluences a buried damage region appeared close to R_p, which is typical feature of dilute collision cascade with a low defects density and thus a low point defects recombination [89].
After 1 h annealing at 360 °C the samples were measured again in order to find changes in the damage regions (figure 3.20(b)). The thermal budget supplied by the annealing was sufficient to regrow the amorphous layers of the samples implanted at LNT, without leaving defects, and their RBS spectra coincided with that obtained from the virgin substrate. Instead, after annealing in the RT implanted samples the damage region was reduced but not completely re-

moved. The residual damage increased with the fluence, meaning that more complex defects were formed [89]. The defects left were also very stable: further annealings at higher temperature (1 h at 450 °C and 1h at 550 °C) were not sufficient to recover the crystalline structure.

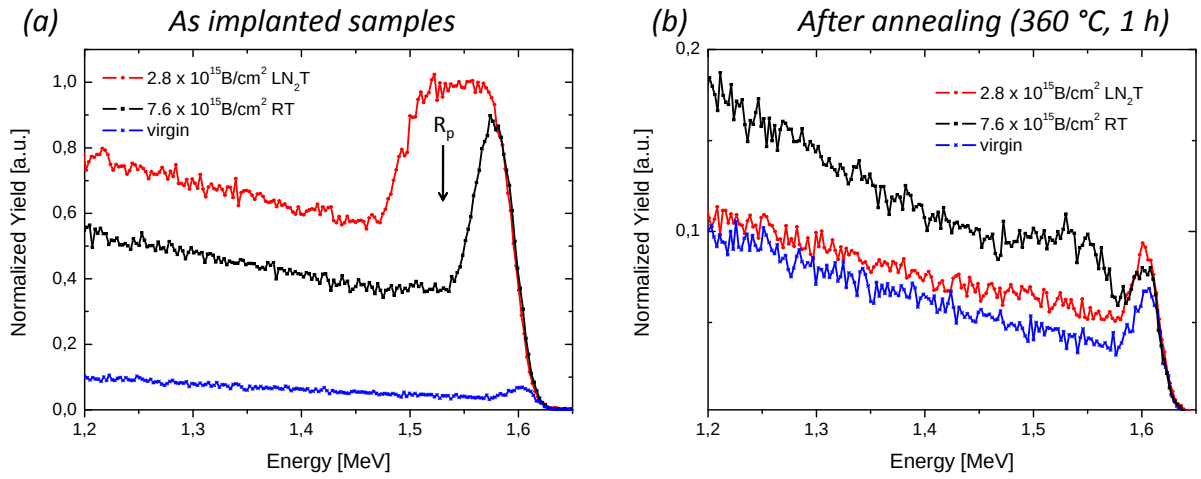

Figure 3.20: *Channeling RBS spectra for c-Ge samples implanted with B at RT (black squares) or at LN_2T (red circles) (a) as-implanted and (b) after annealing at 360 °C for 1 h. The spectrum for virgin Ge (blue asterisks) is shown for comparison [89].*

Subsequently $^{11}B(p,\alpha)^8Be$ nuclear reaction was performed to verify B fluences, while NRA in channeling configuration allowed to obtain boron substitutionality into germanium matrices on LNT implanted samples after annealing. From these measurements one deduced that about 95% in the *LNT-HD* and about 85% in the *LNT-LD* of implanted boron was positioned in substitutional lattice sites.

Nuclear reaction was used also to verify that possible B out-diffusion in the sample after higher temperature annealings (1 h at 450 °C and 1h at 550 °C) doesn't occur.

Electrical characterization allowed to reveal the damage influence on B electrical activation. B electrical activity was studied through independent determinations of sheet resistance R_S and Hall fluence N_H, from which the carrier mobility μ_H was determined. In figures 3.21 these three quantities were reported as functions of B fluences, both for LNT implanted samples and RT implanted ones. These data were compared with those reported in reference [58] for pre-amorphized (PAI) samples, processed at the same implant and annealing conditions of LNT and RT implanted samples.

Figures 3.21(a) and (c) showed that sheet resistance and Hall mobility decreased with increasing B fluence in all samples, but the values for the PAI and LNT samples were lower than those for RT samples (and coincided). In figure 3.21(b) the Hall fluence increased with implanted B fluence in all samples, but in the RT implanted ones the maximum achievable concentration

of active B was only a small percentage of the implanted fluence ($\sim$22% for the *RT-LD* and $\sim$32% for the *RT-HD*). In the LNT implanted samples almost all boron was electrically active, confirming thus the NRA data about boron substitutionality. Moreover Hall fluence in the LNT implanted samples is even better than in PAI samples.

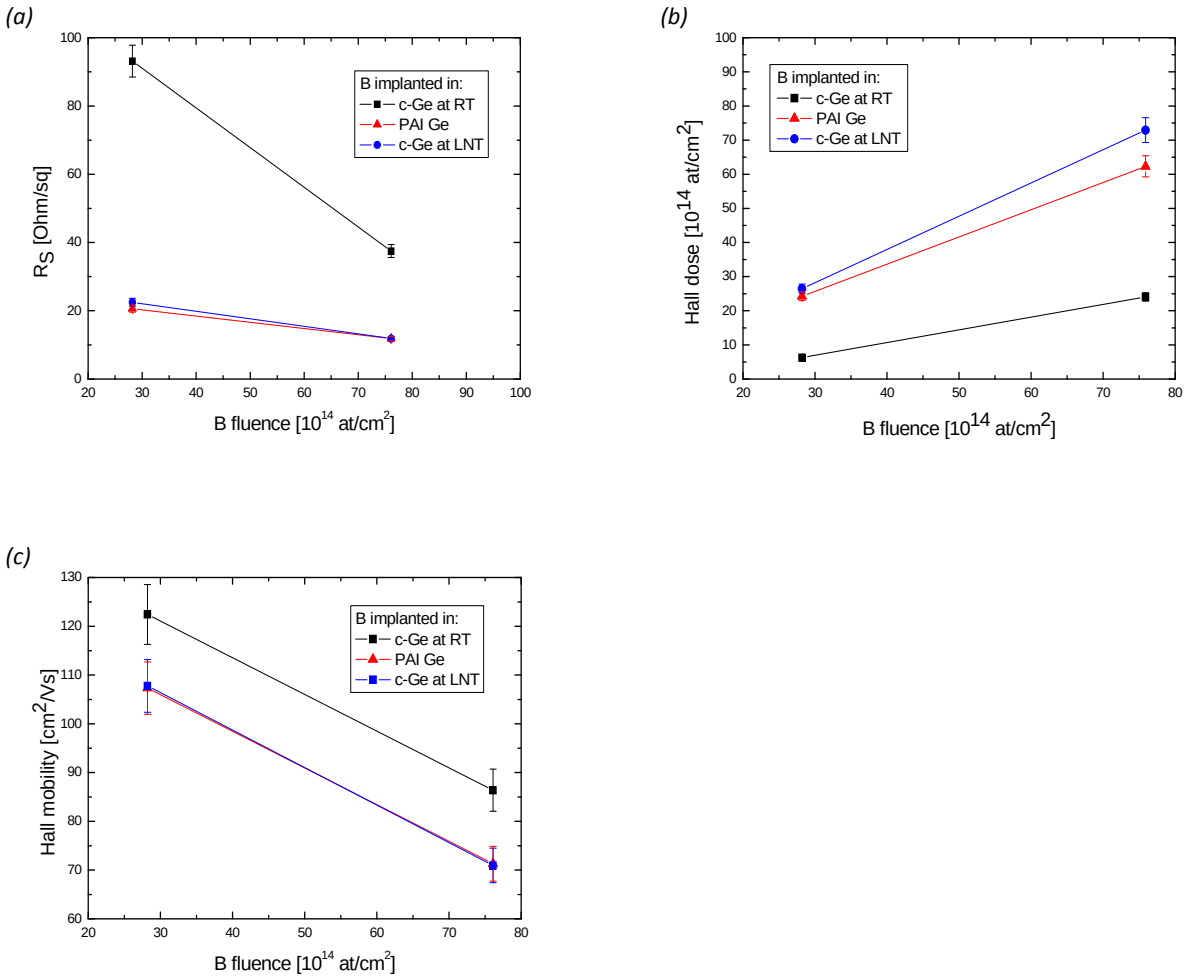

Figure 3.21: *(a) Sheet resistance R_S, (b) carrier Hall fluence N_H and (c) Hall mobility μ_H versus the B fluence for B implanted in c-Ge at RT (open circles) or at LNT (stars) or in PAI-Ge at RT (closed circles). All samples were annealed at 360 °C for 1 h [59].*

In order to verify the thermal stability of a possible B-doped Ge junction, the samples were electrically characterized after further annealings at higher temperature (1 h at 450 °C and 1h at 550 °C). Sheet resistance values in the RT and LNT implanted samples did't change, within the experimental errors.

All these data demonstrated that B-doped junctions with excellent structural characteristics and high electrical dopant activation could be obtained also with direct B implantation in crystalline substrates, if proper implant conditions were chosen: in this study it was found that implanting

with a fluence of about 3×10^{15} at/cm^2 and keeping the substrate at Liquid Nitrogen Temperature, the achievable electrical activation level could be equal or even better than in the PAI samples. For higher B implanted fluence, data showed that precipitation phenomenon occurred, limiting the maximum active B concentration level.
Moreover it was found that electrical activity of boron implanted at Room Temperature was strongly influenced by the residual damage, which was stable even after higher temperature annealing. Probably the thermal budget supplied by the annealings was sufficient to put boron atoms in substitutional sites only if these were located into amorphous pockets, while in the residual crystal defects interacted with dopant, probably forming B-Ge complexes.
The electrical activity data could be integrated with the information about the lattice strain due to substitutional boron and boron off-site. The results are showed in the next paragraph.

3.3.2 High Resolution X-Ray diffraction characterization

The Reciprocal Lattice Maps (RLMs) around the (004) and (224) reciprocal lattice points were collected for each sample (in figures 3.22 the RLMs concerning the *RT-HD* sample are reported as examples). In the symmetrical (004) map the intensity maxima corresponding to the substrate and the film RL nodes perfectly lay on the surface normal- the [001] direction (indicated with a dashed line in figure 3.22(a)), meaning that the examined sample was tilt-free. In the same way, the asymmetrical (224) map of figure 3.22(b) showed perfect alignment between substrate and the film RL nodes along [001] direction, meaning in this case that the sample was fully strained. The same results were obtained for all the samples.

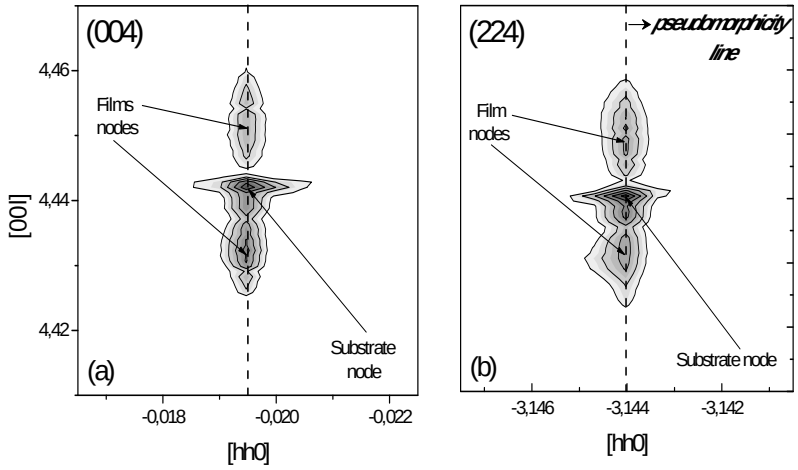

Figure 3.22: *(a) (004) RLM of the RT HD sample; (b) (224) RLM of the RT HD sample. The iso-intensity contours are drawn in the range from 3×10 to 2×10^5 counts in a logarithmic scale. Note the perfect alignment between the substrate and the films nodes in both RLMs.*

Then the $(\omega - 2\theta)$ scans around the (004) reciprocal lattice point were collected.
In figure 3.23(a) the *RT-LD* sample RC (open blue triangles) exhibited a secondary Bragg peak at negative angles, while the *RT-HD* sample RC (red stars) showed two secondary Bragg peaks, one at negative and one at positive angles.
In figure 3.23(b) completely different features appeared: both the LNT implanted samples RCs exhibited a secondary Bragg peak at positive angles (open blue circles: *LNT-LD*, red diamonds: *LNT-HD*).

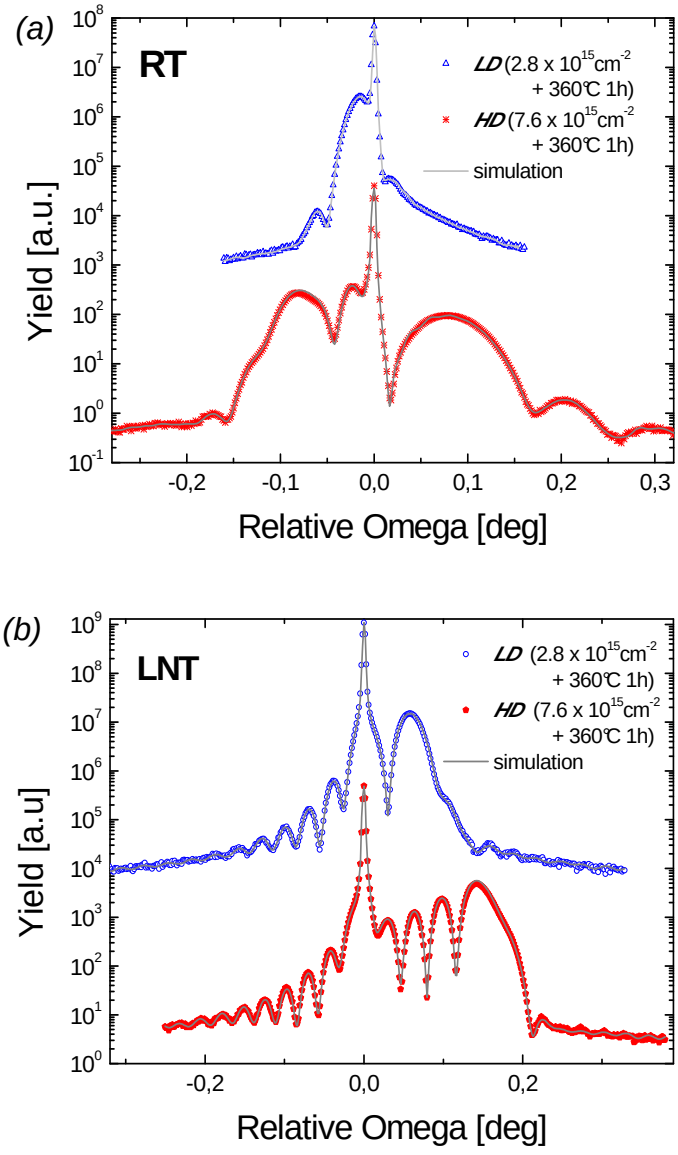

Figure 3.23: *(a) (004) Rocking Curves of the RT boron implanted and annealed samples: open blue triangles are the LD sample, red stars are the HD one; (b) (004) Rocking Curves of the LNT boron implanted and annealed samples: open blue circles are the LD sample, open red diamonds are the HD one.*

From the RCs simulations (the best fits are the continuous lines over the data in figures 3.23(a)-(b)) the corresponding perpendicular strain profiles were derived (figures 3.24(a)-(b)), permitting thus to be quantitative in the strain observations. The strain profile of the *RT-LD* sample showed positive perpendicular strain, i.e. lattice expansion, while the profile of the RT-HD sample had a negatively strained region near the surface and a positively strained region deeper (figure 3.24(a)). B implantation at Liquid Nitrogen Temperature induced a negative perpendicular strain corresponding to a lattice contraction compared to the lattice substrate (figure 3.24(b)). Moreover the strain profiles coming from the LNT implanted samples showed a small (but not negligible) amount of positive strain in a shallow region located in correspondence of the original amorphous/crystal interface, as deduced from RBS measurements.

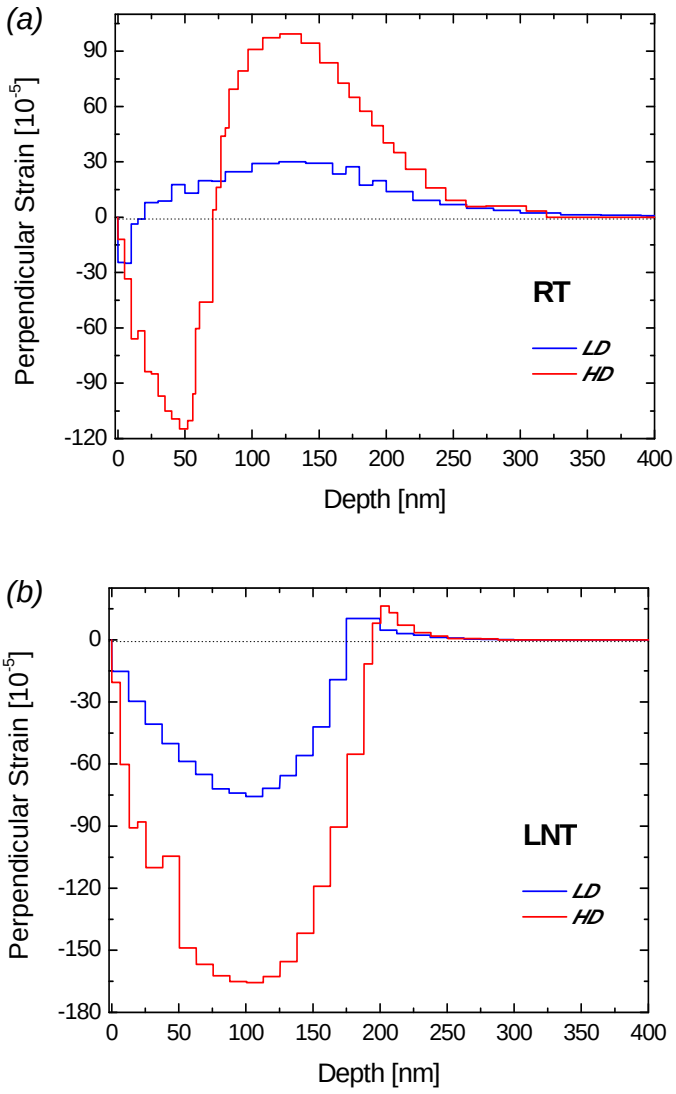

Figure 3.24: *(a) RT samples strain profiles: blue line LD samples, red line HD samples; (b) LNT samples strain profiles: blue line LD samples, red line HD samples.*

Superimposing the LNT implanted samples strain profiles to the corresponding SRIM simulation [90] of the implanted B ions distribution (in figures 3.25(a) and (b)) the almost perfect match between them clearly appeared, both for the LD and the HD samples: this gave evidence of the accuracy of $\varepsilon_{\perp}$ determination, and confirmed that the negative strain is due to the implanted boron.

Moreover from figures 3.25(a) and (b) it could be deduced that the implanted boron could not explained the shallow positive strained regions, because they were located on the tail of the B implantation, where B concentration is negligible. From silicon [81], [83], [84], and from self-amorphized germanium experiments described in the previous paragraph, the presence of positive strain - typical of interstitial-type defects, and its location just below the interface, were evidences of presence of a small amount of EOR defects also in B implanted samples at LNT.

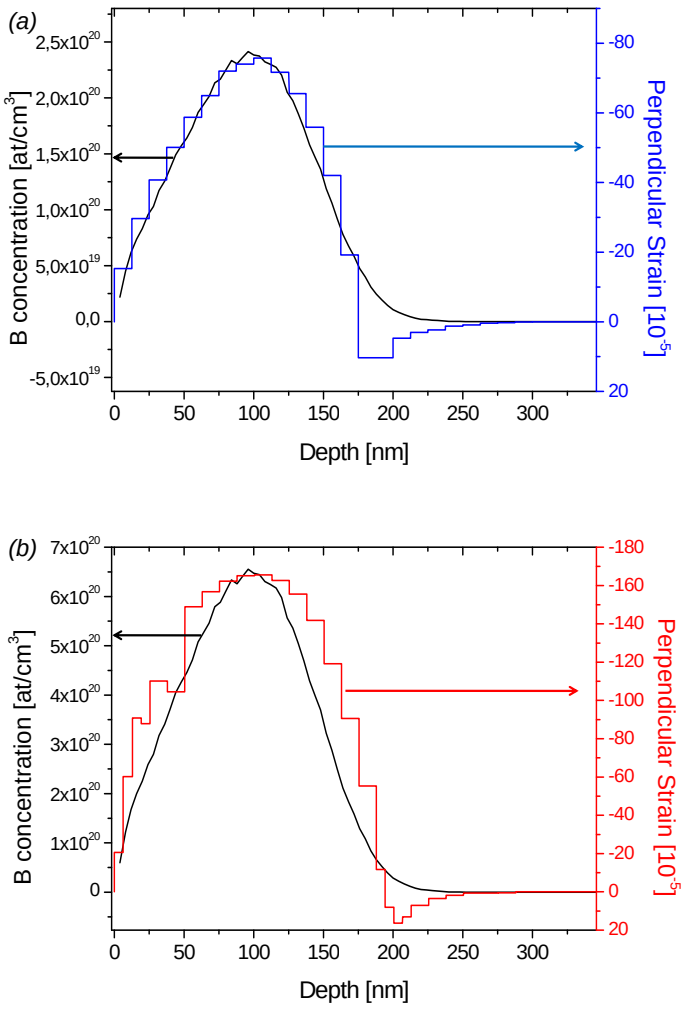

Figure 3.25: *SRIM simulations and perpendicular strain profiles of the LNT B-implanted and then annealed samples: (a) LD sample; (b) HD sample. Notice the reverse direction of the y-axis related to* $\varepsilon_{\perp}$ *profile.*

The data coming from HRXRD strain profiles, together with IBA and electrical measurements, allowed to obtain precise values about the lattice modification Δa induced by substitutional, clustered and precipitated boron.
If boron was placed in substitutional sites, it could be assumed that a $Ge_{1-x}B_x$ dilute alloy was formed. The lattice parameter of the alloy could be reasonably approximated as weighted linear average of the lattice parameter of the parental elements, i.e. a_{Ge} and a fictitious cubic B lattice parameter a_{Bs}:

$$a_{Ge_{1-x}B_x} = a_{Ge} + (a_B - a_{Ge})x = a_{Ge} + \Delta a_{Bs}, \tag{3.5}$$

where x indicated boron concentration and Δa_{Bs} was the specific lattice deformation induced by substitutional boron.
The link between the strain measured in the sample and Δa_{Bs} was represented by equation 2.22:

$$\varepsilon_{\perp} = \frac{2\nu}{1-\nu} \cdot \frac{x \cdot \Delta a_{Bs}}{\rho_{Ge} a_{Ge}}, \tag{3.6}$$

where ν is the Poisson ratio (defined in eq. 2.14) and ρ_{Ge} is the germanium atomic density.
Since $\varepsilon_{\perp}$ had not a constant profile in the examined samples it was preferable to re-write previous equation using a quantity measurable with more precision, like the integral strain profile I_{strain} (defined in equation 2.26):

$$I_{strain} = \frac{2\nu}{1-\nu} \cdot \frac{D_{Bs}}{\rho_{Ge} a_{Ge}} \cdot \Delta a_{Bs}, \tag{3.7}$$

where D_{Bs} was the B electrically active dose or, equivalently, the substitutional B dose.
It was not correct to use the implanted fluences because it would give rise to an overestimation of substitutional B induced-strain in the *LNT-HD* sample, in which a not negligible fraction of the implanted boron in the *LNT-HD* sample precipitates [58], [89] (in figure 3.26 the strain integral plotted as a function of total B fluences (blue triangles) or as a function of the substitutional B fluences (red squares) were compared).

For *LNT-HD* sample, equation 3.7 had to consider also the contribution of precipitated boron Δa_{Bp} on the lattice deformation:

$$I_{strain} = \frac{2\nu}{1-\nu} \cdot \left[\frac{D_{Bs}}{\rho_{Ge} a_{Ge}} \cdot \Delta a_{Bs} + \frac{D_{Bp}}{\rho_{Ge} a_{Ge}} \cdot \Delta a_{Bp} \right]. \tag{3.8}$$

Both substitutional and precipitated boron caused lattice contraction, as deduced from the negative values obtained for Δa_{Bs} and Δa_{Bp} (table 3.3).
Instead, for the RT samples equation 3.7 had to consider the contribution of the electrically inactive boron:

$$I_{strain} = \frac{2\nu}{1-\nu} \cdot \left[\frac{D_{Bs}}{\rho_{Ge} a_{Ge}} \cdot \Delta a_{Bs} + \frac{D_{Bc}}{\rho_{Ge} a_{Ge}} \cdot \Delta a_{Bc} \right] \tag{3.9}$$

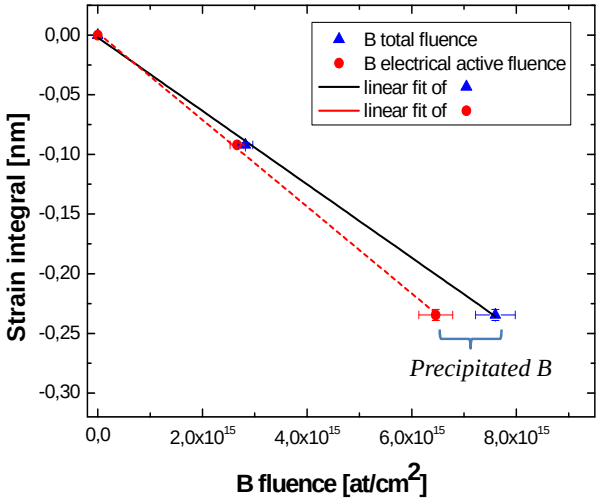

Figure 3.26: *I_{strain} of the LNT implanted and annealed samples as a function of B total fluence or B electrical active fluence. The curly bracket indicates the precipitated B fraction.*

The electrical inactive B induced positive lattice deformation (table 3.3), i.e. it gave rise to lattice expansion compared to substrate lattice parameter.

Sample Code	**Lattice Deformation Δa [Å]**		
	Substitutional	*Precipitated*	*Clustered*
LNT-LD	-1.30 $\pm$ 0.08	–	–
LNT-HD	-1.30 $\pm$ 0.08	-0.16 $\pm$ 0.03	–
RT-LD	-1.30 $\pm$ 0.08	–	+1.04 $\pm$ 0.10
RT-HD	-1.30 $\pm$ 0.08	–	+1.04 $\pm$ 0.10

Table 3.3: *Lattice modification Δa for substitutional, clustered and precipitated boron in the corresponding sample.*

The fictitious lattice parameter of cubic B crystal obtained from these data was equal to (4.35 $\pm$ 0.08)Å; in silicon a_B was equal to (3.78 $\pm$ 0.07) Å [91].

During the substitutional process there was not only a simple replacement of a Ge atom with a B atom: indeed, combining B and Ge covalent radii the strain would result overestimated of a factor $\sim$2. The same consideration applied to B and Si led to a strain error only about 20%. Probably the replacement was coupled with a charge transfer or an alloy ordering, as in $Si_{1-x}Ge_x$ [94] and $Si_{1-y}C_y$ [93] alloys happened.
With regard to the clustering phenomenon, this induced a volume expansion ΔV_{Bc} equals to + (14.8 $\pm$ 1.7) Å per B atom. The volume expansion of B clustered in silicon was equal to + (3.7 $\pm$ 0.6) Å [92]. Since in silicon the formed B-Si complexes had a stoichiometry of 4:1, it appeared reasonable explaining the volume expansion in germanium with the formation of B-Ge complexes rich of interstitials. A strong support was supplied by the work of Impellizzeri et al. [89], in which the ratio between B:Ge off-site was equal to 1:8.

In summary, from detailed characterization of boron doped germanium samples it has been deduced that:

- when boron is implanted at low fluence keeping the substrate at Liquid Nitrogen temperature it can be completely electrically activated because 100% of B atoms are placed substitutional sites: this can be verified measuring the amount of lattice contraction in the implanted region;
- when about 3 10^{15} at/cm^2 of B fluence is exceeded, a small B fraction precipitates;
- boron implanted at low fluence but keeping the substrate at Room Temperature doesn't amorphize, and after annealing the residual damage interacts with boron, which is electrically inactive because trapped in clusters: this can be verified measuring the clusters induced positive strain;
- when a higher B dose is implanted in substrate kept at room temperature, just the small boron fraction positioned in amorphous pockets can be placed in substitutional sites after annealing, it is electrical active and induces negative strain; the other fraction is off-sites and probably clustered, inducing lattice expansion.

Moreover, the HRXRD technique revealed the presence of a small amount of positive strain induced by the End Of Range defects when B amorphized Ge is epitaxially regrowth, similarly to what has been observed in self-amorphized germanium and in silicon.
X ray Diffraction determination of substitutional boron lattice parameter allowed to have a fast and powerful technique from which the electrical results about the amount of electrically active boron can be confirmed, without destroying the sample.

Chapter 4

Conclusions

The renewed interests towards germanium, discussed in the introduction of this thesis, had to face the lack of studies about some fundamental physical properties of germanium and the oldness of the data at disposal in literature. In particular, it resulted that the physics about germanium behaviour, when subjected to fundamental technological processes (e.g. amorphization, epitaxial regrowth and dopant implantation), was not completely known.
Thus, from a scientific and technological point of view it was essential to fill the gaps.

This work of thesis was inserted into this research field and it provided contributions in explaining the following topics:

- the identification through the induced strain of the amount and the nature of the defects formed after amorphizing and non-amorphizing implants, and the study of their dissolution kinetics;

- the study of the strain induced by boron when implanting at different fluences and at different substrate temperatures (room and Liquid Nitrogen temperatures).

For both the topics, the High Resolution X-Ray Diffraction technique has been used in order to overcome the limits showed by other techniques, such as Transmission Electron Microscopy (TEM), to detect low density of small defects and to perform the observations without destroying the samples.

About the first topic, this work of thesis unequivocally demonstrates the formation of End-Of-Range (EOR) defects below the amorphous/crystal interface in germanium just amorphized at medium energy (300 keV).
The amorphization of the sample, keeping the substrate at Liquid Nitrogen temperature, allowed to obtain a continuous amorphous layer at the surface of the sample, which appeared as a null strain region in the corresponding strain profile, since HRXRD is blind to amorphous

layers at the surface. But in the same strain profile a very shallow region located just below the amorphous/crystal interface was present, with a considerable amount of positive perpendicular strain. The detected strain location and its positive sign were both evidences of the presence of EOR interstitials defects.

A detailed study performed at high temperatures permitted to highlight the dissolution kinetics of these defects. In fact, the presence in the diffraction apparatus of a hot stage allowed to collect rocking curves *in situ during* the annealing. Therefore correlating the changes in the rocking curves features with the annealing temperatures (according to the procedures described in chapter 2) four dissolution stages have been singled out, each with a specific activation energy and pre-factor, reported on table 3.1.
The comparison between the theoretical data present in literature and the activation energy of the first dissolution stage suggested that the latter could be due to the migration of interstitials created by the amorphization process. The hypothesis was supported also by the pre-factor value compatible, within the error bar, with the Ge phonon frequencies, meaning that no other species were involved in the process. About the other three stages, the values found suggested the involvement of more complex defects than simple interstitials or vacancies, and for this reason requiring higher thermal budgets to dissolve.

Performing the last annealing at 320 °C, the epitaxial regrowth of the amorphous layer has been obtained, but a thin strained layer was still present at the interface due to the survival of a small amount of EORds. Only after annealing at higher temperature (about 400 °C), the complete dissolution of the defects has been reached.
The few studies reported in literature didn't detect EOR defects after the epitaxial regrowth of samples amorphized with medium energy implants, but this fact is compatible with the results shown in this thesis since in the previous works the samples regrowth was performed at about 400 °C the temperature at which in this work is demonstrated the complete dissolution of defects. Only recently, EORds have been detected by TEM performing the epitaxial regrowth at 330 °C, confirming thus the results reported in this work.

To complete the picture drawn, samples implanted with three different sub-amorphizing fluences have been analyzed (indicated as low-dose, medium-dose and high-dose samples). The damage created by the implants strongly depends on fluence: this appeared evident by comparing the strain amount of the three samples (in particular, in the sample implanted with the lower fluence no strain has been detected), but also by comparing the strain amount measured immediately after the implant procedure and after five months. The medium-dose sample after this time showed a strain lowering without any annealing, the so-called *ageing phenomenon*, while the high-dose sample strain remained the same. Ageing phenomenon has been revealed here for the first time and it confirmed the different stability of the defects formed as a function of fluence.

Moreover these two samples have been subjected to annealing treatments with the aim to discover defect dissolution kinematics. For the medium-dose sample, other three dissolution stages have been singled out; also for the high-dose sample four dissolution stages have been discovered, but the temperatures range covered by each stage didn't match for the two samples, confirming thus the different nature of the damage as a function of fluence.
In literature only one work studied defects formed after sub-amorphizing implants, but the analyzed sample was implanted with Si ions at 1 MeV, creating probably a heavier damage: this was confirmed also by the results obtained after thermal treatments, which showed defects survival at higher temperatures compared to those obtained in this thesis.

The collected data offered the possibility to compare germanium and silicon.
These two substrates are very different under many aspects and the results illustrated in this thesis confirm this issue.
Silicon has a higher melting temperature compared to germanium, but this fact by itself is not sufficient to explain the different ranges of temperatures at which defects dissolution takes place in the two materials. In germanium four types of defects are formed after both amorphizing and sub-amorphizing implant doses and dissolve one by one through annealing at progressively higher temperatures. In silicon, depending on the temperature of the annealing, the defects grow in their main size while decreasing in density (in the so-called *Ostwald ripening* process), and this fact allowed to observe them by TEM technique.
Moreover, in both the materials, after complete dissolution of the EOR defects a negatively strained region is formed near the surface, due to the presence of vacancies. However in silicon the extent of this tensile strain has almost the same order of magnitude as the compressive strain measured after amorphization, while in germanium the modulus of the negative strain is two order of magnitude lower than the positive strain due to EORds after amorphization.
This observation could be interpreted into the frame of the main mechanism of self-diffusion: while in silicon it is intersitialcy mediated mechanism, in germanium it is vacancy mediated, therefore interstitial defects formed in germanium by implantation probably diffuse in the substrate and annihilate with the vacancies instead of aggregating.
This hypothesis can explain also the data coming from SIMS measurements of the sub-amorphized samples, containing boron delta layers. Boron profiles measured in the as-grown samples and after implants plus the annealing that completely dissolved the defects didn't change. Since boron diffuses through interstitials, the absence of any diffusion enhancement indicated the presence of a recombination mechanism that suppressed the interstitials saturation.

In order to complete the picture on the damage caused by implants in germanium, it has been investigated boron implantation in germanium crystals, keeping the substrates at different temperatures (i.e. at room or Liquid Nitrogen temperatures).

The study of boron implanted in germanium samples by HRXRD arose from the demand of giving to ion beam analyses (IBA) and electrical measurements results a strain counterpart. A reliable quantification of lattice variation induced by substitutional/precipitated/clustered B in Ge lattice was lacking.

IBA and electrical measurements showed the possibility of obtaining very different levels of boron electrically active (i.e. placed in substitutional sites) by tuning the substrate temperature during B implantation. In particular, the implantation at Liquid Nitrogen temperature avoided the so-called *dynamic annealing* freezing the damage, and led to the amorphization of the doped region: the subsequent annealing treatment for the epitaxial regrowth allowed to obtain a very high incorporation of B in substitutional sites.
The amount of substitutional boron in these samples implanted at LNT has been demonstrated to depend also on the boron fluence: indeed, when a B fluence of about 3 10^{15} at/cm^2 was exceeded, a small B fraction precipitated.
On the contrary, when the same samples were implanted at room temperature (RT) a continuous amorphous layer was never formed, and the subsequent implant damage annealing gave a much reduced substitutional and electrically active B amount, due to the formation of B-Ge clusters.

HRXRD measurements of the samples implanted at LNT found out that substitutional B induced negative strain, while analyzing the samples implanted at room temperature it has been discovered that the clustering phenomenon reversed the strain of substitutional B from negative into positive.
The negative strain due to substitutional B cannot be explained by simply combining B and Ge covalent radii, on the contrary to what occurs in Si: indeed, the use of Ge and B covalent radii led to a strain overestimation of a factor $\sim$2, while the same procedure in Si leads to a much smaller difference. A possible explanation could be the presence of a charge transfer and/or a B-Ge alloy ordering, as hypothesized for $Si_{1-x}Ge_x$ and $Si_{1-y}C_y$ alloys.

In the samples implanted at Liquid Nitrogen temperature, besides the negative strain induced by substitutional boron, it has been detected also a positively strained region, located below the amorphous/crystalline interface, due to end-of-range defects presence caused by the implantation process.

Combining the information about the strain and the substitutional B amount, it was possible to determine the specific lattice contraction Δa induced by substitutional, precipitated and clustered boron: Δa_s = (-1.30 $\pm$ 0.08) Å; Δa_p = (-0.16 $\pm$ 0.03) Å; Δa_c = (+1.04 $\pm$ 0.10) Å.
If in silicon the lattice contraction due to substitutional boron has a value compatible to that found in Ge ($(\Delta a_s)_{Si}$ = (-1.66 $\pm$ 0.06) Å), it is not possible to affirm the same for the lattice expansion due to clustered boron. Indeed, the larger boron-interstitial clusters detected in silicon (the so-called *BIC*) induce a lattice expansion of Δa_{BIC} = (+0.32 $\pm$ 0.05) Å, lower than that induced by boron-interstitial clusters in germanium. The explanation is the stoichiometry

of the complexes involved: for B-Si complexes the ratio is 4:1, for B-Ge the ratio is estimated to be 1:8, i.e. interstitial-rich structures were formed.

In summary, in this work of thesis it has been demonstrated the existence of end-of-range defects in self-amorphized germanium both before and after the annealing required to regrow the crystalline structure. Moreover through a detailed study of the defects dissolution kinematics, it has been discovered that four stages are needed to dissolve the defects, the first probably involving the migration of interstitials formed in the implantation process. The study of sub-amorphizing implants allowed to determine the damage dependance on the implant fluence: in particular, for a certain fluence the so-called ageing phenomenon (which consists in the dissolution of the defects without annealing) has been revealed. The dissolution of the defects formed by sub-amorphizing implants, which took place in four stages, gave the possibility to verify that the released interstitials flux didn't promote boron diffusion, probably for mechanisms of local interstitials-vacancies recombination.
The HRXRD study of crystalline germanium implanted with boron gave a strain counterpart to IBA and electrical measurements, confirming the effectiveness of dopant implantation directly in the crystal if appropriate implant conditions are chosen, in particular if the substrate during the implantation is kept at liquid nitrogen temperature. Besides, the determination of the substitutional boron lattice parameter allows to determine the amount of substitutional boron in the sample in a fast and effective way, supporting thus the electrical measurements.

The results obtained in this thesis represent a step forward in the description of some physical phenomena in germanium - such as the implant damage and boron diffusion - and they can be used in the formulation of more complete theoretical models for the interpretation these phenomena.

Appendix A

Determination of deuterium concentration depth profiles in dilute nitride: fulfilment of previous work

Dilute nitrides such as *GaAsN*, *GaPN*, or *InGaAsN* are obtained from III-V semiconductors such as *GaAs*, *GaP*, or *InGaAs* by the insertion of nitrogen into the group V sublattice [henini]. They gained a renewed interest in scientific community at the beginning of the 1990s, inspired by the success in the fabrication of high-quality III-V alloys based on (Al, Ga, In)(As, P), as well as the breakthrough in growth of wide-band-gap III-nitrides. The main motivation was the possibility to close the gap between the nitrides and the arsenides, and thus to fabricate light emitters covering the entire visible spectral range based on the direct band-gap materials. Indeed, unlike the conventional III-V semiconductor alloys, dilute nitrides exhibit a huge bowing of the band-gap energy due to a strong mismatch in electronegativity and atomic size between N and the replaced anion atom. For example, although *GaN* has a band-gap nearly 2 eV higher than that of GaAs, the band-gap of the ternary alloy GaN_xAs_{1-x} decreases rapidly with increasing N content. Just 1% of N decreases the room-temperature band-gap from $\sim$1.42 eV to $\sim$1.25 eV [taliercio]. Moreover, the giant band-gap bowing is accompanied by a reduction in the lattice constant of dilute nitrides [bisognin], as opposed to conventional III-V alloys.
Such a unique combination of these remarkable fundamental properties made dilute nitrides great promises for the realization of novel optoelectronic devices based on *GaAs* technologies operating within the wavelength of 1.3-1.55 μm for data- and tele-communications [nakahara], as well as for efficient solar cells [kurtz].

Besides the new possibilities in device applications provided by this new material system, many physical properties that distinguish dilute nitride from other semiconductor alloys have been discovered. It has been shown that all the effects associated with N in *GaAs* (and *GaP*)

are dramatically affected by H irradiation : hydrogen restores the pristine *GaAs* electronic properties, such as the band-gap value [polimeni1], [baldassarri], [polimeni2], the electronic effective mass [polimeni3], [masia] and, most surprising, it reverses the *GaAsN* lattice strain, from tensile to compressive [klar],[bisognin2]. Moreover, it has been observed that the H effects described above are fully reversible by thermal annealing of the samples at elevated temperature ($\sim$600 °C) [bisognin2]. The complete restoring of the properties that *GaAsN* had before hydrogenation excludes the possibility of N desorption cause of hydrogenation. These H-related effects allow dilute nitrides for additional employment opportunities [felici].

For all these reasons, it seemed essential to obtain a full comprehension of the microscopic mechanism leading to N passivation in dilute nitrides.

Besides the experimental works [jiang], [ciatto], lot of theoretical efforts [bonapasta], [du], [fowler] have been spent in order to identify one or more N-H complexes responsible of the observed properties of hydrogenated dilute nitrides: by these studies dihydrogen-nitrogen complex with C_{2v}-like symmetry was suggested as a good candidate for explaining the recovery of the *GaAs* band gap and lattice constant of hydrogenated dilute nitrides, but not for justifying the compressive strain, which high resolution x-ray diffraction (HRXRD) measurements demonstrated to be caused by a different complex [bisognin2]. Indeed, HRXRD data showed that after moderate annealing (T = 250 °C) the GaAsN lattice parameter went back the to the alloy value before N insertion, without affecting N passivation (as shown by PL data [bisognin2]) , while the restoring of the lattice parameter of pristine GaAsN as well as the bandgap energy of the sample before H irradiation has been obtained only with higher temperature annealings (T$\sim$330°C) [bisognin3].
The experimental results of ref. [bisognin3] suggested to investigate theoretically the stability of complexes with more than two H atoms: the extra H atoms responsible for the compressive strain could be lost with the annealing, and the complexes could transform into the C_{2v} ones, responsible for N passivation. Amore Bonapasta and co-workers [bonapasta2] studied a new stable complex with four hydrogen atoms, i.e. a C_{2v} complex with two further weakly bounded H atoms, as the final product of GaAsN hydrogenation.

However, the available results showed a quite puzzling picture and it appeared clear that an extensive and exhaustive experimental study was necessary in order to determine univocally the correct stoichiometric [H]/[N] ratio for both the complexes formed after full hydrogenation: this was the scope of my bachelor degree thesis. This object could be achieved using a technique suitable to determine hydrogen and nitrogen amounts and their location on the samples: if this was not important for nitrogen which had a constant concentration profile (as deduced by measuring constant depth-strain profiles in the as-grown samples), it was fundamental for hydrogen, since it is the smallest atomic species and it easily diffuses into semiconductors.
SIMS technique showed difficulty of getting good standards for H concentration and to avoid

possible matrix effects. The best method in this case was the Nuclear Reaction Analysis for its ability to detect trace amount of impurities with low atomic mass contained in a substrate with higher atomic mass. Substituting hydrogen with deuterium, which is negligibly present in the natural isotopic abundance, but modifies electronic and structural properties of dilute nitrides as hydrogen does, it has been possible to perform $^2H(d,p)^3H$ and the $^{14}N(d,\alpha)^{12}C$ reactions. These allowed to quantify the total amount of nitrogen and deuterium doses, but the D-induced reactions did not permit deuterium depth profiling.

In order to obtain the deuterium concentration depth profiles, the less conventional $^3He(d,p)^4He$ nuclear reaction has been used [dieumegard]. This reaction was never used before in the case of dilute nitrides, thus I dealt with its feasibility on the system under study.
The first sample I analyzed was a $GaAs_{1-x}N_x$ epilayer grown by solid source molecular beam epitaxy on (001) *GaAs* substrate, which N concentration was x = 0.0122 and the thickness t = (223±10) nm. It has been irradiated with a deuterium fluence d_D equal to 3×10^{18} cm^{-2}. The sample (which incorporated a D dose equal to 25.34 at/cm^2) was fully passivated, as demonstrated by HRXRD and photo-luminescence (PL) measurements [bisognin2]. Hereafter this sample is identified with the label *E389*.

After preliminary measurements performed in order to determine the best measurement conditions, I analyzed the collected $^3He(d,p)^4He$ spectra with the *SIMNRA* program [simnra], verifying that the total amount of D obtained with this reaction was compatible, within the error bars, with the amount detected by $^2H(d,p)^3H$ reaction. The achieved depth resolution was equal to 50 nm.

The deuterium concentration profile appeared uniform inside the $GaAs_{1-x}N_x$ layer of the *E389* sample, but surprisingly, the profile showed also a deuterium tail with a low concentration value diffused into the *GaAs* buffer. This deuterium in excess, which was obviously not bound to nitrogen, clearly influenced the [D]/[N] ratio and implied that extreme care in determining the stoichiometry of the N-D complexes was required.
In order to obtain a good estimation for the [D]/[N] ratio two strategies could be adopted:

- considering all the deuterium into the *GaAsN* layer or,
- subtracting from the whole deuterium into the layer a constant concentration value equal to the highest measured into the *GaAs* buffer.

If the [D] / [N] ratio was calculated using the total deuterium dose found through the $^2H(d,p)^3H$ reaction, it would have the value of about *four*. Instead, using this (rather rough) procedure, the ratios obtained had values significantly lower, ranging from **3.5** to **2.5** .
Then, the correction procedures suggested that the number of hydrogen atoms bounded to nitrogen atoms are only *three*, and this is the stoichiometry of the complex giving rise both to compressive strain and to nitrogen passivation.

The same *E389* sample was then annealed at 250 °C in so that to remove the compressive strain observed after deuteration and to restore the N-free *GaAs* lattice parameter. The deuterium depth profile collected after the sample annealing showed that D concentration lowered uniformly within the whole *GaAsN* layer, maintaining a constant value , while the tail of deuterium not bound slightly diffused deeper into the buffer. Applying the same strategies illustrated above for the estimation of the [D]/[N] ratio, after annealing its value ranged from **2.2** and **1.6**.

The difference in the [D] / [N] ratio before and after annealing at 250 °C was about one: the compressive strain was produced by the complex responsible for N passivation plus an additional, weakly bound satellite D atom, released already by the moderate energy supplied during the 250 °C annealing. This picture agreed with the IR absorption [jiang] and x ray absorption [ciatto] measurements.

After a higher temperature (328 °C) annealing, which restored the lattice parameter and the bandgap energy of not-deuterated *GaAsN*, deuterium concentration profile in the *GaAsN* layer decreased further and only a broadened low concentration peaked at the GaAsN/GaAs interface was detected. The observation suggested that with this annealing also *N-2D* dissolved, and deuterium left did not affect sizably the lattice or the electronic properties of *GaAsN*. Therefore some deuterium not bound to nitrogen was present both before and after annealings, and the procedure of correction of the [D] / [N] ratio was justified. With the aim to clarify if the incorporation of deuterium not bound to nitrogen could depend on deuteration conditions, preliminary analyses were performed on a sample in which the cooling procedure at the end of the deuteration process had been varied (namely by cooling down the sample immediately after D implantation, instead of keeping it for 10 min in deuterium atmosphere). This sample needed a slightly higher thermal budget in order to restore the *GaAsN* lattice parameter (T =355 °C), moreover the NRA spectrum that I analyzed demonstrated that after this annealing a higher concentration of deuterium not bound to nitrogen was left into the sample, both in the layer and in the buffer. These data suggested that the deuterium excess was dependent in some way on deuteration conditions.

At the end of my work of thesis the stoichiometry of the different complexes formed after full deuteration was determined: only two different N-D complexes are responsible for the hydrogen-related effects observe in the examined samples. The *N-3D* complex, responsible for the increase in the lattice parameter, which a moderate annealing converted in the *N-2D* complex, still capable of N passivation, by losing one D atom bound to N less tightly than the other two atoms. After an annealing at higher temperature, *N-2D* dissolved and the *GaAsN* lattice parameter and energy gap are almost fully recovered, even if some deuterium was still present in the sample.
However some aspects were still unexplained and they have been the objects of my study in

the first part of my PhD period. Firstly, it was important to confirm that the stoichiometric [D]/[N] ratios singled out for the complexes in the *E389* sample were independent of the *GaAsN* layer characteristics, like the thickness and the nitrogen concentration, and of other deuteration conditions, like the D fluences and beam current.

Secondly, it was fundamental to clarify in which way the D incorporation proceeded: it could be possible that in a first time N-2D complexes were formed, and only after the full passivation of the layer, further deuterium was incorporated and weakly bounded to nitrogen; the deuterium amount not bound to nitrogen could be accumulated during passivation or after that step.
With the aim to answer to the first question, a thinner sample (t =(110 $\pm$ 5) nm) containing a slight higher nitrogen concentration ($x = 0.014$) was subjected to the same analyses as the E389 sample. The sample had a 35 nm thick *GaAs* cap. Hereafter this sample is labeled *E510*.
The HRXRD analysis confirmed the pseudomorphicity of the epilayer after deuteration, demonstrating that the changes observed in the perpendicular lattice parameter of this deuterated layer were due to the clusters formation/dissolution and not to relaxation of the epitaxial constraint. Moreover with the rocking curve simulation the full passivation of the layer was verified.
NRA measurements with the reactions $^2H(d,p)^3H$ and $^{14}N(d,\alpha)^{12}C$ showed a ratio between deuterium and nitrogen amounts near **4**, similar to that obtained in the sample E389 (see table I of ref.[berti]).

Performing the simulation of the spectra coming from the nuclear reaction $^3He(d,p)^4He$, I verified the presence of the deuterium excess tail also in this new sample, with a percentage of diffused deuterium only slightly higher than in the previous analyzed sample *E389* (15% in the *E510* sample against 10% of the *E389* sample), but it diffused less deeper in the GaAs buffer (figure A.1 to compare with figure 4 of ref. [berti]). Following the same strategies of subtraction of the deuterium excess from the deuterium total amount described above, the [D] / [N] ratio obtained ranged from **3.4** to **2.3**.
These data suggested that the deuterium not bound to nitrogen depended (slightly) on the sample characteristics, but confirmed the stoichiometry 1:3 for the N-D complexes formed after full deuteration.

The sample was then annealed. The first mild annealing was performed at T =235 °C, a temperature lower compared to that used for the *E389* sample, but sufficient for compressive strain removing (as verified by HRXRD measurement [bisognin3]). The deuterium dose left into the *GaAsN* layer had a higher concentration compared to that in the *E389* sample, but the same was observed for the tail; moreover the tail was still less deeper than that in the *E389* (figure A.1). These observations explained the range for [D] / [N] ratio which cover higher values, from **2.7** to **1.9**. However the presence of N-D complexes with stoichiometry 1:2 was confirmed. Probably a higher deuterium excess than the subtracted amount was incorporated

in the layer.

After a higher temperature annealing (T =315 °C) was performed, which removed nitrogen passivation, the deuterium dose left in the sample was equally distributed between the layer and the *GaAs* buffer (similarly to what happened in the *E389* sample), but it had a very low concentration. For this reason it has been very difficult to determine exactly the tail extension in the GaAs buffer, and in figure A.1 a rough estimation is reported.

Finally a 610 °C annealing was performed, in order to verify that the thermal budget supplied led the full recovering of the initial GaAsN lattice parameter and the total deuterium desorption.

The whole data extracted from the deuterium concentration profiles for these two samples after full deuteration and after the annealing stages are reported on ref. [berti].

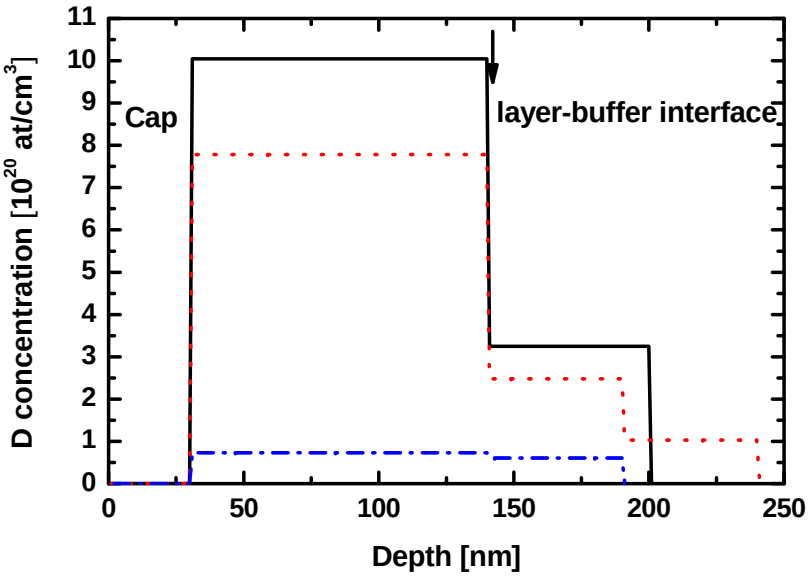

Figure A.1: *Deuterium depth profiles derived from the $^3He(d,p)^4He$ reaction in a 110-nm-thick GaAsN (N at 1.4%) sample at the end of the deuteration process (black line),at the end of the 235 °C annealing stage (red line), and at the end of the 315 °C annealing stage (blue line).*

The mechanism of deuterium incorporation was clarified examining samples irradiated with increasing deuterium fluences, without achieving the full passivation of the layer. Two 280-nm-thick $GaAs_{0.9873}N_{0.0127}$ samples (hereafter labeled *E271*), as-grown and irradiated with nominal deuterium doses d_D equal to 0.7×10^{18} and 1.2×10^{18} cm^{-2} were measured first by HRXRD (figure A.2(a)) and by PL (figure A.2(b)). These measurements demonstrated that N passivation grew with deuterium fluence, without completing it. More precisely, the rocking curves simulation showed a deuterium containing layers thickness corresponding to the 46% and 57% of the whole film thickness for the lower and higher d_D values, respectively.

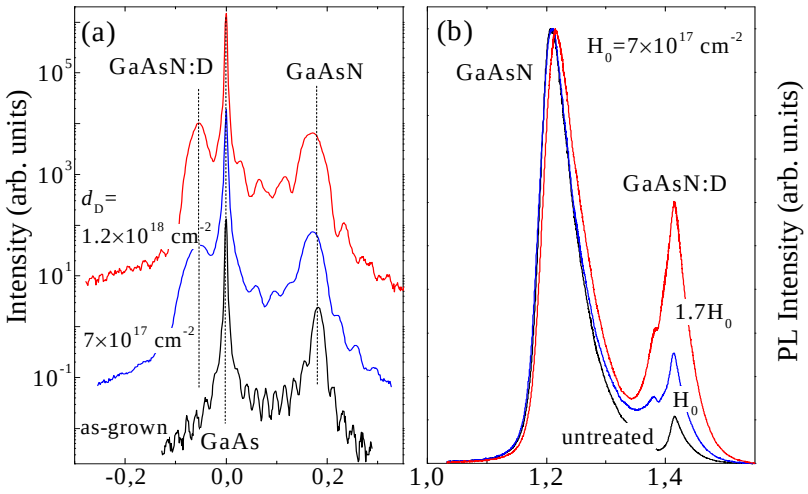

Figure A.2: *(a) (004) x-ray diffraction rocking curves of the 280-nm-thick* $GaAs_{0.9873}N_{0.0127}$ *sample before (bottommost curve) and after deuterium irradiation with doses* $d_D = 0.7 \times 10^{18}$ *and* 1.2×10^{18} cm^{-2} *(middle and topmost curves, respectively). (b) Peak normalized photoluminescence spectra at T=290 K of the same samples displayed in (a). The same laser power density was used for all samples.*

The deuterium depth profiles for this two samples are drawn in figure A.3. The thickness of the deuterated layers obtained by $^3He(d,p)^4He$ nuclear reaction agreed with those obtained by HRXRD.

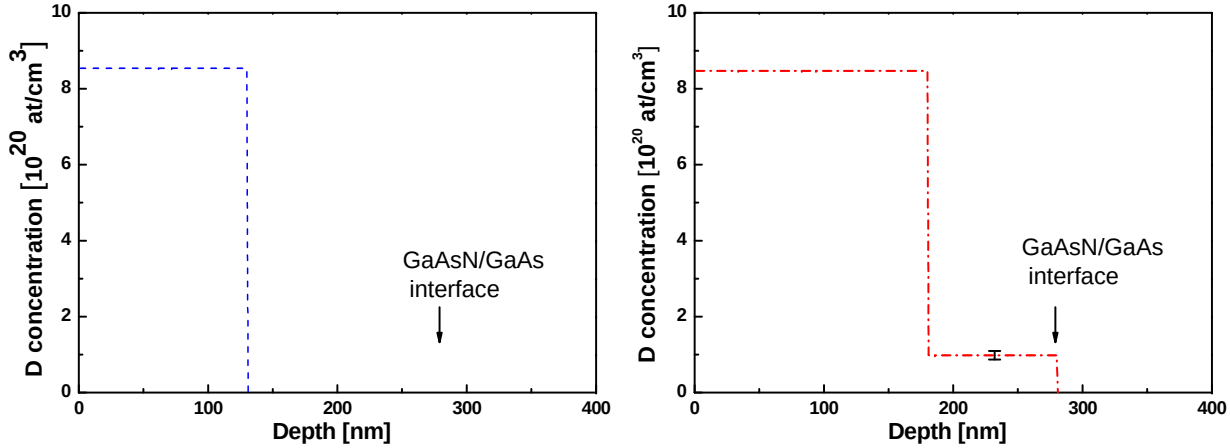

Figure A.3: *Deuterium depth profiles derived from NRA using the 3He(d, p)4He reaction in the sample after (a)* 0.7×10^{18} cm^{-2} *irradiation fluence; (b)* 1.2×10^{18} cm^{-2} *irradiation fluence.*

From these profiles it appeared clear that deuterium incorporation in the *GaAsN* layer proceeded with a *sharp front* and with a constant concentration, even if for the sample at higher fluence a tail at low concentration - inside the *GaAsN* layer - was present. Probably, even if the complexes formation took place progressively with the progress of the deuteration front,

a small part of deuterium could go deeper in the sample by defects presence in the strained GaAsN:D layer and at the *GaAsN*-layer/buffer interface. This suggestion was confirmed by analyzing samples with *GaA*s homoepitaxial layers, in which upon deuteration excess deuterium was not observed.
Performing the ratio between the nitrogen concentration involved in the passivation and the deuterium concentration, it was found a value 1:3, that is one N atom per three D atoms. The same result was obtained for both d_D fluences - not considering the tail.

The depicted scenario is that of a deuteration process which initially proceeds in a "layer-by-layer" fashion, leading to the formation of a N-3D complex and inducing both N electronic passivation and compressive strain. During the process of passivation, D in excess was accumulated. This part not bound to nitrogen had a concentration depth profile that, in the samples completely passivated, slightly extended into the *GaAs* substrate, but it was peaked on the *GaAsN*-layer/buffer interface. The phenomenon could be attributed to the presence of defects in the strained GaAsN:D layer and at the *GaAsN*-layer/buffer interface which mediated incorporation and diffusion of this extra D. Indeed, measuring *GaAs* homoepitaxial layers subjected to deuterium irradiation, it has been found that the D amount trapped in the samples was negligible.
The amount of defect present in a sample could depend on the sample characteristics: this can explained the different amount of deuterium excess accumulated by the analyzed samples. The deuteration process (as well the compressive strain) is almost independent of hydrogenation conditions and of the N-hosting semiconductor matrix , suggesting that the N-3D complex is the final product of the deuteration in all dilute nitrides.

Bibliography

[1] Seeger A. and Chik K. P., *Phys. Stat. Sol.* **29**, 455 (1968).

[2] Shaw D., *Phys. Stat. Sol.* **72**, 11 (1975).

[3] Letaw H. Jr., Portnoy W.M. and Slifkin L., *Phys. Rev.* **102**, 636 (1956).

[4] Valenta M.W. And Ramasastry C., *Phys. Rev.* **106**, 73 (1957).

[5] Campbell D.R., *Phys. Rev. B* **12**, 2318 (1975).

[6] Vogel G., Hettich G. and Mehrer H, *J. Phys. C: Solid State Phys.* **16**, 6197 (1983).

[7] Werner M., Mehrer H and Mochheimer H.D., *Phys. Rev. B* **32**, 3930 (1985).

[8] Fuchs H.D., Walukiewicz W., Haller E.E., Dondl W., Schorer R., Abstreiter G., Rudnev A.I., Tikhomitov A.V. and Ozhogin V.I. *Phys. Rev. B* **51**, 16817 (1995).

[9] Hüger E., Tietze U., Lott D., Bracht H., Bougeard D., Haller E. E. and H. Schmidt *Appl. Phys. Lett.* **93**, 162104 (2008).

[10] Räisänen J., Hirvonen J. and. Anttila A, *Solid-State Electron.* **24**, 333 (1981).

[11] Friesel M., Södervall U. and Gust W., J. *Appl. Phys.* **78**, 5351 (1995).

[12] KringhØj P. and Elliman R.G., *Appl. Phys. Lett.* **65**, 324 (1994).

[13] Silvestri H.H., Bracht H., Lundsgaard Hansen J., Nylandsted Larsen A. and Haller E.E. *Semicond. Sci. Technol.* **21**, 758 (2006).

[14] Tweet A.G., *Phys. Rev.* **106**, 221 (1957).

[15] Penning P., *Phys. Rev.* **102**, 1414 (1956).

[16] Hiraki A., Cleland J.W. and Crawford J.H. *Phys. Rev.* **177**, 1203 (1969).

[17] Watkins G. D. and Corbett J. W., *Phys. Rev.* **134**, A1359 (1964).

[18] Whan R.E., *Phys. Rev.* **140**, A690 (1965).

[19] Ershov S.N., Panteleev V.,Nagornykh S.N.and Chernyakhovskii V.V.,*Soviet Physics-Solid State*, **19**, 187 (1977).

[20] Spiewak P., Muzyk M., Kurzydłowski K.J., Vanhellemont J., Miynarczyk K., Wabinski P., Romandic I., *J. Cryst. Growth* **303**, 12 (2007).

[21] Spiewak P., Kurzydłowski K.J., Vanhellemont J., Clauws P., Wabinski P., Młynarczyk K., I. Romandic, A. Theuwis, *Mater. Sci. Semicon. Proc.* **9**, 465 (2006).

[22] Gessner H. and Posselt M., presentation at E-MRS Spring Meeting, Strasbourg, 2005.

[23] Sueoka K. and Vanhellemont J., *Mater. Sci. Semicond. Process. 9*, 494 (2006).

[24] Pinto H.M., Coutinho J., Torres V. J. B., Öberg S., and Briddon P. R., *Mater. Sci. Semicond. Process.* **9**, 498 (2006).

[25] Vanhellemont J., Spiewak P. and Sueoka K., *J. Appl. Phys.* **101**, 036103 (2007).

[26] Dunlap W.C.Jr., *Progr. Semicond.* **2**, 165 (1957).

[27] Wills G.N., *Solid State Electron.* **10**, 1 (1967).

[28] Brotzmann S. and Bracht H., *J. Appl. Phys.* **103**, 033508 (2008).

[29] Riihimäki I., Virtanen A., Rinta-Anttila S., Pusa P., Räisänen J. and The ISOLDE Collaboration, *Appl. Phys. Lett.* **91**, 091922 (2007).

[30] Chroneos A., Bracht H., Grimes R. W., and Uberuaga B. P., *Appl. Phys. Lett.* **92**, 172103 (2008).

[31] Kube R., Bracht H., Chroneos A., Posselt M. and Schmidt B., *J. Appl. Phys.* **106**, 063534 (2009).

[32] Södervall U., Odelius H., Lodding A., Roll U., Predel B., and Gust W., and Dorner P., *Philos. Mag. A* **54**, 539 (1986).

[33] Chui C.O., Gopalakrichnan K., Griffin P.B. and Plummer J.D., *Appl. Phys. Lett.* **83**, 3275 (2003).

[34] Carroll S.M. and Koudelka R., *Semicond. Sci. Technol.* **22**, S164 (2007).

[35] Dorner P., Gust W., Lodding A., Odelius H., Predel B., Roll U., *Acta Metall.* **30**, 941 (1982).

[36] Meer W. and Pommerrenig D., *Z. Angew. Phys.* **23**, 369 (1967).

[37] Pantaleev V.A., *Sov. Phys. Solid State* **7**, 734 (1965).

[38] Dorner P., Gust W., Lodding A., Odelius H., Predel B., and Roll U., *Metallkd.* **73**, 325 (1982).

[39] Satta A., D'Amore A., Simoen E., Anward W., Skorupa W., Clarysse T., Van Daele B., Janssens T., *Nucl. Instr. and Meth. in Phys. Res. B* **257**, 157 (2007).

[40] Hu S.M., *Phys. Status Solidi* **60**, 595 (1973).

[41] Delugas P. And Fiorentini V., *Phys. Rev. B* **69**, 085203 (2004).

[42] Bracht H.,. Stolwijk N. A. and Mehrer H., *Phys. Rev. B* **52**, 16542 (1995).

[43] Satta A., Van Daele B., Simoen E., Vandervost W., presentation at GADEST 2007, Erice (Sicily).

[44] Simoen E., Brouwers G., David M.L., Pailloux F., Parmentier B., Clarysse T., Goossens J., Vandervost W. and Meuris M., *Mater. Sci. Semicond. Process* **11**, 368 (2008).

[45] Uppal S., Willoughby A.F.W., Bonar J.M., Evans A.G.R., Cowern N.E.B., Morris R and Dowset M., *J. Appl. Phys.* **90**, 429 (2001)3.

[46] Michel A.E., Rausch W., Ronsheim P.A. and Kastl R.H., *Appl. Phys. Lett.* **50**, 416 (1987).

[47] Koffel S., Scheiblin P., Claverie A. and Benassayag G., *J. Appl. Phys.* **105**, 013528 (2009).

[48] Trumbore F.A., *Bell. Syst. Tech. J.*, **39**, 205 (1960).

[49] Uppal S., Willoughby A.F.W., Bonar J.M., Grasby T., Morris J.H. and Dowsett M.G., *J. Appl. Phys.* **96**, 1376 (2004).

[50] Gusev V. M., Guseva M. I., Ionova E. S., Mansurova A. N. and Starinin C. V.,*Phys. Status Solidi* A **21**, 413 (1974).

[51] Jones K. and Haller E.E. *J. Appl. Phys.* **61**, 2469 (1987).

[52] Vanhellemont J., Simoen E., *J. Electrochem. Soc.* **154**(7), H572 (2007).

[53] *"Ge Based Technologies: From Materials to Devices"*, edited by C. Claeys and E. Simoen (Elsevier, Oxford, 2006).

[54] Satta A., Simoen E., Clarysse T., Janssens T., Benedetti A., De Jaeger B., Meuris M., and Vandervorst W., *Appl. Phys. Lett.* **87**, (2005) 172109.

[55] Suh Y. S., Carroll M. S., Levy R. A., Bisognin G., De Salvador D. and Sahiner M. A., *Mater. Res. Soc. Symp. Proc.* **891**, 20.1 (2007) .

[56] Suni I., Göltz G., Nicolet M.A. and Lau S.S., *Thin Solid Film* **93**, 171 (1982).

[57] Satta A., Simoen E., Janssens T., Clarisse T., De Jaeger B., Benedetti A., Hoflijk I., Brijs B., Meuris M. and Vandervorst W., *J. Electrochem. Soc.* **153**, G229 (2006) .

[58] Mirabella S., Impellizzeri G., Piro A. M., Bruno E., and Grimaldi M. G., *Appl. Phys. Lett.* **92**, 251909 (2008).

[59] Bruno E., Impellizzeri G., Mirabella S., Piro A.M., Irrera A. and Grimaldi M.G., *Mater. Sci. Engineering* B **154**, 56 (2008).

[60] Chao Y.-L, Prussin S., Woo J.C.S. and Scholz R., *Appl. Phys. Lett.* **87**, 142102 (2005).

[61] Rudawski N.G., Jones K.S. and Gwilliam R., *Mat. Sci. Eng.*(R),**61**, 40 (2008).

[62] Mayer J. W. and Rimini E., *"Ion beam handbook for material analysi"* (Academic Press, New York, 1977).

[63] Csepregi L., Küllen R. P., and Mayer J. W., *Solid State Commun.* **21**, 1019 (1977).

[64] Roth J.A. and Anderson C.L., *Mater. Sci. Rep.* **3**, 1 (1988).

[65] Haynes T.E., Antonell M.J., Archie Lee C. and Jones K.S., *Phys. Rev. B* **51(12)**, 7762 (1995).

[66] Johnson B.C., Gortmaker P. and McCallum J.C., *Phys. Rev. B* **77**, 214109 (2008).

[67] Sigurd P., Fladda G., Eriksson L. and Bjorkqvist K., *Rad. Eff.* **6**, 145 (1970).

[68] Vollmer M., Meyer J.D., Michelmann R.W. and Bethge K., *Nucl. Instr. And Meth. in Phys. Res. B* **117**, 21 (1996).

[69] Liu J., Liu X.,Chu X.W. and W.-K., *Nucl. Instr. And Meth. in Phys. Res. B* **190**, 107 (2002).

[70] Chu W.K., Mayer J.W. and Nicolet M.-A., *"Backscattering Spectrometry"* (Academic Press, New York, London, 1978).

[71] Batterman B. W. and Cole H., *Rev. Mod. Phys.* **36**, 681 (1964).

[72] Wormington M., Panaccione C., Matney K. M. and Bowen K., *Phil. Trans. R. Soc. Lond.* A **357**, 2827 (1999).

[73] Tapfer L. and Ploog K., *Phys. Rev. B* **40**, 9802 (1989).

[74] Hickey D.P., Bryan Z.L., Jones K.S., Elliman R.G. and Haller E.E., *Appl. Phys. Lett.* **90**, 132114 (2007).

[75] Koffel S., Cherkashin N., Houdellier F., Hytch M.J., Benassayag G., Scheiblin P. and Claverie A. *J. Appl. Phys.* **105**, 126110 (2009).

[76] Bisognin G., De Salvador D., Napolitani E., Berti M., Polimeni A., Capizzi M., Rubini S. and Franciosi A., *J. Appl. Cryst.* **41**, 366 (2008).

[77] Bisognin G., De Salvador D., Napolitani E., Carnera A., Bruno E., Mirabella S., Piro A.M., Romano L. and Grimaldi M.G., *J. Phys.: Cond. Matter* **20**, 175215 (2008).

[78] Bisognin G., Vangelista S.and Bruno E., *Mater. Sci. Eng.* B **155-156**, 64 (2008).

[79] Milita S. and Servidori M., *J. Appl. Cryst.* **28**, 666 (1995).

[80] Hickey D.P., Bryan Z.L., Jones K.S., Elliman R.G. and Haller E.E.,*J. Vac. Sci. Technol.* B **26(1)**, 425 (2008).

[81] Cembali F., Servidori M. and Zani A., *Solid-State Electron.* **28**, 933 (1985).

[82] Mazzone A.M., *Phys. Status Solidi A* **95**, 149 (1986).

[83] Servidori M., Angelucci R., Cembali F., Negrini P., Solmi S., Zaumseil P. and Winter U., *J. Appl. Phys.* **61(5)**, 1834 (1987).

[84] Zaumseil P., Winter U., Cembali F., Servidori M. and Sourek Z.,*Phys. Sat. Sol.* (a) **100**, 95 (1987).

[85] Fabbri R., Servidori M., Zani A. and Cembali F., *Phys. Stat. Sol.*(a) **115**, 437 (1989).

[86] Claverie A., Colombeau B., De Maudit B., Bonafos C., Hebras X., Ben Assayag G., Cristiano F., *Appl. Phys. A* **76**, 1025 (2003).

[87] Rimini E., *Ion implantation: basic to device fabrication*, (Kluwer Academic Publishers), pp.143-163.

[88] Mok K.R.C, Benistant F., JAraiz M., Rubio J.E. Castrillo P., Pinacho R., and Srinivasan M.P., *J. Appl. Physics* **103**, 014911 (2008).

[89] Impellizzeri G., Mirabella S., Bruno E., Piro A.M. and Grimaldi M.G., *J. Appl. Phys.* **105**, 063533 (2009).

[90] `www.srim.org`

[91] Bisognin G., De Salvador D., Drigo A. V., Napolitani E., Sambo A., and Berti M., *Appl. Phys. Lett.* **89**, 061904 (2007).

[92] Bisognin G., De Salvador D., Napolitani E., Carnera A., Bruno E., Mirabella S., Priolo F. and Mattoni A., *Semicon. Sci. Technol.* **21**, L41 (2006).

[93] Berti M., De Salvador D., Drigo A. V., Romanato F., Stangl J., Zerlauth S., Schäffler F. and Bauer G., *Appl. Phys. Lett.* **72**, 1602 (1998).

[94] Dismukes J.P., Ekstrom L. and Paff R.J., *J. Phys. Chem.* **68**, 3021 (1968).

Appendix

[henini] Henini M., *Dilute Nitride Semiconductors*, (Elsevier, Oxford, 2005).

[taliercio] Taliercio T., Intartaglia R., Gil B., Lefebvre P., Bretagnon T., Tisch U., Finkman E., Salzman J., Pinault M.-A., Laügt M., and Tournié E., *Phys. Rev.* B **69**, 073303 (2004).

[bisognin] Bisognin G., De Salvador D., Mattevi C., Berti M., Drigo A. V., Ciatto G., Grenouillet L., Duvaut P., and Mariette H., *J. Appl. Phys.* **95**, 48 (2004).

[nakahara] Nakahara K., Kondow M., Kitatani T., Larson M. C., and Uomi K., *IEEE Photonics Tech. Lett.* **10**, 487 (1998).

[kurtz] Kurtz S.R., Allerman A.A., Jones E.D., Gee J.M., Banas J.J., and Hammons B.E., *Appl. Phys. Lett.*, **74**, 729 (1999).

[polimeni1] Polimeni A., Baldassarri G., Bissiri H., Capizzi M., Fischer M., Reinhardt M. and Forchel A., *Phys. Rev.* B **63**, 201304(R) (2001).

[baldassarri] Baldassarri G., von Hoegersthal H., Bissiri M., Polimeni A., Capizzi M., Fischer M., Reinhardt M., and Forchel A., *Appl. Phys. Lett.* **78**, 3472 (2001).

[polimeni2] Polimeni A., Bissiri M., Felici M., Capizzi M., Buyanova I.A., Chen W.M., Xin H.P., and Tu C.W., *Phys. Rev.* B **67**, 201303(R) (2003).

[polimeni3] Polimeni A., Baldassarri G., Masia F., Frova A., Capizzi M., Sanna S., Fiorentini V., Klar P.J. and Stolz W., *Phys. Rev.* B **69**, 041201(R) (2004).

[masia] Masi F.a, Pettinari G., Polimeni A., Felici M., Miriametro A., Capizzi M., Lindsay A., Heal S.B.y, O'Reilly E.P., Cristofoli A., Bai G.s, Piccin M., Rubini S., Martelli F., Franciosi A., Klar P.J., Volz K. and Stolz W., **Phys. Rev.** B **73**, 073201 (2006).

[klar] Klar P.J., Gruning H., Gungerich M., Heimbrodt W., Koch J., Torunski T., Stolz W., Polimeni, A. and Capizzi M., *Phys. Rev.* B **67**, 121206(R) (2003).

[bisognin2] Bisognin G., De Salvador D., Drigo A.V., Napolitani E., Samb A.o, Berti M., Polimeni A., Felici M., Capizzi M., Güngeric M.h, Kla P.J.r, Bais G., Jabee F.n, Piccin M., Rubini S., Martelli F., and Franciosi A., *Appl. Phys. Lett.* **89**, 061904 (2006).

[felici] Felici M., Polimeni A., Salviati G., Lazzarini L., Armani N., Masi F.a, Capizzi M., Martell F.i, Lazzarino M., Bai G.s, Piccin M., Rubini S., and Franciosi A., *Adv. Mater. (Weinheim, Ger.)* **18**, 1993 (2006).

[jiang] Jiang F., Stavola M., Capizzi M., Polimeni A., Amore Bonapasta A., and Filippone F., *Phys. Rev.* B **69**, 041309(R) (2004).

[ciatto] Ciatto G., Boscherini F., Amore Bonapasta A., Filippone F., Polimeni A., and Capizzi M., *Phys. Rev.* B **71**, 201301(R) (2005).

[bonapasta] Amore Bonapasta A., Filippone F., and Giannozzi P., *Phys. Rev.* B **68**, 115202 (2003).

[du] Du M.H., Limpijumnong S., and Zhang S.B., *Phys. Rev.* B **72**, 073202 (2005).

[fowler] Fowler W.B., Martin K.R., Washer K., and Stavola M., *Phys. Rev.* B **72**, 035208 (2005).

[bisognin3] Bisognin G., De Salvador D., Napolitani E., Berti M., Polimeni A., Felici M., Capizzi M., Bais G., Jabeen F., Piccin M., Rubini S., Martelli F., and Franciosi A., *Phys. Stat. Sol.* (a) **204**, No. 8, (2007) 2766.

[bonapasta2] Amore Bonapasta A., Filippone F., and Mattioli G., *Phys. Rev. Lett.* **98**, 206403 (2007).

[dieumegard] Dieumegard D., Dubreuil D., and Amsel G., *Nucl. Instrum. Methods* **166**, 431 (1979).

[simnra] Mayer M., SIMNRA user/s guide, http://www.rzg.mpg.de/mam/MANUAL.pdf

[berti] Berti M., Bisognin G., De Salvador D., Napolitani E., Vangelista S., Polimeni A., Capizzi M., Boscherini F., Ciatto G., Rubini S., Martelli F. and Franciosi A., *Phys. Rev. B***76**, 205323 (2007)

Publication List

1. Berti M., Bisognin G., De Salvador D., Napolitani E., **Vangelista S.**, Polimeni A., Capizzi M., Boscherini F., Ciatto G., Rubini S., Martelli F. and Franciosi A., *Phys. Rev.* B **76**, 205323 (2007)

2. Bisognin G., **Vangelista S**. and Bruno E., *Mater. Sci. Eng. B* **155-156**, 64 (2008)

3. Bisognin G., **Vangelista S.**, Mastromatteo M., Napolitani E., De Salvador D., Carnera A., Berti M., Bruno E., Scapellato G., Terrasi A., *Thin Solid Films*, In Press, Corrected Proof, doi: 10.1016/j.tsf.2009.09.136

4. Bisognin G., **Vangelista S.**, Berti M., Impellizzeri G., Grimaldi M.G., *J. Appl. Phys.*, Accepted manuscript